ALGORITHMS FOR FLUORESCENCE LIFETIME MICROSCOPY AND OPTICAL COHERENCE TOMOGRAPHY DATA ANALYSIS: APPLICATIONS FOR DIAGNOSIS OF ATHEROSCLEROSIS AND ORAL CANCER

A Dissertation

by

PARITOSH PANDE

Submitted to the Office of Graduate and Professional Studies of
Texas A&M University
in partial fulfillment of the requirements for the degree of

DOCTOR OF PHILOSOPHY

Chair of Committee,	Javier A. Jo
Committee Members,	Brian E. Applegate
	Kristen C. Maitland
	Byung-Jun Yoon
Head of Department,	Gerard L. Coté

August 2014

Major Subject: Biomedical Engineering

ABSTRACT

With significant progress made in the design and instrumentation of optical imaging systems, it is now possible to perform high-resolution tissue imaging in near real-time. The prohibitively large amount of data obtained from such high-speed imaging systems precludes the possibility of manual data analysis by an expert. The paucity of algorithms for automated data analysis has been a major roadblock in both evaluating and harnessing the full potential of optical imaging modalities for diagnostic applications. This consideration forms the central theme of the research presented in this dissertation.

Specifically, we investigate the potential of automated analysis of data acquired from a multimodal imaging system that combines fluorescence lifetime imaging (FLIM) with optical coherence tomography (OCT), for the diagnosis of atherosclerosis and oral cancer. FLIM is a fluorescence imaging technique that is capable of providing information about autofluorescent tissue biomolecules. OCT on the other hand, is a structural imaging modality that exploits the intrinsic reflectivity of tissue samples to provide high resolution 3-D tomographic images. Since FLIM and OCT provide complimentary information about tissue biochemistry and structure, respectively, we hypothesize that the combined information from the multimodal system would increase the sensitivity and specificity for the diagnosis of atherosclerosis and oral cancer.

The research presented in this dissertation can be divided into two main parts. The first part concerns the development and applications of algorithms for providing quantitative description of FLIM and OCT images. The quantitative FLIM and OCT features obtained in the first part of the research, are subsequently used to perform automated tissue diagnosis based on statistical classification models. The results of the research presented in this dissertation show the feasibility of using automated algorithms for FLIM and OCT data analysis for performing tissue diagnosis.

DEDICATION

To the one who was constantly by my side during all these years.

You were right all along in telling me:

"It's too late now, it will always be too late. Fortunately!"[*]

[*] *Albert Camus, The Fall*

ACKNOWLEDGEMENTS

Without naming people, simply because there are too many of them to list here, I would like to thank one and all, who have contributed in any big or small, direct or indirect way to this work. This work is as much yours as it is mine.

NOMENCLATURE

CA	Calcified Fibroatheroma
CAD	Computer Aided Diagnosis
CLG-CA	Calcified Fibroatheroma with Lipid-rich Cap
CLG-FA	Fibroatheroma with Collagenous Cap
CLG-PIT	Collagen-rich Pathological Intimal Thickening
CV	Cross-validation
DLF	Discrete Laguerre Functions
DPFT	Dark Point Fixed Transform
FA	Fibroatheroma
FC	Plaque with Foam Cell Infiltration
FDA	Food and Drug Administration
FD-OCT	Frequency-domain Optical Coherence Tomography
FLIM	Fluorescence Lifetime Imaging
FOV	Field of View
HC	High Collagen Plaque
HL	High Lipids Plaque
IRF	Impulse Response Function

IT	Intimal Thickening
IVUS	Intravascular Ultrasound
LCL	Low Collagen, Low Lipids Plaque
LDL	Low Density Lipoproteins
LEC	Laguerre Expansion Coefficients
LHS	Left Hand Side
LIP-FA	Fibroatheroma with Lipid-rich Cap
LIP-PIT	Pathological Intimal Thickening with Superficial Lipid Accumulation
LOO CV	Leave-One-Out Cross Validation
LOSO CV	Leave-One-Sample-Out Cross Vlaidation
MVT	Minimum Volume Transform
NMF	Nonnegative Matrix Factorization
OCT	Optical Coherence Tomography
PIT	Pathological Intimal Thickening
RHS	Right Hand Side
SISAL	Simplex Identification via Split Augmented Lagrangian
SNR	Signal-to-noise Ratio
TCFA	Thin Cap Fibroatheroma
TD-OCT	Time-domain Optical Coherence Tomography

TABLE OF CONTENTS

LIST OF FIGURES

LIST OF TABLES

1. INTRODUCTION

The past couple of decades have seen an increasing interest in the development of a wide range of new optical imaging techniques for biomedical diagnostics [1–5]. Part of the reason for this upsurge lies in the fact that each imaging modality has its own set of strengths and limitations, which makes it suitable for certain applications but not others. For example, while confocal imaging is capable of providing sub-micron cellular resolution images, it has a limited tissue penetration depth of several hundreds of microns. In comparison, a typical Optical Coherehce Tomography (OCT) imaging system has a relatively poorer resolution of several microns, but has a higher penetration depth of couple of millimeters. In addition to resolution and penetration depth, different imaging modalities could also have different sources of contrast. Thus, while structural imaging modalities like confocal microscopy and OCT use the back-scattered light to provide rich details about cellular and tissue morphology, fluorescence imaging modalities depend on fluorescence as the source of contrast to provide information about tissue biochemistry. Because no single imaging modality can provide satisfactory performance in all respects (resolution, penetration depth, sensitivity, SNR, acquisition speed, cost, etc.), considerable research in recent years has focused on the development of multimodal imaging systems to utilize the strengths of different imaging modalities for achieving better diagnostic accuracy [6–11].

1.1 Significance

In this dissertation, we investigate the potential of a multimodal imaging system that combines Fluorescence Lifetime Imaging (FLIM) with OCT for the diagnosis of atherosclerosis and oral cancer. FLIM is a fluorescence imaging technique that is capable of providing information about autofluorescent tissue biomolecules. OCT on the other hand, is a structural imaging modality that exploits the intrinsic reflectivity of tissue samples to provide high resolution 3-D tomographic images. Since FLIM and OCT provide complimentary information about tissue biochemistry and structure, respectively, we hypothesize that the combined information from the multimodal system will increase the sensitivity and specificity for detecting atherosclerotic plaques and oral cancer in early stages. To better understand the significance of the combined structural and functional imaging in the context of the scope of this dissertation, a brief discussion on the biochemical and morphological changes associated with the pathophysiology of atherosclerosis and oral cancer is presented next.

1.1.1 Atherosclerosis

Atherosclerosis is a vascular disease characterized by the progressive thickening of arterial walls through a process of inflammation [12], which is accompanied by the accumulation of lipids, calcium and several cellular components of blood like white blood cells, macrophages, and smooth muscle cells, resulting in the formation of an *atherosclerotic plaque*. A class of atherosclerotic plaques called the *vulnerable plaques*

are characterized mainly by a thin fibrous cap and an underlying lipid-rich core. These plaques are prone to rupture, releasing thrombogenic material into the bloodstream, leading to an acute ischemic event. In fact, it is known that two-thirds of the deaths resulting from coronary events are caused by rupture of *vulnerable plaques* or some form of plaque erosion [13]. Efficient diagnosis of vulnerable plaques is therefore of paramount importance for the treatment of high-risk patients suffering from coronary artery diseases. While a fluorescence imaging modality like FLIM is capable of characterizing a plaque's biochemical content, it does not provide any information about its morphology. On the other hand, a structural imaging modality like OCT can provide high resolution tomographic images of plaques, but it cannot offer any information about their biochemistry. Because the development of an atherosclerotic plaque involves complex interactions between tissue morphology and biochemistry, a multimodal imaging system is needed for a comprehensive assessment and directed treatment of atherosclerotic plaques.

1.1.2 Oral Cancer

Oral cancers have an overall five-year survival rate of approximately 60%. However, when detected in early stages, oral cancers can have a five-year survival rate as high as 80-90% [14]. Early detection of oral cancer, therefore, holds the key for improving survival rates and reducing the need for disfiguring surgical interventions, which significantly compromises the quality of life of survivors. Diagnosis of oral cancer in late stages can be mainly attributed to the current method of diagnosis

of oral malignancies, which is primarily based on a visual inspection of oral lesions, followed by biopsies in suspicious cases. The distinction between a benign and a malignant lesion is, however, not always very clear by a mere visual examination. In the absence of a reliable screening tool, therefore, it is not easy to determine which *abnormal looking* lesions in the oral cavity are worthy of concern. Since it is impractical to perform biopsies on every suspicious lesion, the standard protocol is to watch a lesion over an extended period of time to determine if it is indeed malignant. This often leads to a situation where a potentially malignant lesion, which might be easily treatable at an earlier stage, advances into a later untreatable condition. It is known that the progression of a malignant lesion from an early stage to later stages is accompanied by both biochemical changes like alterations in the relative abundances of tissue autofluorophores [15–17] and morphological changes like epithelial thickening and loss of the layered tissue structure [18–21]. An imaging system, capable of providing information about both tissue biochemistry and morphology, could therefore serve as an effective screening tool for the early diagnosis of oral cancer.

1.2 Objectives and Dissertation Outline

Recent advances in optical imaging technology and instrumentation has enabled the acquisition of large volumes of data in near real-time. For example, the high speed multimodal FLIM-OCT system used in this study is capable of acquiring high-resolution co-registered FLIM and OCT data over a $2\times2\,\mathrm{mm}^2$ field of view in approximately 7 seconds. The vast amount of data acquired by such high-speed

imaging systems makes direct human interpretation virtually impossible. The need for automated data analysis is even more pressing in the case of multimodal imaging, where the information obtained from the constituent modalities needs to be synergistically integrated to make the most of the intrinsic advantages of the complimentary nature of information provided by the individual modalities. The paucity of such algorithms for automated image analysis has been a major roadblock in both evaluating and harnessing the full potential of optical imaging modalities for diagnostic applications. This consideration forms the central theme of this dissertation. In this spirit, the remaining sections of this dissertation are organized as follows.

Section 2 provides a concise overview of FLIM and OCT, along with an introduction to several basic concepts and definitions pertaining to FLIM and OCT data processing. This is followed by Section 3, which gives a brief description of the multimodality FLIM-OCT system and the tissue datasets used in the studies presented in this dissertation. Section 4 desribes a novel automated deconvolution algorithm for FLIM data analysis. This deconvolution algorithm forms the core of FLIM data processing presented in this dissertation. In Section 5, a new set of FLIM features based on nonnegative matrix factorization (NMF) of multispectral FLIM data are proposed. These features are more intuitive and easier to interpret than the standard fluorescence intensity and lifetime features. The performance of the new set of FLIM features is also compared against the standard FLIM features. A discussion on how a quantitative classification based on FLIM-derived biochemical features can

be combined with qualitative information obtained from OCT images to perform a comprehensive evaluation of atherosclerotic plaques is presented next in Section 6. In Section 7, automated algorithms for quantifying structural features in OCT images of hamster cheek pouches (the animal model used for oral cancer) are presented. The feasibility of performing automated diagnosis of pre-malignant and malignant oral lesions, by combining these morphological features with FLIM features in a statistical classification framework, is also demonstrated. Finally, in Section 8, some concluding remarks are presented.

2. OVERVIEW OF FLUORESCENCE LIFETIME IMAGING MICROSCOPY AND OPTICAL COHERENCE TOMOGRAPHY

2.1 Basics of Fluorescence*

Fluorescence is a phenomenon in which light absorption by a molecule is followed by spontaneous emission of light of a longer wavelength, typically within few nanoseconds after absorption. The absorption of light results in the excitation of the molecule from its ground state to a higher energy electronic state, and the subsequent emission is a result of the molecule returning back to its ground state. In general, a molecule can relax to its ground state from an excited electronic state through several mechanisms. These mechanisms are illustrated through a Jablonski diagram. To understand the process of fluorescence, a simplified Jablonski diagram is shown in Fig. 2.1, where the electronic states are represented as gray bands. The two electronic states, denoted by S_0 and S_1 denote the lowest energy state (most populated and stable energy state at room temperature, also called the ground state) and the first excited electronic state, respectively. Each electronic state further has several vibrational energy states that are shown as a set of closely spaced lines within each electronic state. Excitation of a molecule by absorption of light occurs when the energy of the incident photons matches the difference in the energy levels of the lowest vibrational level in the ground state and some vibrational level in an excited elec-

*A detailed exposition of fluorescence imaging can be found in the introductory chapters of [22]

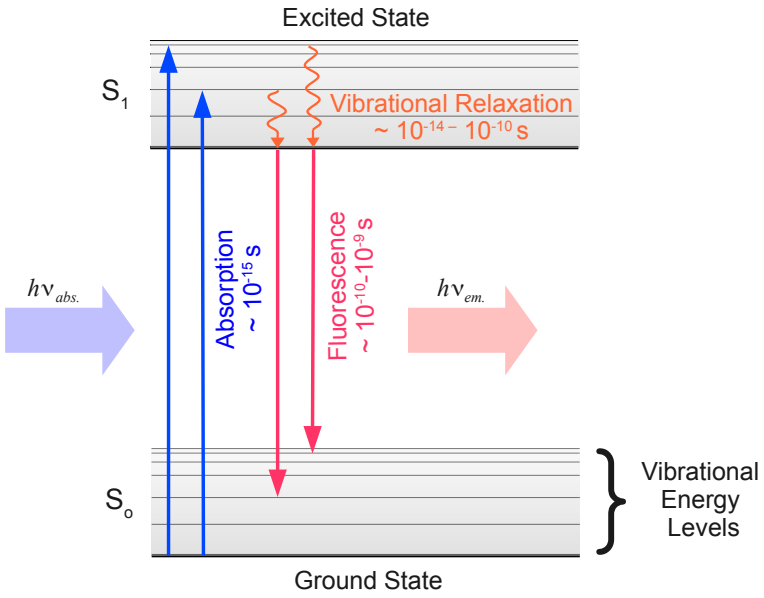

Figure 2.1: Simplified Jablonski diagram illustrating the various electronic and vibrational states of a molecule and the transitions.

tronic state (S_1 in Fig. 2.1). This transition from ground state to a higher electronic state, shown by blue arrows in Fig. 2.1, occurs over a time scale of femtoseconds.

The absorption of light is followed by relaxation of the molecule to the lowest vibrational state of the first excited electronic state (shown by orange squiggly arrows in Fig. 2.1). This transition is a non-radiative process, which happens in the order of picoseconds and is called vibrational relaxation or internal conversion if the transition occurs between the vibrational states of different excited electronic states (not shown in Fig. 2.1). The molecule residing in the lowest vibrational state of the first excited electronic state may subsequently relax to one of the vibrational states of its ground state through a radiative process, in accordance with the *Kasha's rule* [22], which states that the transition between an excited energy state to a lower energy state

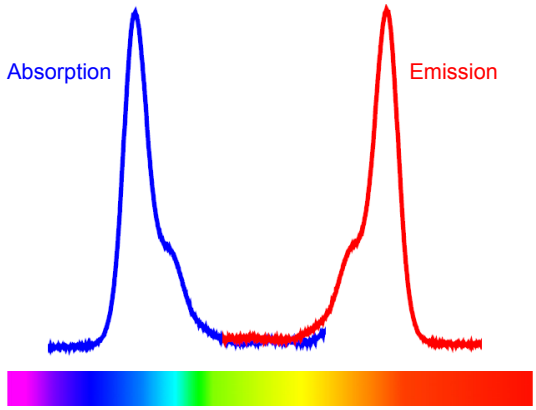

Figure 2.2: Absorption and emission spectra of a fluorophore illustrating the mirror-image symmetry property.

usually takes place from the the lowest vibrational state of the excited state. This radiative process which typically takes place on time scales of nanoseconds, is called fluorescence (shown by red arrows in Fig. 2.1). While in most cases, radiative decay occurs from the lowest vibrational state of the first excited state to a vibrational state of the ground state, some exceptions exist where molecules fluoresce directly from a higher excited electronic state; although, such cases are rare.

As mentioned earlier, depending on the excitation photon energy, a molecule can be excited from its ground state to any vibrational state of a higher energy electronic state, resulting in a broad absorption spectrum. Of the several possible transitions, some are more likely than others; the most probable transition from the ground state to an excited state being the one corresponding to the peak of the absorption spectrum. Likewise, the several possibilities for the transition between the lowest vibrational level of the first excited electronic state to the ground state, results in

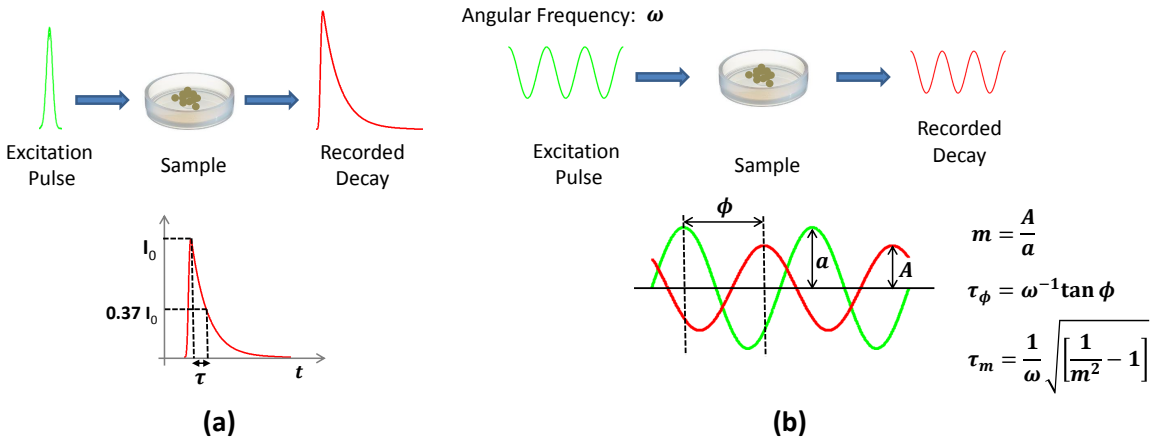

Figure 2.3: Time-resolved measurement techniques. (a) Time-domain lifetime measurements are performed by exciting the sample by a short light pulse and the lifetime τ is calculated by estimating the rate of decay of the recorded decay (shown for a simple exponential decay). (b) Lifetime estimation based on frequency-domain lifetime measurements. The sample is excited by an intensity modulated light source (sinusoidally with angular frequency ω in the example shown in the figure). The phase shift ϕ and modulation m of the emission signal with respect to the excitation waveform is used to estimate the lifetime. The two lifetimes, τ_ϕ and τ_m yield the same value for a sample exhibiting an exponential decay dynamics. In the case of complex decay dynamics, the two lifetimes represent apparent lifetimes and advanced computational methods are required to extract the true lifetime.

a broad emission spectrum. According to the Frank-Condon principle [22], in most cases, if the probability of transition from the lowest vibrational level of S_0 to say, nth vibrational state of S_1 is highest during absorption, then the probability of relaxation from the lowest energy vibrational state of S_1 to the nth vibrational state of S_0 is also the highest during emission. This results in a symmetric absorption and emission spectra as shown in Fig. 2.2, where the shift in spectra, called the *Stokes shift*, corresponds to the energy loss resulting from the non-radiative relaxation transitions.

2.2 Steady-state and Time-resolved Fluorescence Measurements

Fluorescence measurements can be classified into two broad categories: steady-state and time-resolved. In steady-state measurements, a fluorescent sample is usually excited at its peak absorption wavelength by a continuous light source and the fluorescence intensity is recorded at different emission wavelengths to obtain the emission spectrum of the sample. Due to the nanosecond timescale of fluorescence decay, the sample under continuous excitation, reaches steady-state almost immediately after excitation, and hence, the measurements obtained in this way are called steady-state measurements. Time-resolved measurements on the other hand are aimed at characterizing the sample's fluorescence decay dynamics. These measurements can be performed in either time-domain or frequency-domain as illustrated in Fig. 2.3. In time-domain fluorescence measurements, the sample is excited by a short pulse of light and the subsequent emission intensity is measured as a function of time using a high speed photo-detector. The fluorescence dynamics of the sample is characterized by measuring the rate of decay of the recorded time-resolved emission intensity. As shown in Fig. 2.3 (a), the rate of decay, denoted by τ, is called the lifetime, which in the simplest case of an exponential decay (and an ideal infinitesimally short excitation pulse) is the time it takes for the emission intensity to decay to 37% of its maximum value. In frequency-domain measurements, a high speed intensity modulated (usually sinusoidally) light source is used as the excitation source. The fluorescence emission under such excitation is also modulated in the same way

as the excitation light, but has a decreased modulation depth and is phase shifted with respect to the excitation signal. The lifetime of the sample is determined by computing the phase shift and the demodulation factor using the equations shown in Fig. 2.3 (b). For a sample exhibiting a mono-exponential decay dynamics, measurement at one modulation frequency ω, is enough, and the two lifetimes, τ_ϕ and τ_m are equal. For multi-exponential or non-exponential decays, phase and modulation measurements at multiple modulation frequencies are needed, and the true lifetime is estimated by model fitting [23].

The time-resolved fluorescence data used in this dissertation was obtained using a time-domain system described in Section 3.1.1; all subsequent discussion on time-resolved measurements will, therefore, pertain to time-domain systems.

So far, the concept of lifetime has been couched in relatively general terms as a measure of the rate of decay of fluorescence emission intensity. For a more rigorous definition of lifetime, consider the simplest case, where the relaxation process of a fluorescent molecule, from an excited state to its ground state, can be described by a first-order rate law:

$$\frac{\mathrm{d}N(t)}{\mathrm{d}t} \propto -N(t). \tag{2.1}$$

Here, $N(t)$ denotes the number of molecules in the excited state at a given time, t. Introducing a constant of proportionality, k, which represents the rate constant of the decay dynamics, and assuming that the initial population of the excited state is

N_0, the differential rate law in Eq. (2.1) can be solved as below:

$$\begin{aligned} \frac{\mathrm{d}N(t)}{\mathrm{d}t} &= -kN(t) \\ \int_{N_0}^{N(t)} \frac{\mathrm{d}N(t)}{N(t)} &= -\int_0^t k\,\mathrm{d}t \\ N(t) &= N_0 \mathrm{e}^{-kt} \end{aligned} \tag{2.2}$$

Because the intensity of fluorescence emission is proportional to the population of the excited state, the above time-dependent relationship can be equivalently expressed in terms of fluorescence intensity. The constant, $1/k$, is called the lifetime, and henceforth, shall be denoted by τ as shown below:

$$I(t) = I_0 \mathrm{e}^{-t/\tau} \tag{2.3}$$

The equation above describes the shape of the time-resolved decay, when the excitation light pulse is infinitesimally narrow. In practice, however, the excitation pulse width is finite, which results in a modified shape of the recorded decay as shown in Fig. 2.3 (a). Mathematically, the recorded decay can be expressed as the convolution of the excitation pulse with the true fluorescence decay described by Eq. (2.3). To retrieve the true fluorescence decay from time-resolved measurements, the excitation pulse, therefore, has to be deconvolved from the recorded decay. Deconvolution is an important concept in fluorescence lifetime imaging as discussed briefly later in this section, and in more detail in Section 4.

In Eq. (2.3), lifetime was defined as the inverse of the rate constant of the assumed first-order fluorescence decay dynamics. There is, however, another interpretation of lifetime, which is based on the understanding that fluorescence emission is a stochastic process. This means that in an ensemble of fluorescent molecules, a particular molecule spends a random amount of time in the excited state before relaxing to its ground state. Eq. (2.3) can then be interpreted as a stochastic decay law, where the constant τ, characterizes the average time that a fluorescent molecule spends in its excited state. This definition can be verified for the decay law expressed in Eq. (2.3) as shown below:

$$\bar{t} = \frac{\int_0^\infty tI(t)\,\mathrm{d}t}{\int_0^\infty I(t)\,\mathrm{d}t} = \frac{\int_0^\infty tI_0\mathrm{e}^{-t/\tau}\,\mathrm{d}t}{\int_0^\infty I_0\mathrm{e}^{-t/\tau}\,\mathrm{d}t} = \tau \tag{2.4}$$

While the above calculation for lifetime estimation has been worked out for a mono-exponential decay, the preceding definition of lifetime can also be used to estimate the lifetime of any complex decay law, $I(t)$. For example, for a bi-exponential decay law of the form: $I(t) = a_1\mathrm{e}^{-t/\tau_1} + a_2\mathrm{e}^{-t/\tau_2}$, the lifetime (also called the average lifetime) can be estimated as:

$$\tau \equiv \tau_{avg} = \bar{t} = \frac{\int_0^\infty t\left(a_1\mathrm{e}^{-t/\tau_1} + a_2\mathrm{e}^{-t/\tau_2}\right)\,\mathrm{d}t}{\int_0^\infty a_1\mathrm{e}^{-t/\tau_1} + a_2\mathrm{e}^{-t/\tau_2}\,\mathrm{d}t} = \frac{a_1{\tau_1}^2 + a_2{\tau_2}^2}{a_1\tau_1 + a_2\tau_2} \tag{2.5}$$

2.3 Fluorescence Lifetime Imaging

Simply put, FLIM is a fluorescence imaging technique in which time-resolved fluorescence measurements are performed over a two-dimensional FOV. A typical

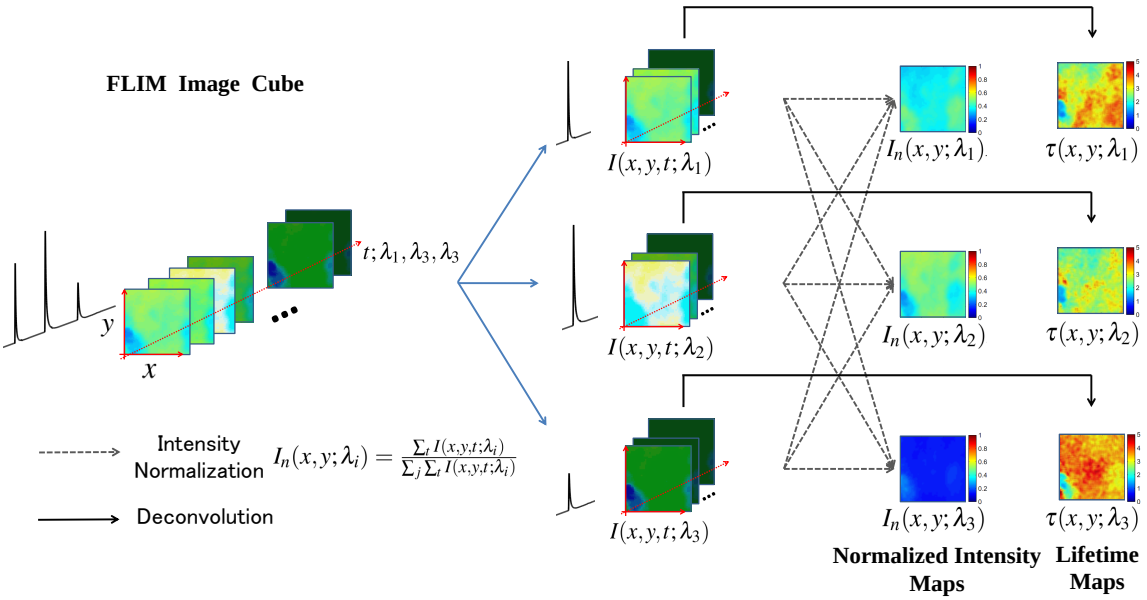

Figure 2.4: Signal processing cascade for multispectral FLIM data processing. Schematic illustrates the process of obtaining the normalized intensity maps and lifetime maps from a 3 channel multispectral FLIM data cube. The first step in the process is splitting the spectro-temporal cube into three temporal cubes (shown by blue arrows): one cube per wavelength channel. The normalized intensity and lifetime maps are then obtained from the temporal cubes by a normalization procedure (dashed lines, also see legend) and time deconvolution (solid lines), respectively. (Reproduced with permission from: P. Pande, B. E. Applegate, and J. Jo, "Application of non-negative matrix factorization to multispectral FLIM data analysis," *Biomedical Optics Express*, vol. 3, no. 9, pp. 2244–2262, 2012. ©2012 OSA)

dataset from a FLIM imaging system is three-dimensional, where in addition to the temporal dimension, there are two additional spatial dimensions corresponding to different spatial locations on the sample. In applications like tissue imaging, where there are more than one fluorophore emitting in different wavelength bands, multispectral FLIM can be used, in which, FLIM measurements are performed for several emission bands (also called *channels*). The multispectral FLIM data used in this dissertation was acquired using a three-channel FLIM system described in

Section 3.1.1. The unique detection scheme of the aforementioned FLIM system employs a set of dichroic mirrors and optical fibers of different lengths to temporally delay the fluorescence decays in the three emission bands with respect to each other. This arrangement produces a 3-D FLIM data cube, where the temporal dimension contains the concatenated fluorescence decays from the three channels.

Fig. 2.4 illustrates the signal processing cascade for obtaining intensity and lifetime maps from a 3-D data cube (labeled FLIM image cube) acquired using the three-channel FLIM system. The 3-D FLIM data cube is first split into three different FLIM data cubes, one for each wavelength band. These FLIM data cubes, denoted by $I(x, y, t; \lambda_1), I(x, y, t; \lambda_2)$ and $I(x, y, t; \lambda_3)$ in Fig. 2.4, contain the recorded time-resolved intensity at different spatial points on the sample corresponding to pixel locations (x, y). Next, intensity map for each wavelength band are obtained by integrating in time, the measured fluorescence decays in each FLIM data cube. The normalized intensity maps are then obtained by dividing the intensity value at each pixel in an intensity map by the sum of the intensity values at that pixel in the intensity maps for each wavelength band. This process of normalization is illustrated by dashed arrows in Fig. 2.4. Finally, to obtain a lifetime map for each wavelength band, the measured temporal decays in a FLIM data cube corresponding to a wavelength band are deconvolved (illustrated by solid black arrows in Fig. 2.4), and the lifetime values are subsequently obtained based on the definition of lifetime presented in Eq. 2.4. The multispectral FLIM data is finally presented in the form of a set of nor-

malized intensity and lifetime maps, denoted by $I_n(x, y; \lambda_1), I_n(x, y; \lambda_2), I_n(x, y; \lambda_3)$ and $\tau(x, y; \lambda_1), \tau(x, y; \lambda_2), \tau(x, y; \lambda_3)$, respectively as shown in Fig. 2.4.

2.4 Optical Coherence Tomography

A typical OCT system consists of an arrangement similar to a Michaelson's interferometer, where light from a low coherence source is split into two directions called the reference arm and the sample arm. In a fiber based implementation of Michaelson's interferometer, light in the reference arm is directed back after reflection from a mirror to the 2×2 fiber coupler, where it gets combined with the backscattered light from the sample in the sample arm, to generate an interference pattern, which contains information about the depth reflectivity profile of the sample. Like FLIM, OCT can also be performed in either time or frequency-domain. In a time-domain OCT (TD-OCT) system, the mirror in the reference arm is mechanically translated across the full imaging depth. At each position of the reference mirror, the intensity of the interference signal is recorded by a photodetector as shown in Fig. 2.5 (a). The depth reflectivity profile is obtained by analyzing the envelope of the temporal interference pattern recorded by the photodetector. The main drawback of a TD-OCT system is that the reference arm mirror has to be mechanically translated, which significantly limits the data acquisition speed. A frequency-domain (also called *Fourier-domain* or *spectral-domain*) OCT (FD-OCT) system differs from a TD-OCT system in that the mirror in the reference arm of a FD-OCT system is fixed and the spectrally resolved interferogram is collected using a spectrometer and a line camera as shown

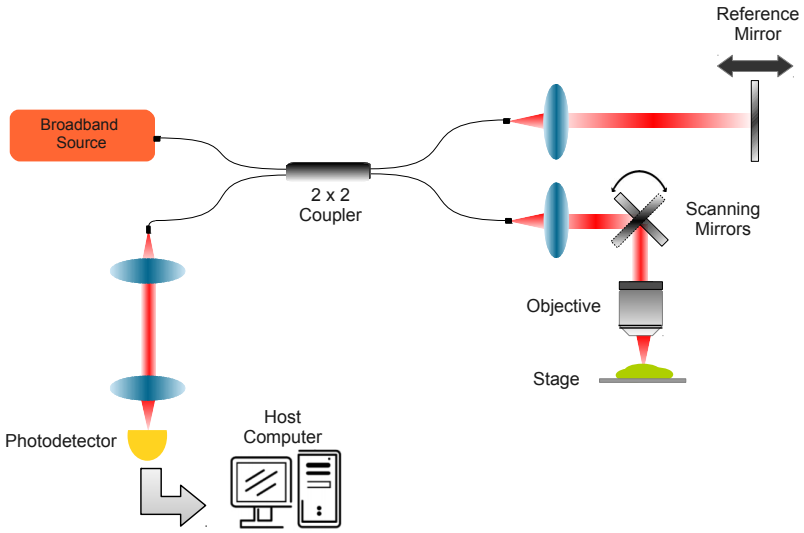

(a)

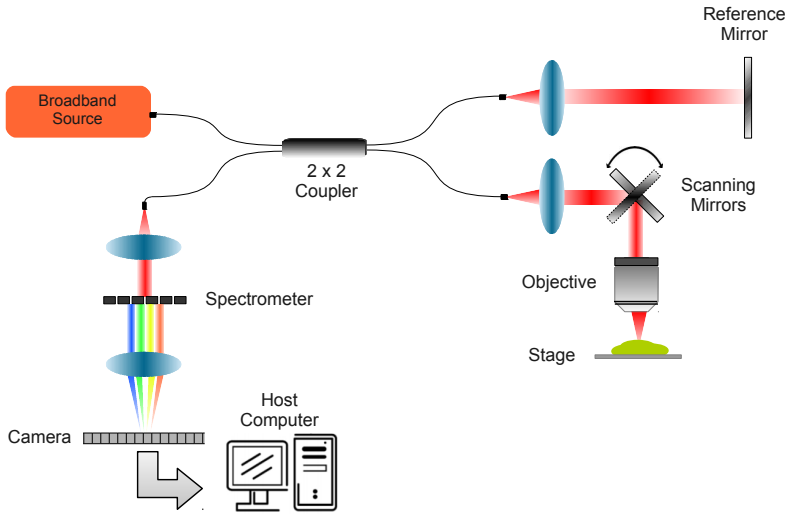

(b)

Figure 2.5: Optical coherence tomography optical setups. (a) Time-domain OCT system: The reference arm in a time-domain OCT system consists of a mirror that is mechanically translated to produce a time-varying path-length. The envelope of the temporal interference signal obtained by combining the beam reflected from the mirror in the reference arm and the backscattered light from the sample is analyzed to obtain the depth-resolved reflectivity profile of the sample. (b) Frequency-domain OCT system: The reflected beam from a fixed reference mirror and the backscattered light from the sample is recombined at the fiber coupler and the axial depth scan reflectivity profile is obtained by analyzing the spectrally encoded information contained in the interference signal obtained by using a spectrometer.

in Fig. 2.5 (b). The depth reflectivity profile, in the case of a FD-OCT system is obtained by performing an inverse Fourier transform of the interference signal obtained at the detector. Due to the fast imaging capability and high signal-to-noise (SNR) of FD-OCT systems [24], FD-OCT system is the most commonly used type of OCT system.

The OCT data used in this dissertation was acquired using a frequency-domain OCT system described in Section 3.1.2. We, therefore, focus our subsequent discussion on FD-OCT. Details about a TD-OCT system can be found in any standard text on OCT like [25, 26].

2.5 Signal Processing in a FD-OCT System*

To understand the basics of image formation in an OCT system, consider the simplest case in which the sample is modeled as a collection of N discrete reflectors having electric field reflectivities $r_{S1}, r_{S2}, \ldots, r_{SN}$ and located at distances $z_{S1}, z_{S2}, \ldots, z_{SN}$ from the beam-splitter (See Fig. 2.6 (a)). The depth-dependent reflectivity profile $r_S(z_S)$ for such a sample can then be mathematically expressed as a sum of N dirac-delta pulses as: $r_S(z_S) = \sum_{n=1}^{N} r_{Sn}\delta(z_S - z_{Sn})$. By definition, the power reflectivity is equal to the magnitude squared of its electric field reflectivity, i.e. $R_{Sn} = |r_{Sn}|^2$. The goal of OCT imaging is to reconstruct the function $r_S(z_S)$ from the interferometric measurements.

The electric field of the broadband or polychromatic light source can be expressed

*The formulations and theory presented in this section are heavily borrowed from [27]

in complex form as $E_i = s(k,\omega)\mathrm{e}^{i(kz-\omega t)}$. Here, $s(k,\omega)$ represents the contribution of monochromatic light of wave-number $k = \frac{2\pi}{\lambda}$ and angular frequency $\omega = 2\pi\nu$ to the electric field amplitude of the polychromatic light. As usual, the wavelength λ and frequency ν are related by the refractive index $n(\lambda)$ of the medium of propagation as $n(\lambda) = \frac{c}{\nu\lambda}$, where c denotes the velocity of light in vacuum. The electric field of the light passing through the 50/50 beam-splitter after getting reflected from the sample can then be expressed as $E_S = \frac{E_i}{\sqrt{2}}\left(r_S * \mathrm{e}^{i2kz_S}\right)$, where $*$ represents the convolution operation, the factor of $\frac{1}{\sqrt{2}}$ represents the 50% reduction in intensity of light due to the beam-splitter and the factor of 2 in the exponential term represents the round-trip path of the light in the sample arm. The expression for E_S can be simplified by using the property of convolution operation to yield $E_S = \frac{E_i}{\sqrt{2}}\sum_{n=1}^{N} r_{Sn}\mathrm{e}^{i2kz_{Sn}}$. Likewise, the expression for the electric-field of light in the reference arm can be written as $E_R = \frac{E_i}{\sqrt{2}} r_R \mathrm{e}^{i2kz_R}$. The interference signal detected at the photo-detector $I_D(k)$ is the time average of the intensity signal resulting from the phasor sum of E_R and E_S, i.e.

$$I_D(k,\omega) = \frac{\rho}{2}\left\langle |E_R + E_S|^2 \right\rangle \tag{2.6}$$

where ρ denotes the responsivity of the photodetector and the factor of 2 reflects the halving of intensity on the second pass of light through the beam-splitter. Simplifying the above expression based on the fact that the electric field oscillations are much faster than the responsivity of the photodetector, we get an expression involving only

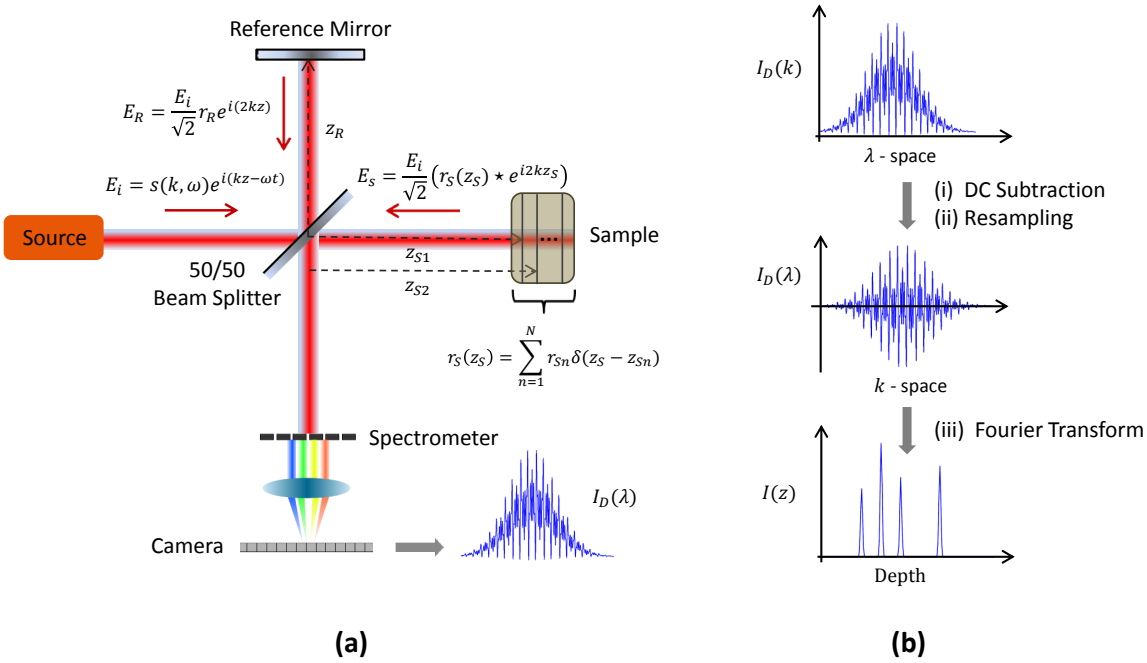

Figure 2.6: (a) Optical setups of a Fourier-domain OCT system (b) Signal processing steps involved in generating an A-line $I(z)$ from the raw Fourier-domain OCT data $I_D(\lambda)$.

time invariant terms as:

$$\begin{aligned} I_D(k) =& \frac{\rho}{4}\left[S(k)\left(R_R + R_{S1} + \ldots + R_{SN}\right)\right] + \\ & \frac{\rho}{2}\left[S(k)\sum_{n=1}^{N}\sqrt{R_R R_{Sn}}\cos\left[2k\left(z_R - z_{Sn}\right)\right]\right] + \\ & \frac{\rho}{4}\left[S(k)\sum_{n\neq m=1}^{N}\sqrt{R_{Sn}R_{Sm}}\cos\left[2k\left(z_{Sn} - z_{Sm}\right)\right]\right] \end{aligned} \tag{2.7}$$

Here, $S(k) = \langle |s\left(k,\omega\right)|^2 \rangle$ denotes the spectral dependence of the power of the light source, which for most practical applications is assumed to be Gaussian and is expressed in terms of the central wavelength and the bandwidth of the light source k_o

and Δk, respectively, as follows:

$$S(k) = \frac{1}{\Delta k\sqrt{\pi}} \mathrm{e}^{-\left[\frac{(k-k_o)}{\Delta k}\right]^2} \tag{2.8}$$

The first term in Eq. (2.7) corresponds to the DC component of the signal. This term carries no information about the location of reflectors in the sample. The second term, called the "cross-correlation" term is the desired component for OCT imaging, because it contains information about the location of reflectors in the sample (coded in the frequency of the cross-correlation terms) and the sample reflectivties (coded in the amplitude). Finally, the third term, called the "autocorrelation" term, contains information about the mutual separation between different reflectors in the sample.

In the context of FD-OCT, the wavelength resolved intensity signal, $I_D(k)$, is measured by using a combination of a spectrometer and a line camera. To obtain the reflectivity profile of the sample, an inverse Fourier transform of Eq. (2.7) is performed, which results in the depth-resolved intensity signal $I(z)$, also called an "A-line" as:

$$\begin{aligned} I(z) =& \frac{\rho}{8}\left[\gamma(z)\left(R_R + R_{S1} + \ldots + R_{SN}\right)\right] + \\ & \frac{\rho}{4}\left[\gamma(z) * \sum_{n=1}^{N} \sqrt{R_R R_{Sn}}\left[\delta\left(z \pm 2(z_R - z_{Sn})\right)\right]\right] + \\ & \frac{\rho}{8}\left[\gamma(z) * \sum_{n=1}^{N} \sqrt{R_{Sn} R_{Sm}}\left[\delta\left(z \pm 2(z_{Sn} - z_{Sm})\right)\right]\right] \end{aligned} \tag{2.9}$$

which can be further simplified to:

$$\begin{aligned} I(z) =& \frac{\rho}{8}\left[\gamma(z)\left(R_R + R_{S1} + \ldots + R_{SN}\right)\right] + \\ & \frac{\rho}{4}\left[\gamma(z)\left(2\left(z_R - z_{Sn}\right)\right) + \gamma(z)\left(-2\left(z_R - z_{Sn}\right)\right)\right] + \\ & \frac{\rho}{4}\left[\gamma(z)\left(2\left(z_{Sn} - z_{Sm}\right)\right) + \gamma(z)\left(-2\left(z_{Sn} - z_{Sm}\right)\right)\right]. \end{aligned} \tag{2.10}$$

In the above expression, $\gamma(z)$ is called the coherence function and is related to the power spectral dependence of the light source by a Fourier transform:

$$\gamma(z) = \mathrm{e}^{-z^2\Delta k^2} \overset{\mathcal{F}}{\longleftrightarrow} S(k) = \frac{1}{\Delta k\sqrt{\pi}}\mathrm{e}^{-\left[\frac{(k-k_o)}{\Delta k}\right]^2} \tag{2.11}$$

Intuitively, this means that the bandwidth of the light source is inversely related to the width of the coherence function. This relationship is significant because it relates the spectral width of the light source with the axial resolution of the imaging system. This is clear from Eq. (2.9), where it can be seen that the depth-resolved intensity signal is the convolution of the delta pulses at true locations with the coherence function $\gamma(z)$. Thus a narrower coherence function (or equivalently wide bandwidth light source) would result in sharper peaks corresponding to the locations of the reflectors in the sample, or a better axial resolution; whereas, a wider coherence function (or a narrow bandwidth light source) would produce smudged peaks in the depth-resolved intensity signal. In fact, the axial resolution for an OCT system is

indeed defined in terms of the coherence length l_c as:

$$\text{axial resolution} = l_c = \frac{2\sqrt{\ln 2}}{\Delta k} = \frac{2\,(\ln 2)}{\pi}\frac{\lambda_o^2}{\Delta\lambda} \tag{2.12}$$

We conclude this section with a brief description of the various signal processing steps involved in FD-OCT imaging, as shown in Fig. 2.6 (b). The first step in the sequence of steps is the *background subtraction*, which involves getting rid of the DC component in Eq. (2.7). The DC component can be optically estimated by recording the signal at the detector when no sample is present in the sample arm. This signal can be subtracted from the spectral interferometric signal $I_D(k)$ to get rid of the DC component. For the data used in this dissertation, the approximation to the background signal was obtained computationally by averaging the A-lines in a 2-D OCT scan (also called a B-scan, which is obtained by scanning the light beam laterally along the sample). The next step in the FD-OCT signal processing cascade is *resampling*. As noted earlier, the spectral interferometric signal $I_D(k)$ recorded by the spectrometer and line-camera combination is uniformly sampled in wavelength (sampling resolution decided by the line spacing of the spectrometer grating). In order to obtain depth-resolved signal $I(z)$ from $I_D(k)$, Fourier transform needs to be performed. However, this necessitates that the spectrally resolved data is evenly spaced in k-space. The conversion of evenly spaced data in λ-space to evenly spaced data in k-space is called resampling. To resample the signal, the known unevenly spaced k-space points corresponding to say, I evenly spaced λs:

$k_i = \dfrac{2\pi}{\lambda_i}, i = 1, 2, \cdots, I$ are used for interpolation to obtain the value of the spectral signal at evenly spaced k-space points given by $k_i = k_{min} + (i-1)\ \delta k, i = 1, 2, \cdots, I$, where $k_{min} = \dfrac{2\pi}{\lambda_{max}}$ and $\delta k = \dfrac{1}{I}\left[\dfrac{2\pi}{\lambda_{min}} - \dfrac{2\pi}{\lambda_{max}}\right]$. In this study, linear interpolation was used to resample the k-space data. The resampled k-space data is then Fourier transformed and the magnitude of the transformed data yields the depth-resolved reflectivity profile of the sample.

3. COMBINED FLIM-OCT IMAGING SYSTEM AND TISSUE DATASETS*

3.1 Combined FLIM-OCT Imaging System

In this section, we present a brief description of the combined FLIM-OCT system used to acquire the data used in this dissertation. More details about the design of the system and its validation can be found in [28]. The schematic of the combined FLIM-OCT system, shown in Fig. 3.1, can be better understood in terms of three main functional blocks: (i) FLIM sub-system (on the right), (ii) OCT sub-system (on the left), and (iii) the common path (in the center). The light path in the OCT sub-system is shown in red. Fluorescence excitation is likewise shown by dark blue arrows and the fluorescence emission in the three bands is shown in light blue, cyan, and green. All other hardware interfacing is shown by black lines. In the following sections, we present a brief description of the FLIM and OCT sub-systems, system control, and data processing.

3.1.1 FLIM Sub-system

The multipsectral FLIM system was implemented following a direct pulse-recording scheme, in which pixel rate could be equal to the laser repetition rate. A frequency

*Parts of this section are reproduced with permission from J. Park, J. Jo, S. Shrestha, P. Pande, Q. Wan, and B. E. Applegate, "A dual-modality optical coherence tomography and fluorescence lifetime imaging microscopy system for simultaneous morphological and biochemical tissue characterization," *Biomedical Optics Express*, vol. 1, pp. 186–200, 2010. ©OSA

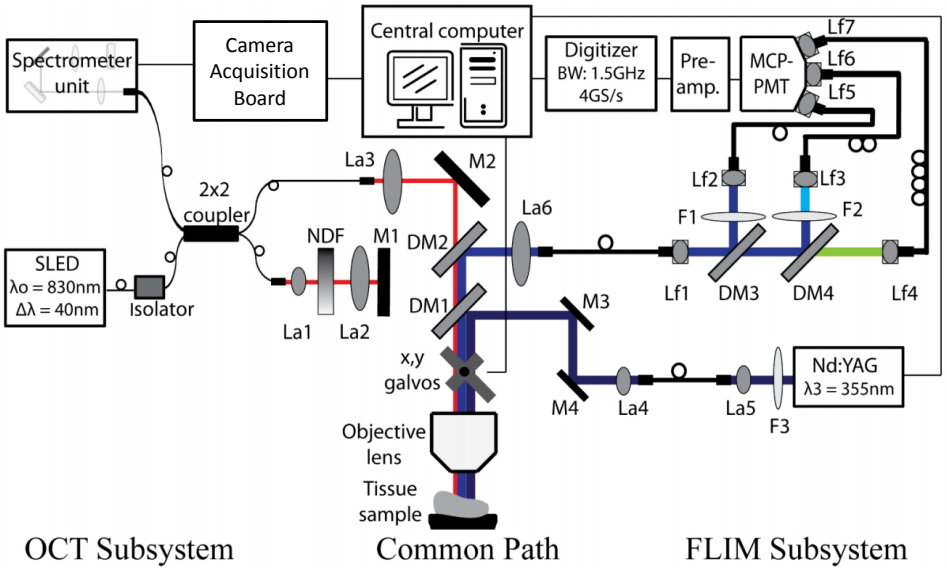

Figure 3.1: Optical setup of the dual-modality FLIM-OCT imaging system. L1, L2 and L5: open-aired collimation and coupling lenses, L3, L4, L6-L10: fiber-connected collimation and coupling lenses, NDF: neutral density filter, M1-M4: mirrors, DM1-DM4: dichroic mirrors, and F1-F4: filters.

tripled Q-switched Nd:YAG laser (SPOT-10-50-355, Elforlight Ltd., England) was used as the excitation source (355 nm, 30 kHz maximum repetition rate, 1 ns pulse FWHM). A 50 μm multi-mode fiber was used to deliver the excitation light to the FLIM-OCT common path. The emission light exiting the FLIM-OCT common path was directed through a 200 μm multi-mode fiber into a multi-spectral detection module, where the fluorescence emission was separated into three spectral channels, namely, 390 ± 20 nm, 452 ± 22.5 nm, and $600 \pm 1\,25$ nm, using a set of dichroic mirrors and filters (Chroma Technology, Bellows Falls, VT). The emission from each channel was launched into fibers with different lengths (1 m, 10 m and 19 m) chosen to provide 45 ns interval between each emission band decay. The emission

bands were selected to target tissue endogenous fluorophores like flavin adenine dinucleotide (FAD), nicotinamide adenine dinucleotide (NADH), collagen, elastin and lipids. The three consecutive decays were detected with a MCP-PMT having a rise time of 150 ps (R3809U-50, Hamamatsu, Japan) and sampled with a high bandwidth digitizer (1.5 GHz, 4 GS/s). Further details on FLIM sub-system characterization can be found in [29].

3.1.2 OCT Sub-system

The FD-OCT sub-system used a 830 nm (40 nm bandwidth) superluminescent light emitting diode (SLED) (EXS8410-2413, Exalos, Langhome, PA) as the light source, providing an axial resolution of 7.6 μm (in air). Light from the SLED was directed to a 2×2 optical fiber coupler through a single-mode fiber where it gets split into the reference and sample arms. The reflected beam from a reference mirror and the backscattered light from the sample are recombined at the fiber coupler and the spectral interferogram were obtained using a custom designed grating based high speed spectrometer (1200 L/mm, Wasatch Photonics, Logan, UT; bandwidth: 102 nm; line rate of up to 59 kHz) and and a CCD linescan camera (Aviiva, SM2CL1014, EV2 Technologies, Essex, England). The detected signal was digitized and acquired using a high speed imaging acquisition board (PCIe-1427, National Instruments, Austin, TX). The OCT subsystem had a signal-to-noise ratio (SNR) of 98 dB and a 3 dB single sided fall-off of 900 μm.

3.1.3 Common Path

The OCT sample beam and FLIM excitation were combined via a dichroic mirror (DM1) (reflects UV and transmits visible-near IR light). Beam scanning over a field of view of 2×2 mm^2 (corresponding to $600 \times 600 \times 1024$ ($x \times y \times depth$) pixels for OCT and $60 \times 60 \times 768$ ($x \times y \times time$) pixels for FLIM) was achieved using a set of galvo mirrors (6230H, Cambridge Technology, Lexington, MA). A broadly achromatic (UV-near IR) objective lens (5X/0.16 NA, EC plan-Neufluar, Zeiss, Germany) was used to simultaneously focus the OCT and FLIM excitation beams resulting in lateral resolutions of 13.4 μm for OCT and 100 μm for FLIM. The OCT and FLIM emission beams were separated by using a second dichroic mirror (DM2), which transmitted the near-IR OCT beam and reflected the UV-visible FLIM beam.

3.1.4 System Control and Data Processing

An OCT/FLIM data acquisition module was developed in Labview (Labview 8.6, National Instruments, Austin, TX) to control the electronics, data acquisition and imaging. 3-D multi-spectral FLIM datasets and co-registered OCT volumes were acquired using a galvo mirror arrangement and was saved on a host computer for post-processing. Due to the low pulse energy of the FLIM excitation beam (maximum of 240 nJ at 10 KHz), 20 tissue autofluorescence decays were averaged to improve the SNR.

3.2 Tissue Datasets

We present below a brief description of the tissue databases used for data analysis in this dissertation and the imaging protocol thereof. The two databases, namely, the arterial tissue database and the hamster cheek pouch tissue database were used in the studies relating to atherosclerosis and oral cancer, respectively. Specific details about the histopathological findings will be discussed in the context of the data analysis presented in the relevant sections, later in the dissertation.

3.2.1 Coronary Artery Tissue Database

Human coronary artery segments were obtained from 6 autopsy cases within 48 hours of the time of death, according to a protocol approved by the Texas A&M University Institutional Review Board. A total of 58 arterial segments were longitudinally opened and imaged from the lumen side. Immediately after imaging, each segment was ink marked (for correlation with histopathology), fixed in 10% formalin, and sent for histopathology analysis for which each imaged plaque segment was consecutively sectioned every $500\,\mu$m. The sections were stained with Movat pentachrome and evaluated by a cardiovascular pathologist.

3.2.2 Hamster Cheek Pouch Tissue Database

The standard Syrian golden hamster (*mesocricetus auratus*) cheek pouch model of epithelial cancer was used in this study. The animal protocol consisted of scheduled application of a suspension of 2.0% Benzo[a]pyrene (Sigma Aldrich Corporation, St

Louis, Missouri) in mineral oil to the right cheek of 20 hamsters three times per week for up to 32 weeks. 11 control animals were similarly treated with mineral oil alone. The procedure was approved by the Institution for Animal Care and Use Committee at Texas A&M University. Before imaging, the hamsters were anaesthetized by administering a mixture of ketamine and xylazine The cheek pouches of the anaesthetized animals were inverted and positioned under the microscope objective of the imaging system. After imaging, the animal was euthanized by barbiturate overdose. Biopsy samples from the imaged areas were processed following standard procedures for histopathology analysis (H&E staining) by a board certified pathologist.

4. NOVEL AUTOMATED LAGUERRE DECONVOLUTION*

4.1 Deconvolution in the Context of Time-Domain FLIM

As discussed in Section 2.2, in the context of time-domain FLIM, the recorded decay at a given pixel of the FLIM image can be mathematically modeled as a convolution of the excitation pulse and the true fluorescence decay. In the following discussion, we shall refer to the excitation pulse as the instrument response, and the true fluorescence decay as the Impulse Response Function (IRF). To estimate the IRF, therefore, the instrument response needs to be deconvolved from the recorded fluorescence decay at each pixel of the image. Estimating the instrument response is a problem in itself, which can be tackled in several ways [30]: (1) the instrument response can be approximated by the measured fluorescence decay from a sample with extremely short lifetime; (2) the instrument response can be indirectly obtained by measuring the fluorescence decay of a reference compound with known IRF; or (3) the instrument response is modeled as a pulse of certain amplitude and width. In the present research, we have used a representative Gaussian profile to model the instrument response. The most commonly used deconvolution technique for FLIM is the non-linear least-squares iterative reconvolution method [31]. This method models the IRF as a multi-exponential function and iteratively estimates the model parameters

*Reprinted, with permission, from P. Pande and J. Jo, "Automated Analysis of Fluorescence Lifetime Imaging Microscopy (FLIM) Data Based on the Laguerre Deconvolution Method," *IEEE Transactions on Biomedical Engineering.* ©*2011 IEEE*, vol. 58, no. 1, pp. 172–181, 2011.

(lifetimes and coefficients for the exponential terms) by a non-linear least squares optimization technique. There are, however, some limitations of this method. First, model selection in terms of the number of exponentials needed to correctly estimate the IRF requires *a priori* knowledge about the nature of the decay, or trying out different multi-exponential models (e.g. single-exponential, bi-exponential, and so on) and choosing the one that minimizes a certain error criterion, (e.g. chi-squared test) [22]. Secondly, the iterative process demands computation of a large number of convolutions per pixel, which is time consuming and impractical for real-time FLIM applications. Lastly, it requires large number of data samples, which increases the acquisition time. Recently, Lee and French *et al.* [32] proposed the use of a stretched exponential function: $I(t) = I_0 e^{(-t/\tau)^\beta}$, to model the IRF. This approach is more flexible than the multiexponential formulation in that it can model a complex decay as a weighted sum of exponentials where the parameter, β, is related to the probability distribution of decay times, thereby providing a much more general form for IRF modeling than the multi-exponential models. However, since the model parameters, β and τ, have to be estimated through non-linear least-squares optimization, this method is also computationally expensive and impractical for real-time FLIM applications.

A novel deconvolution method for FLIM data analysis based on the Laguerre expansion technique was recently introduced and validated [33, 34]. In this method, the IRF at each pixel of the FLIM image is expressed as a linear combination of

Laguerre basis functions with unknown coefficients. Estimating IRFs, then, amounts to finding the expansion coefficients (the weights of the Laguerre basis functions) at each pixel. The orthogonality of the Laguerre basis functions permits an extremely efficient least-squares estimation of the Laguerre coefficients. Since estimation of the expansion coefficients for all image pixels are performed simultaneously, this method performs orders of magnitude faster than other algorithms. Accurate performance of this method, however, depends on proper selection of the set of orthonormal Laguerre basis functions, defined by a parameter called the Laguerre parameter and denoted by α. In the original Laguerre FLIM deconvolution implementation, α is selected using a trial and error approach, making it unsuitable for real-time applications. In this section, we present a fully automated implementation of the Laguerre FLIM deconvolution, whereby the Laguerre parameter, α, is treated as free parameter within a nonlinear least-square optimization scheme.

4.2 Laguerre Deconvolution

In the context of time-domain FLIM, the series of time-gated fluorescence intensity maps $H(r, n)$ are given by the convolution of the IRF $h(r, n)$ with the instrument response $x(n)$:

$$H(r, n) = T \sum_{m=0}^{K-1} h(r, m)x(n - m), \tag{4.1}$$

where, r denotes the pixel number, $n = 0, 1, \ldots, N$ denotes the time gate, K determines the extent of system memory, T is the sampling interval, and N is the number

of time samples per pixel [34]. The Laguerre deconvolution technique uses a set of Discrete Laguerre Functions (DLF) as the orthonormal basis to represent the IRF:

$$h(r,n) = \sum_{j=0}^{L-1} c_j(r) b_j^{\alpha}(n), \tag{4.2}$$

where, $c_j(r)$ are the unknown Laguerre Expansion Coefficients (LEC) at the rth pixel, L is the number of DLFs (or the order of Laguerre basis) used to model the IRF, and $b_j^{\alpha}(n)$ denotes jth order DLF [34], defined as:

$$b_j^{\alpha}(n) = \alpha^{(n-j)/2}(1-\alpha)^{1/2} \sum_{k=0}^{j} (-1)^k \binom{n}{k} \binom{j}{k} \alpha^{j-k}(1-\alpha)^k \tag{4.3}$$

The Laguerre parameter ($0 < \alpha < 1$) determines the rate of exponential decline of the DLFs and defines the time scale for which the Laguerre expansion of the system IRF is most efficient in terms of convergence [35]. For a given pixel, the measured fluorescence decay $y(r,n)$ can thus be written as:

$$y(r,n) = H(r,n) = \sum_{j=0}^{L-1} c_j(r) v_j^{\alpha}(n), \tag{4.4}$$

where,

$$v_j^{\alpha}(n) = T \sum_{m=0}^{K-1} b_j^{\alpha}(m) x(n-m). \tag{4.5}$$

Then, the system of linear equations defined in Eq. (4.4) can be expressed in matrix notations as follows:

$$\underbrace{\begin{bmatrix} y(r,0) \\ y(r,1) \\ \vdots \\ y(r,N-1) \end{bmatrix}}_{\mathbf{y}_r} = \underbrace{\begin{bmatrix} v_0^\alpha(0) & v_1^\alpha(0) & \cdots & v_{L-1}^\alpha(0) \\ v_0^\alpha(1) & v_1^\alpha(1) & \cdots & v_{L-1}^\alpha(1) \\ \vdots & \vdots & \ddots & \vdots \\ v_0^\alpha(N-1) & v_1^\alpha(N-1) & \cdots & v_{L-1}^\alpha(N-1) \end{bmatrix}}_{\mathbf{V}_\alpha} \underbrace{\begin{bmatrix} c_0(r) \\ c_1(r) \\ \vdots \\ c_{L-1}(r) \end{bmatrix}}_{\mathbf{c}_r}$$

or, equivalently,

$$\mathbf{y}_r = \mathbf{V}_\alpha \mathbf{c}_r. \tag{4.6}$$

To include the effect of experimental noise, we modify Eq. (4.6) as:

$$\mathbf{y}_r = \mathbf{V}_\alpha \mathbf{c}_r + \epsilon_r, \tag{4.7}$$

where, ϵ_r is the error vector resulting due to noise at the rth pixel.

4.3 Automated Laguerre Decomvolution

The objective of deconvolution is to obtain the IRF, or, equivalently, the LEC vector $\mathbf{c}_r$ in Eq. (4.7). The correct estimation of LEC depends on proper selection of the set of DLFs, which in turn depends on proper choice of Laguerre parameter α. Equation (4.7) can be solved to get the least-squares estimate of the measured

decay $\mathbf{y}_r$, which is equal to:

$$\hat{\mathbf{y}}_r = \mathbf{V}_\alpha \left(\mathbf{V}_\alpha^T \mathbf{V}_\alpha\right)^{-1} \mathbf{V}_\alpha^T \mathbf{y}_r. \tag{4.8}$$

4.3.1 Defining and Optimizing the Cost Function

The cost function at the rth pixel can then defined as the mean squared error (MSE) of the estimated decay:

$$\begin{aligned} F^r(\alpha) &= (\mathbf{y}_r - \hat{\mathbf{y}}_r)^T (\mathbf{y}_r - \hat{\mathbf{y}}_r) \\ &= \mathbf{y}_r^T (\mathbf{I} - \mathbf{V}_\alpha \left(\mathbf{V}_\alpha^T \mathbf{V}_\alpha\right)^{-1} \mathbf{V}_\alpha^T) \mathbf{y}_r \\ &= \mathbf{y}_r^T (\mathbf{y}_r^T - \hat{\mathbf{y}^T}_r) \\ &= \mathbf{y}_r^T \epsilon_r. \end{aligned} \tag{4.9}$$

It must be reiterated that all the analysis so far focused on one pixel of the FLIM image. If we denote the number of pixels in a FLIM image by M, then, the cost function for the entire FLIM image can be written as a sum of the MSE computed for each pixel of the image:

$$F_{image}(\alpha) = F^1(\alpha) + F^2(\alpha) + \cdots + F^M(\alpha). \tag{4.10}$$

Our objective is to find the value of α that minimizes the cost function defined in Eq. (4.10). We denote this optimum value of α by $\hat{\alpha}$. Mathematically, this problem

can be stated as:

$$\arg\max_{\alpha} F_{image}(\alpha). \tag{4.11}$$

The problem stated in 4.11 can be framed as a nonlinear least-squares optimization problem. Since α is constrained in $(0, 1)$, we implemented a simple iterative gradient based optimization scheme, where the search direction and step size γ was determined using successive bisection algorithm. This iterative process can be summarized as:

$$\hat{\alpha}^{v+1} = \hat{\alpha}^{v} - \gamma^{v} \left[\frac{d}{d\alpha} (F_{image}(\alpha)) \right]^{v} \tag{4.12}$$

Here, $\hat{\alpha}^{v}$ and γ^{v} denote the estimated value of α and the step size at vth iteration. Next, we find an expression for the derivative of the cost function. Here, we briefly outline the method of obtaining such an expression. For a more detailed derivation, interested readers are referred to [36], wherein a similar expression was derived for time resolved fluorescence spectroscopy measurements. It follows from Eq. (4.9) and Eq. (4.10) that:

$$\frac{d}{d\alpha} (F_{image}(\alpha)) = \sum_{r=1}^{M} \mathbf{y}_r^T \left(\frac{d\epsilon_r}{d\alpha} \right). \tag{4.13}$$

If we define two matrices $\mathbf{Y}_{modified}$ and $\mathbf{E}_{modfied}$ as:

$$\mathbf{Y}_{modified} = \begin{bmatrix} y(0,1) & y(1,1) & \cdots & y(N-1,1) \\ y(0,2) & y(1,2) & \cdots & y(N-1,2) \\ \vdots & \vdots & \ddots & \vdots \\ y(0,M) & y(1,M) & \cdots & y(N-1,M) \end{bmatrix}^T \tag{4.14}$$

$$\mathbf{E}_{modified} = \begin{bmatrix} \frac{d\epsilon_1}{d\alpha} & \frac{d\epsilon_2}{d\alpha} \cdots & \frac{d\epsilon_M}{d\alpha} \end{bmatrix}^T \tag{4.15}$$

It can be shown that each term of the summation in Eq. (4.13) corresponds to a diagonal term of the matrix product $\mathbf{Y}^T_{modified}\mathbf{E}_{modified}$. It then follows that the summation in the right hand side (RHS) of Eq. (4.13) can be written as:

$$\frac{d}{d\alpha}(F_{image}(\alpha)) = \text{trace}\left(\mathbf{Y}^T_{modified}\mathbf{E}_{modified}\right) \tag{4.16}$$

To evaluate $\mathbf{E}_{modified}$, we define another matrix $\mathbf{C}_{modified}$ as:

$$\mathbf{C}_{modified} = \begin{bmatrix} c_0(1) & c_0(2) & \cdots & c_0(M) \\ c_1(1) & c_1(2) & \cdots & c_1(M) \\ \vdots & \vdots & \ddots & \vdots \\ c_{L-1}(1) & c_{L-1}(2) & \cdots & c_{L-1}(M) \end{bmatrix}. \tag{4.17}$$

Following the derivation in [36], we can write an expression for $\mathbf{E}_{modified}$ as:

$$\begin{aligned}\mathbf{E}_{modified} = \frac{d\mathbf{V}_\alpha}{d\alpha}\mathbf{C}_{modified} + \mathbf{V}_\alpha(\mathbf{V}_\alpha^T\mathbf{V}_\alpha)^{-1} \\ \left[\frac{d\mathbf{V}_\alpha^T}{d\alpha}\mathbf{Y}_{modified} - \left(\frac{d\mathbf{V}_\alpha^T}{d\alpha}\mathbf{V}_\alpha + \mathbf{V}_\alpha^T\frac{d\mathbf{V}_\alpha^T}{d\alpha}\right)\mathbf{C}_{modified}\right].\end{aligned} \tag{4.18}$$

Finally, to evaluate $\frac{d\mathbf{V}_\alpha}{d\alpha}$ and $\frac{d\mathbf{V}_\alpha^T}{d\alpha}$ we use the recursive property of the DLF [35], which gives:

$$\frac{dv_j^\alpha}{d\alpha} = \frac{1}{2\sqrt{\alpha}}\left(v_j^\alpha(n-1) + v_{j-1}^\alpha(n)\right) + \sqrt{\alpha}\left(\frac{dv_j^\alpha(n-1)}{d\alpha} + \frac{dv_{j-1}^\alpha(n)}{d\alpha}\right) - \frac{dv_{j-1}^\alpha(n)}{d\alpha} \tag{4.19}$$

where,

$$\frac{dv_0^\alpha}{d\alpha} = \frac{1}{2\sqrt{\alpha}}\left(v_0^\alpha(n-1)\right) + \sqrt{\alpha}\left(\frac{dv_0^\alpha(n-1)}{d\alpha}\right) + \frac{1}{2\sqrt{1-\alpha}}x(n). \tag{4.20}$$

Using Eq. (4.16) - (4.20) in Eq. (4.12), we can estimate the optimal value of α. For the analyses presented in the next section, we fixed the order of Laguerre expansion basis to 4, based on findings from previous studies [36].

4.4 Instrumentation for FLIM Measurements

The FLIM imaging was accomplished using a time-domain wide-field time-gated endoscopic FLIM instrument [37]. The central component of the FLIM system was an intensified CCD camera (4Picos, Stanford Computer Optics) coupled to a flexible endoscope through a microscope objective (20×). The endoscope was constructed

from a 10,000 fiber coherent bundle (O.D. 400 μm) glued to a GRIN lens (NA 0.5, 4 mm working distance). Light pulse excitation was delivered via a multimode fiber (NA 0.22). A filter wheel inserted in the collimated optical path was used for multi-spectral imaging at the predefined emission bands of 390 ± 20, 450 ± 20, and 550 ± 40 nm. A N_2 UV laser (337 nm, 0.8 ns FWHM, 50 Hz repetition rate, 5 μJ/pulse) was used for excitation. The FLIM images were acquired with a time resolution of 200 ps.

4.5 Method Validation on Synthetic and Experimental FLIM Data

The performance of the proposed algorithm was tested on: (i) synthetic FLIM data, (ii) experimental FLIM data from fluorescence lifetime standards, and (iii) experimental FLIM data from biological tissue.

4.5.1 Synthetic FLIM Images

A synthetic FLIM image (25 X 25 pixels) was generated using a bi-exponential model (lifetimes 1 ns and 4 ns) with relative contributions varying in a linear fashion (from 1 ns at the lower rightmost to 4 ns at the top leftmost pixel). Additive white noise was added to yield two images at 40 dB and 25 dB SNR. A representative Gaussian profile for instrument response was used to generate the synthetic FLIM images. Fig. 4.1 (a) shows the theoretically calculated lifetime map. For a mixture of two fluorophores of relative contribution $\beta, (0 \geq \beta \leq 1)$ and $(1 - \beta)$, and lifetime τ_1 and τ_2, respectively; the average lifetime of the mixture is given by [22]:

$$\tau_{\text{mixture}} = \frac{\beta\tau_1^2 + (1-\beta)\tau_2^2}{\beta\tau_1 + (1-\beta)\tau_2} \tag{4.21}$$

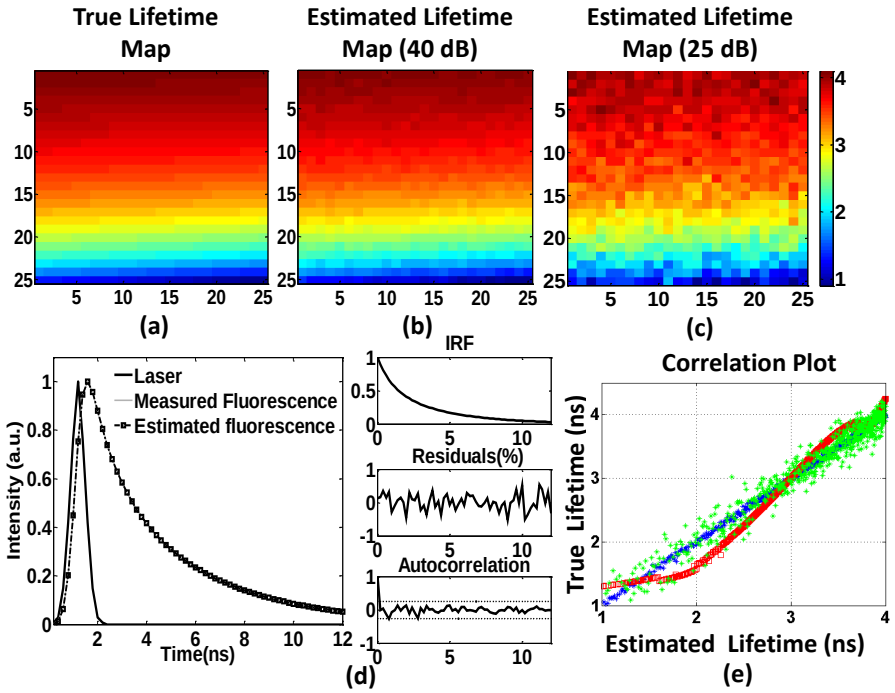

Figure 4.1: Validation results on synthetic data. (a) Theoretically calculated lifetime map. (b) Estimated lifetime map at 40 dB SNR. (c) Estimated lifetime map at 25 dB SNR. (d) Measured decay at a sample pixel and the estimated fit. Also, shown is the instrument response, estimated IRF and the error residuals. (e) Correlation between the true and estimated lifetime values at 25 and 40 dB SNR. The green and blue curves correspond to lifetimes estimated after deconvolution for 25 and 40 dB, respectively. The red curve corresponds to lifetimes estimated without deconvolution by simply fitting a bi-exponential model to the decaying part of the measured fluorescence signal (at 40 dB only).

The synthetic data was then deconvolved using the proposed deconvolution algorithm to estimate the IRF and thereafter the average lifetime map (as defined in Eq. (2.4)) was calculated from the estimated IRFs. Optimal value of α was found to be 0.829 and 0.834 for 40 dB and 25 dB noise levels, respectively. In Fig. 4.1 (d), we plot the measured decay, the instrument response profile (labelled laser), and the estimated decay for a representative pixel in the FLIM image. In order to assess the goodness of

fit of our model, we calculate the residual of the fit, normalized against the maximum value of the recorded decay. The magnitude of the residual was found to be <1% and it showed a random behavior suggesting that the model fits the data well. This was further validated by calculating the autocorrelation of the residual. Since, in the absence of any systematic errors, the residual is randomly distributed around zero, we would expect its autocorrelation function to die down to zero very rapidly, as shown in the autocorrelation inset of Fig. 4.1 (d). The estimated lifetime maps at 40 dB and 25 dB SNR are shown in Fig. 4.1 (b) and Fig. 4.1 (c), respectively. Both the estimated lifetime maps were similar to the true lifetime map; however, as expected, the variability in the estimated lifetime values was more in the low SNR condition.

The correlation plot between the true (theoretical) and estimated lifetimes for both 25 dB (green) 40 dB SNR (blue) shown in Fig. 4.1 (e) suggests good lifetime estimation by the proposed method. To illustrate the importance of deconvolution, we also estimated the lifetimes by using a bi-exponential model fit to the decaying part of the measured fluorescence decay as a surrogate for the IRF. This approach of lifetime estimation is implemented in many commercially available software for FLIM data analysis. The correlation plot for the true and lifetimes estimated in this manner (without deconvolving) is also shown in Fig. 4.1 (e) (red curve) for 40 dB SNR. The relatively poor correlation between the two lifetimes, emphasizes the need for deconvolution.

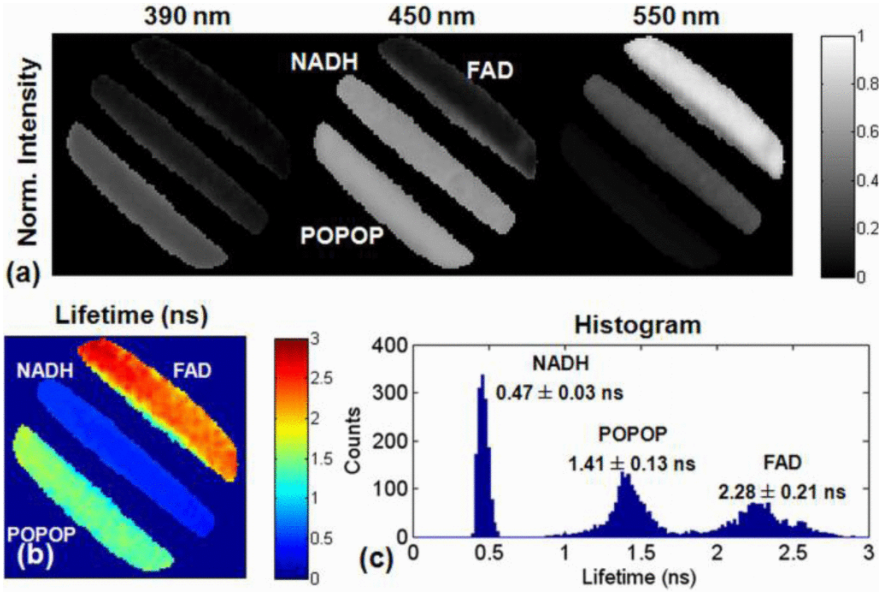

Figure 4.2: Validation results on FLIM images of standard fluorophores. Three fluorophores (POPOP, NADH, FAD) were loaded on quartz capillaries and imaged with our FLIM system. (a) The normalized intensity maps at 390 nm, 450 nm and 550 nm emission bands correctly reflect the emission spectrum of the three fluorophores. (b) The lifetime map shows accurate estimation of each fluorophore lifetime characteristics. (c) Lifetime histogram indicates that the three fluorophores can be identified directly from the estimated lifetime map.

4.5.2 Validation on Fluorescence Lifetime Standards and Endogenous Fluorophores

Validation of the proposed algorithm on fluorophores with known emission spectra and lifetimes was done in two different ways.

Experiment 1: The fluorophores used for validating our method were selected to cover a broad range of emission wavelengths (380–600 nm) and fluorescence lifetimes (0.4–12 ns). These included two exogenous flurophores: Rhodamin B (RhB) (25242, Sigma-Aldrich) and 9-cyanoanthracene (9CA) (15276, Sigma-Aldrich) dissolved in ethanol to a concentration of 1 μM and two endogenous fluorophores, relevant for

potential fluorescence based tissue diagnosis [38, 39]: Nicotinamide Adenine Dinucleotide (NADH) (N8129, Sigma-Aldrich) and Flavin Adenine Dinucleotide (FAD) (F6625, Sigma-Aldrich) dissolved in Phosphate Buffered Saline (PBS) to a concentration of 1 μM. The solutions were placed in a quartz cuvette and illuminated from one side of the cuvette, while the endoscope was positioned on the other side of the cuvette for imaging. For each sample, FLIM images corresponding to the peak emission band of that fluorophore were recorded. The laser pulse energy at the tip of the excitation fiber probe was adjusted to $\sim$5 μJ/pulse.

Experiment 2: The idea behind performing the second experiment was to demonstrate the robustness of the proposed deconvolution scheme, in terms of its ability to estimate IRFs having different decay rates (lifetimes) using the same value of α. This is of particular importance in tissue imaging applications, where different tissue regions may have different biochemical compositions (e.g. a malignant region surrounded by a normal region), thereby resulting in IRFs with different decay rates. For this experiment, we obtained a single FLIM image for three different fluorophores namely, FAD, NADH and POPOP [p-phenylenbis(5.-phenyl-2.-oxazol)]. Solutions of POPOP in Methanol, and NADH and FAD in PBS (1 μM concentration each) were prepared and loaded in quartz capillaries (400 μm diameter) for FLIM imaging. All other experimental conditions were identical to those described in the first experiment. The performance of the proposed deconvolution algorithm was evaluated by estimating a global value of α for the entire image and comparing the known lifetime

Table 4.1: Validation results from fluorescence standards and tissue endogenous fluorophores FLIM data(Laguerre order equals 4) from fluorescence standards and tissue endogenous fluorophores FLIM data

Sample (solvent)	Wavelength (nm)	C.F.[a]	Optimal α	Lifetime (ns) Estimated	Lifetime (ns) Literature	Computational Time(s)
9CA (Ethanol)	450 ± 40	1	0.953	11.92 ± 0.28	11.70–12.28	211.6
		3	0.953			37.6
RhB (Ethanol)	550 ± 80	1	0.732	2.49 ± 0.08	2.60–3.01	44.4
		3	0.730			8.5
FAD (PBS)	550 ± 80	1	0.788	2.61 ± 0.11	2.30–2.85	48.6
		3	0.788			8.9
NADH (PBS)	450 ± 40	1	0.265	0.31 ± 0.11	0.30–0.50	7.1
		3	0.263			1.4

[a]C.F. stands for Compression Factor as discussed in Section 4.6

values of three fluorophores with the lifetimes calculated from the IRFs obtained after deconvolution.

Results from the analysis of FLIM images of fluorescence lifetime standards and endogenous fluorophores, as described in Experiment 1, are summarized in Table 4.1. As mentioned earlier, Laguerre order expansion was fixed to four to estimate the fluorescence IRF in all cases. It was found that the optimal values of α were correlated with the fluorescence lifetimes: short-lived decays were expanded with smaller values of α ($\alpha = 0.265$ for NADH with $\tau = 0.31\,\text{ns}$), while longer decays required larger α values ($\alpha = 0.953$ for 9CA with $\tau = 11.92\,\text{ns}$). The lifetime maps (not shown here), showed a homogeneous spatial distribution of lifetimes. Histograms of the lifetime maps (not shown here) for all four lifetime standards were Gaussian with mean and

standard deviation values as reported in Table 4.1. The mean lifetime values reported in Table 4.1 are in good agreement with those obtained from spectroscopy measurements of the same fluorescent standard solutions with a time-resolved fluorescence spectroscopy system, as previously reported [40].

Validation results from this experiment are shown in Fig. 4.2. The normalized intensity maps at 390 nm, 450 nm and 550 nm emission bands are in accordance with the emission spectrum of the three fluorophores: the POPOP capillary showed emission at both the 390 nm and 450 nm bands, the NADH capillary showed the strongest emission at the 450 nm band, and the FAD capillary showed significant emission only the 550 nm band. Optimal value of α in this case was found to be 0.694. The lifetime values for the three fluorophores are also in good agreement with the values reported in the literature: the POPOP capillary showed a homogenous lifetime map with values $\sim$1.4 ns, the NADH capillary showed a homogenous lifetime map with values $\sim$0.5 ns, and the FAD capillary showed a homogenous lifetime map with values $\sim$2.3 ns. The histogram of the lifetime values indicate that the three fluorophores can be identified from their estimated lifetime values. Moreover, lifetime values estimated for NADH and FAD in this experiment are in good agreement with the values obtained in Experiment 1.

4.5.3 Validation on Biological Tissue Autofluorescence

The automated Laguerre deconvolution method was also tested on FLIM measurements obtained from biological tissue. A postmortem human coronary artery

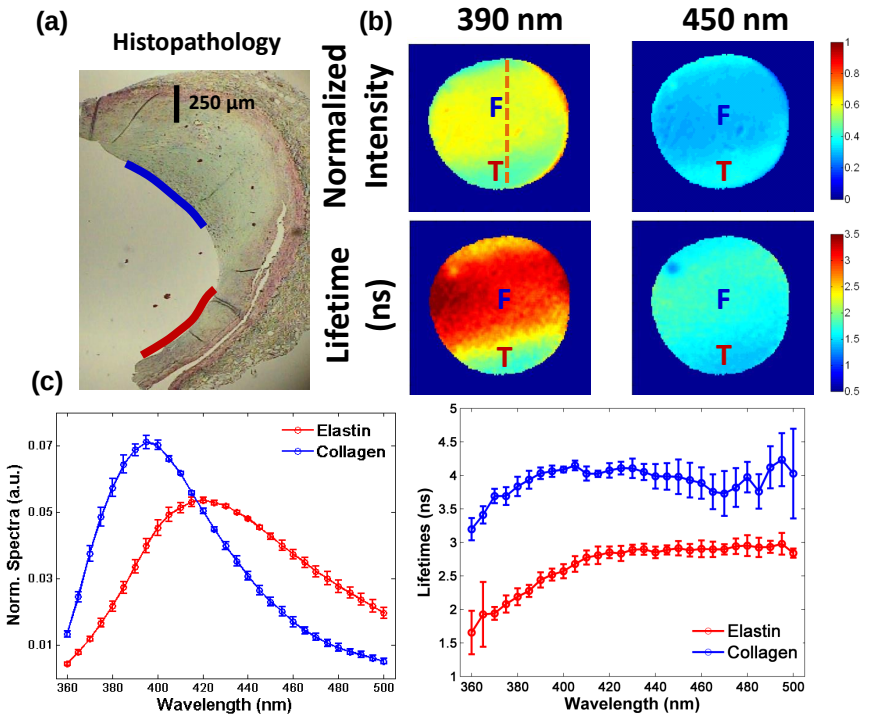

Figure 4.3: Analysis of FLIM images of a fibrotic plaque in human artery. (a) The plaque histopathology showing a thick fibrotic (F) collagen-rich plaque in the middle region of the arterial section (blue solid curved line), and a thinner (T) elastin and collagen-rich region towards the bottom side of the section (red solid curved line). (b) Normalized intensity and lifetime maps (top and bottom respectively) at 390 nm and 450 nm. (c) Normalized spectra and (d) lifetime values of collagen and elastin obtained from time-resolved fluorescence spectroscopy measurements.

was harvested from an autopsy case. The coronary artery was opened longitudinally for luminal imaging. The coronary plaques were imaged by placing the endoscope tip perpendicular to the lumen side, resulting in a circular field of view of ∼2 mm. The laser pulse energy at the tip of the excitation fiber probe was also adjusted to ∼5 μJ/pulse. The FLIM images from the coronary artery showing an atherosclerotic plaque are shown in Fig. 4.3. The artery histopathology (corresponding to a perpendicular section cut through the center of the FLIM field of view) showed a thick

fibrotic (F) collagen-rich plaque in the middle region of the arterial section (blue solid curved line), and a thinner (T) elastin and collagen-rich region towards the bottom side of the section (red solid curved line) as shown in Fig. 4.3 (a). Both the normalized intensity and lifetime maps showed two different regions (Fig. 4.3 (b)): a middle one (F) correlated to the fibrotic region and a bottom one (T) correlated to the thinner plaque. The contrast, however, was more dramatic for the 390 nm emission band. The normalized intensity at 390 nm was ∼60% for the middle (F) region and ∼40% for the bottom (T) region. On the other hand, the normalized intensity at 450 nm was smaller for the middle (F) region (∼30%) compared to the bottom (T) region (∼40%). The fluorescence lifetime at 390 nm was longer (∼3 ns) for the middle (F) region compared to the bottom (T) region (∼2 ns). On the other hand, the lifetime at 450 nm was in the range 1.5–2 ns for both regions. The intensity and lifetime maps at 550 nm (not shown) did not show any difference between the two regions, and were therefore not shown in Fig. 4.3. To correlate the artery fluorescence emission with those from purified collagen and elastin extracts, time-resolved fluorescence measurements of collagen and elastin were recorded and analyzed. The normalized spectra and lifetimes for the two fluorophores are also shown in Fig. 4.3 (c) & (d). The fluorescence spectra (normalized against the area under the curve) showed that the relative fluorescence intensity of collagen at in 390–400 nm range is almost twofold than that of elastin; while the relative fluorescence emission of elastin at 450 nm is almost 50% stronger than that of collagen. The fluorescence lifetime of collagen was

in the range of 2.5–3 ns for the entire emission spectrum; while for the lifetime increased from about 1.3 ns in the 390–400 nm range to almost 2 ns at 450 nm. Based on these characteristics, it was concluded that the thick plaque reflected the fluorescence emission of collagen, while the FLIM signal of the thinner part of the plaque reflected the fluorescence emission of both elastin and collagen.

4.6 Computational Performance

An important aspect of the present study that needs attention is the fact that a significant reduction in computation time could be achieved by compressing the the FLIM image (or FLIM data volume, to be more precise) without compromising the accuracy in the value of optimal α, as reported in Table 4.1. A compression factor (C.F.) of N means that the measured decays in a $N \times N$ region in FLIM data volume is replaced by a single decay equal to the average of all the replaced recorded decays (thus, a C.F of 1 would mean no compression). It was found that a compression factor of 3 applied to reduce the image size and speed up the optimization algorithm did not affect the estimation of the optimal values for α, while significantly reducing the computation time. Also, the computation time for 9-Cyanoanthracene (9CA) was much longer than for the other fluorophores. This is because the large lifetime ($\sim$11 ns) of 9CA demands an acquisition and processing of a larger sized FLIM data as compared to fluorophores with relatively shorter lifetimes. It must be noted that image compression is performed only to speed up the optimization of α. Once, we have the optimal value of α, the deconvolution is then performed on the uncompressed

image.

4.7 Conclusions

As stated in the introduction, the recorded decay at a given pixel of the FLIM image is mathematically modeled as a convolution of the instrument response with the IRF of the sample at that pixel. Thus, to estimate the IRF, the instrument response needs to be deconvolved from the recorded fluorescence decay at each pixel of the image. Accurate deconvolution becomes even more important when the width of the instrument response is comparable to the lifetime of the fluorescent sample. This observation was also clear from the results presented in Fig. 4.1 and Table 4.1, where we compared the lifetime estimates obtained through deconvolution against the case when no deconvolution was performed.

The proposed automated Laguerre deconvolution technique was successfully tested on a set of synthetic FLIM images covering a range of lifetime values (1–4 ns) derived from a bi-exponential model. The chosen lifetime range was significant, since a number of biologically relevant fluorophores have lifetimes in this range. The robustness of the proposed deconvolution method was demonstrated by its ability to accurately retrieve the IRFs at every pixel of the synthetic FLIM images covering a broad dynamic range under moderate and high noise conditions (40 and 25 dB SNR, respectively). The algorithm was also successfully tested on measured FLIM images from fluorescence lifetime standards. The fact that the lifetime values obtained by the Laguerre method for the fluorescence standards were very close to the

values reported in the literature confirms the accuracy of our method. Moreover, the results from the second experiment where multiple fluorescence lifetime standards were imaged together, further demonstrated the ability of the proposed algorithm to retrieve correct lifetime values from FLIM images that might have regions of different intensities and lifetimes.

We also demonstrated the applicability of the proposed technique on FLIM data obtained from a biological tissue. In this case, the proposed deconvolution algorithm produced lifetime maps having two regions with significantly different lifetimes. The lifetime values in the two regions, corroborated with the histopathological finding that the two regions correspond to a collagen-rich thick fibrotic plaque section and an elastin-rich thinner section of the plaque. This example has demonstrated the capability of FLIM to distinguish regions of different endogenous fluorophores, suggesting that it could be used as a potential optical technique in medical diagnosis. Moreover, the fact that the proposed technique is fast and automated makes it suitable for not only *ex-vivo* studies but also for *in-vivo* applications.

An important aspect of the proposed algorithm is that it optimizes a global value of the parameter α to fit a range of impulse response functions having different decay rates. In [35], Marmerelis discussed the empirical relationship between the optimal value of α and the memory of the nonlinear signal that is being estimated using the discrete Laguerre basis. Based on this, the author proposed a rather heuristic way of selecting the proper value of α for the estimation of nonlinear signals

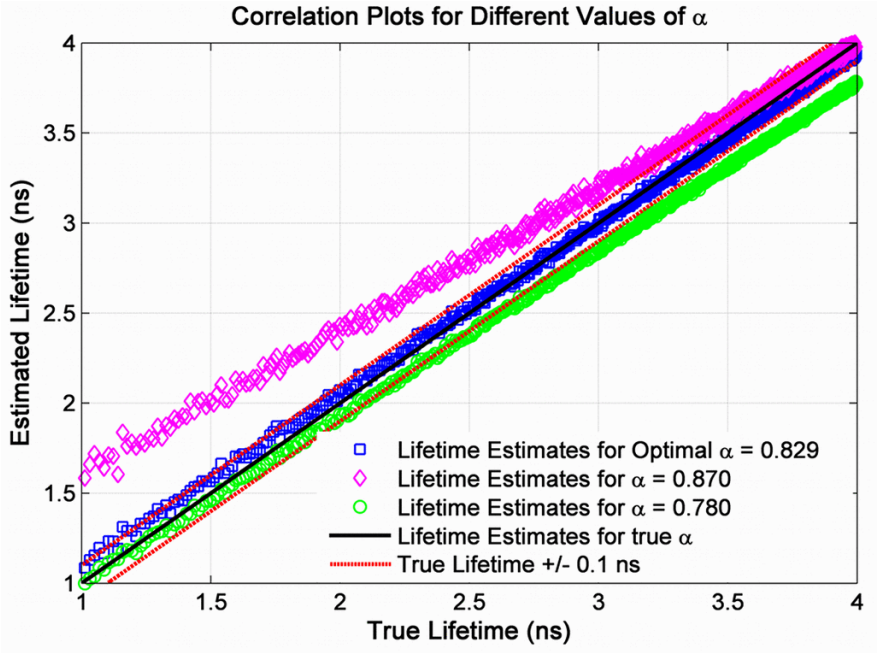

Figure 4.4: Plot showing the correlation between estimated and true lifetime values for different values of α

based on Laguerre kernel expansion. In the context of the research presented in this paper, the empirical relationship described in [35] translates to the fact that for a given order, fluorescence decays having longer lifetimes require larger values of α for proper representation within the Laguerre expansion framework; and decays having relatively shorter lifetimes require smaller values of α. This relationship is also evident from the lifetime and optimal α values presented in Table 4.1.

If one then extends this deduction to a case where it is required to estimate a set of fluorescence decays characterized by different lifetimes using a single value of α (which we have called the optimal α), a question that naturally arises is: how well do we expect to estimate different lifetimes using the same value of α? To answer this

question, let us reconsider the case where we validated the proposed algorithm on synthetic data, where we had a FLIM image with lifetime values ranging from 1 ns to 4 ns. The optimal value of α in this case was found to be 0.829 for a noise level of 40 dB. The correlation plot of the estimated *vs.* true lifetime for this optimal value shown in Fig. 4.1(e) is reproduced in Fig. 4.4 (blue squares). To study the effect of choosing a sub-optimal value of α for estimation of lifetimes, we deconvolved the noisy synthetic data with a value of $\alpha = 0.780$. The correlation plot for this value of α is also shown in Fig. 4.4 (green circles). Next, to study the effect of choosing a value of α that is greater than the optimal value, we perform the same process of deconvolving and plotting the correlation plot for $\alpha = 0.870$, which is shown in magenta diamonds in Fig. 4.4. We also plot the ideal correlation plot as a black solid line from 1 ns to 4 ns. It is clear from this plot that for a value of α greater than the optimal α, higher lifetimes are estimated much more accurately than shorter lifetimes (magenta diamonds); whereas for a sub-optimal value of α, shorter lifetimes are estimated more accurately than larger lifetimes (green circles). For the optimal α, we get an extremely accurate estimation of lifetime values around 2.8–3.2 ns. For lifetime values lying outside this range one either side, the estimate gets worse but stays confined within a small margin of 0.1 ns (shown as red broken line on either side of the solid black line). This means that the error in lifetime estimation for optimal value of α is at worse 0.1 ns for the entire range of 1–4 ns. The maximum error in the case of choosing a sub-optimal α was 0.2 ns and 0.6 ns for $\alpha = 0.780$ and

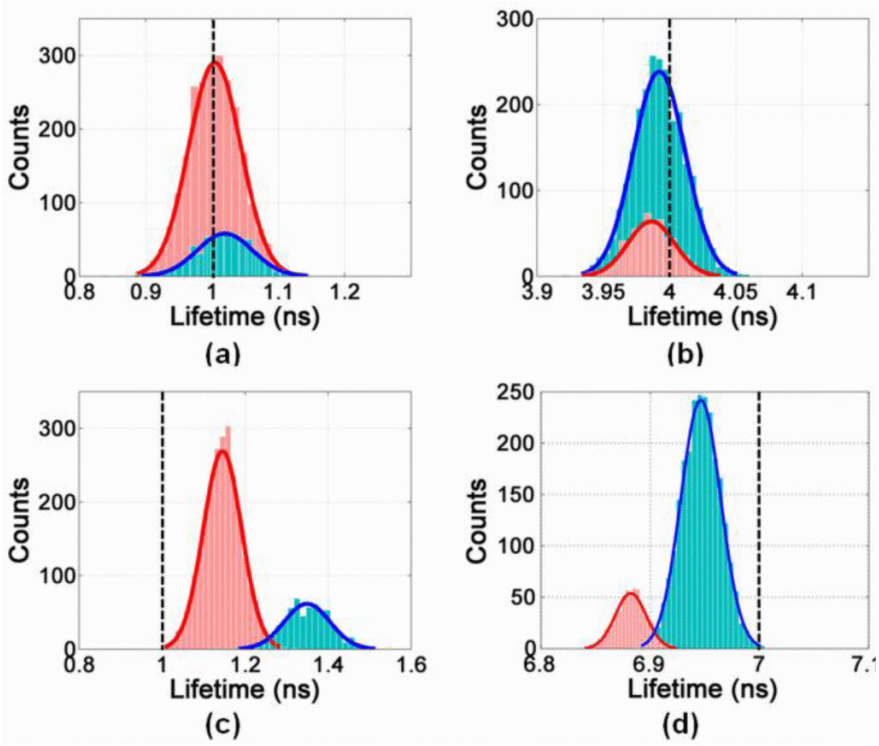

Figure 4.5: Results of the simulation study to test the lifetime dependence of the α parameter. (a) & (b) shows lifetime estimates for mixture 1a and 1b (not respectively). Blue histograms correspond to mixture 1a and red histograms correspond to mixture 1b. (d) & (c) shows lifetime estimates for mixture 2a and 2b, respectively. Blue histograms correspond to Mixture 2a and red histograms correspond to Mixture 2b. Black dotted line denotes the true lifetime value.

0.870, respectively. Thus, the best value of $\alpha = 0.829$ is optimal in a sense that it gives a reasonable error (maximum error $\sim$0.1 ns) in estimating the lifetimes over a range of lifetime values, which is smaller than that obtained for any other value of α.

The question that follows next is: how much error in lifetime estimates is acceptable? The answer is that in most applications where we one is interested in distinguishing different fluorophores based on their lifetime values, it depends on the

individual lifetimes of the constituent species as well as the range of the lifetime values. For example, in the case of the artery sample, the constituent fluorophores, collagen and elastin showing average lifetimes of $\sim$3 ns and $\sim$2 ns, respectively, in the 390 nm band, could be easily distinguished within a tolerance of 0.1 ns.

To study the sensitivity of α on relative concentration of constituent fluorophores and their lifetime, we perform a simple simulation study, where we simulate fluorescence decay maps for 4 different mixtures at 40 dB SNR, namely:

Mixture 1a 20% of $\tau = 1$ ns; 80% of $\tau = 4$ ns

Mixture 1b 20% of $\tau = 4$ ns; 80% of $\tau = 1$ ns

Mixture 2a 20% of $\tau = 1$ ns; 80% of $\tau = 7$ ns

Mixture 2b 20% of $\tau = 7$ ns; 80% of $\tau = 1$ ns

Since the cost function for α optimization is defined as the sum of cost functions for each pixel (see equation 4.10). We expect the estimation of α to be biased towards the component present in majority. Through simulations we find that it is indeed the case. Fig. 4.5 below shows the histograms of the estimated lifetimes for each of the 4 mixtures described above.

Several interesting observations can be made from this simulation study. Since every mixture above contains two lifetime components, the estimated lifetime of each component is biased in a way such that the lower lifetime is overestimated and the higher lifetime value is underestimated. Note that for mixture 1b, where the 1 ns

component is present in majority, bias in the lifetime estimation is smaller than the bias when the 1 ns component is in minority, as in mixture 1a (red histogram is less biased than blue histogram in Fig. 4.5 (a)). Similarly, for mixture 1a, where the 4 ns component is present in majority, the bias in lifetime estimation is smaller than the bias when the 4 ns component is in minority, as in mixture 1b (blue histogram is less biased than red histogram in Fig. 4.5 (b)). Same trend is observed for mixtures 2a and 2b where the lower and higher lifetime components have values 1 ns and 7 ns, respectively. This is shown in Fig. 4.5 (c)&(d). Moreover, bias in lifetime estimation in the case of mixtures that have widely spaced lifetime values are much higher than biases for mixtures where the lifetime values of the constituent species are not too widely spaced, i.e. bias in case of 1 ns and 7 ns mixture is more than the bias in case of 1 ns and 4 ns mixture. It is thus clear from these observations that the range of lifetime values of different species present in a mixture is more important than their relative proportions to decide whether the same value of α should be used for the entire mixture or should different regions of possibly different lifetimes be analyzed separately. It should be noted that the range 1–7 ns was used only for simulation purpose and that for most practical applications like tissue imaging, the range of lifetime values is not so wide and thus a single value of α would generally suffice.

Our validation results on FLIM data from fluorescence lifetime standards and tissue endogenous fluorophores show that the proposed algorithm is capable of finding an optimal value of α using non-linear least square optimization, which is then used

to find the optimal IRFs by estimating the LECs using linear least-squares approach. This is a significant improvement over previous implementation of the Laguerre deconvolution method, in which the values of α was determined by trial and error. The automated algorithm, however, takes more machine time than the standard Laguerre deconvolution method. This is not surprising, though, since the proposed algorithm performs an additional task of optimizing α as opposed to the standard Laguerre deconvolution that relies on a user provided value of α to perform the deconvolution. If computational time is a major concern for certain application, a significant improvement in speed can be achieved by performing the optimal search for α on a compressed FLIM data volume rather than the original uncompressed data, as discussed in an earlier section. The bottom line is that the optimization of α ensures an accurate and automated estimation of fluorescence IRFs. The proposed method thus offers an opportunity to perform an automated analysis of FLIM data and will, therefore, facilitate the use of FLIM in applications requiring minimal user intervention, such as *in-vivo* tissue imaging for clinical diagnosis. Also, because Laguerre basis functions have been used to model a wide variety of phenomena and systems, particularly in the areas of system identification [41, 42] and control theory [43], the application of the presented method is not limited to FLIM alone but to a wider variety of problems.

5. APPLICATION OF NON-NEGATIVE MATRIX FACTORIZATION TO MULTISPECTRAL FLIM DATA ANALYSIS*

5.1 Introduction

Despite several studies showing the potential of multispectral FLIM as a promising clinical optical imaging modality [44–47], its utility has not yet been fully established. One of the main reasons for this is the element of subjectivity involved in interpreting multispectral FLIM images. Existing methods of interpreting multispectral FLIM images are based on a qualitative comparison of spectral intensity and lifetime values at each pixel in a FLIM image with those of known fluorophores. Such comparison-based interpretation of FLIM images is satisfactory only when the fluorescence decay at each pixel can be attributed to primarily just one fluorophore. However, in most practical applications, there are often more than one fluorescing species contributing to the bulk fluorescence signal. In such cases, it becomes imperative to develop a method that can quantitatively characterize the type and relative abundance of fluorophores present in a sample. This is of particular interest

*Parts of this section have been reprinted, with permission, from:

1. P. Pande, B. E. Applegate, and J. Jo, "Application of non-negative matrix factorization to multispectral FLIM data analysis," *Biomedical Optics Express*, vol. 3, no. 9, pp. 2244–2262, 2012. ©2012 OSA

2. J. Park, P. Pande, S. Shrestha, F. Clubb, B. E. Applegate, and J. A. Jo, "Biochemical characterization of atherosclerotic plaques by endogenous multispectral fluorescence lifetime imaging microscopy," *Atherosclerosis*, vol. 220, no. 2, pp. 394–401, 2012. ©2012 Elsevier

in the context of biomedical diagnosis, since the progression from normal to pathological tissue is often characterized by changes in the relative abundance of tissue fluorophores.

Several studies reported in the literature that attempt to quantify the contributions of constituent fluorophores to bulk fluorescence signal, are based on lifetime measurements [48, 49]. In the general approach, it is assumed that the constituent fluorophores have mono-exponential decay dynamics with known lifetimes, and consequently the mixture fluorescence dynamics is modeled as a multi-exponential decay, wherein, each exponential component corresponds to a specific fluorophore. The sample fluorescence decay at each pixel is thus fitted to the corresponding multi-exponential model, and the estimated pre-exponential weights are used as surrogates for the relative contributions of the constituent fluorophores to the bulk fluorescence signal. When the lifetime values of the fluorophores are not known *a priori*, the global analysis approach is applied, in which the global fluorophore lifetimes are also estimated from the complete FLIM data [48].

Although generally used, these methods suffer from several limitations. First, the assumption of mono-exponential decay for each fluorophore is quite often inaccurate, since many exogenous and endogenous fluorophores show more complex decay profiles. For instance, Flavin Adenine Dinucleotide (FAD), which is an important cofactor in many enzymatic reactions, is known to have a non-exponential decay [22]. Similarly, for a single tryptophan protein, the distribution of protein conformations

results in a complex decay profile [50]. Second, most of these methods are restricted to two-component models [48, 51]; thus, they can only handle data in which at most two fluorescent species are being simultaneously monitored. These two major limitations have been identified in a number of publications. In particular, Veerver *et al.* have addressed these issues in [48], where the authors have stated that the "resolution of fluorophores with complex decays and separation of more than two fluorophores continues to be a topic of research". Third, from a computational aspect, accurate fitting of fluorescence decay data to a multi-exponential model requires signal-to-noise levels that are in many cases impractical for FLIM measurements [22]. Fourth, unless extremely short excitation light pulses are used, time deconvolution of the instrument response from the fluorescence decay data is required prior to lifetime estimation, which results in an additional computational burden. Lastly, all these methods are applicable to single spectral channel FLIM data and are thus unable to exploit the spectral information contained in the multispectral FLIM data [49, 52].

In this study, we present the application of non-negative matrix factorization (NMF) to multispectral FLIM data analysis. NMF is a multivariate data analysis technique that aims at extracting non-negative signatures and relative contributions of pure components from an additive mixture of those components; a process commonly referred to as unmixing [53]. In the context of FLIM data analysis, unmixing amounts to expressing the bulk fluorescence signal obtained from a sample as a weighted sum of fluorescence signals of the constituent fluorophores present in that

sample, where the weights correspond to the relative contributions of the constituent fluorophores to the bulk fluorescence signal. Unlike most other approaches mentioned earlier, which make assumptions about the functional form of the constituent fluorophore decay profiles and are restricted to two-component models, NMF is able to handle more than two fluorescent species showing complex decay dynamics (i.e. non-monoexponential decay). Another significant advantage of the NMF based approach is that it can be directly applied to raw multispectral FLIM intensity data, obviating the need to perform time-consuming deconvolution.

In the present study, the following two specific aims were accomplished. First, we proposed a new set of features to characterize multispectral FLIM data. This feature set (henceforth referred to as *NMF FLIM features*) comprises the relative abundance of constituent fluorophores derived *via* NMF of multispectral FLIM data. We also showed how these features are more intuitive and easy to interpret than the standard bulk intensity and lifetime features (henceforth referred to as *standard FLIM features*), which are currently used to characterize multispectral FLIM data. Second, we compared the performance of the NMF features against the standard FLIM features in terms of their ability to discriminate between three types of atherosclerotic plaques.

5.2 Materials and Methods

5.2.1 FLIM Instrumentation

The coronary segments were imaged using an in-house built high speed bench-top multispectral FLIM system reported in [29], and discussed in Section 3.1.1. Briefly, the scanning FLIM system was implemented following a direct pulse-recording scheme, in which the pixel rate could be equal to the laser repetition rate. A frequency tripled Q-switched Nd:YAG laser was used as the excitation source (355 nm, 30 kHz max. repetition rate, 1 ns pulse FWHM). The fluorescence emission was separated into three spectral channels using a set of dichroic mirrors and filters (390 ± 20 nm for collagen, 452 ± 22.5 nm for elastin, and 550 ± 20 nm for lipids). The emission from each channel was launched into fibers with different lengths (1 m, 10 m and 19 m) chosen to provide ∼45 ns interval between each emission band decay. The three consecutive decays were detected with a MCP-PMT (rise time: 150 ps) and sampled with a high bandwidth digitizer (1.5 GHz, 4 GS/s). The system's lateral resolution was measured to be 100 μm. Each multispectral FLIM image (FOV: 2×2 mm^2 at 60×60 pixels) was acquired in ∼7 s.

5.2.2 Tissue Sample Preparation and Histopathological Evaluation

The coronary artery tissue database described in Section 3.2.1 was used in this study. Based on the histopathological evaluation, each section was classified as: intimal thickening (IT), pathological intimal thickening (PIT), fibroatheroma (FA),

thin-cap fibroatheroma (TCFA), calcified plaque (CA), and/or plaque with significant foam-cell (FC) infiltration [12]. A total of 21 segments showing similar and uniform histopathological characteristics in all consecutive sections were selected and grouped either as High-Collagen (HC; including FA and PIT), High-Lipids (HL; including TCFA and PIT with significant foam-cell infiltration or FC-PIT) or Low-Collagen/Lipids (LCL; including IT and CA). We shall refer to these datasets as the *homogeneous datasets* while the remaining 37 datasets shall be called the *heterogeneous datasets*.

5.2.3 Multispectral FLIM Data in NMF Framework

Before setting out to describe the problem statement, the following notations are in order. We shall denote the multispectral fluorescence intensity decay measured at a given pixel (x, y) as a function of time (t) and wavelength band (λ_i) by $I(x, y, t; \lambda_i)$. If we linearly index, say N pixels in a multispectral FLIM image as $i = 1, 2, \ldots, N$, such that the i th index corresponds to the pixel (x, y), and if we denote the spectro-temporal FLIM profile at the ith pixel by $\mathbf{x}_i$, then we define this spectro-temporal decay as a concatenation in time of the fluorescence decays for all emission bands; i.e., $\mathbf{x}_i \equiv I(x, y, t; \lambda_1, \lambda_2, \ldots, \lambda_P) = [\, I\,(x, y, t; \lambda_1)\,, I(x, y, t; \lambda_2), \ldots, I(x, y, t; \lambda_P)\,]$, where P denotes the number of emission bands. Let us also assume that in a sample there are K fluorophores, termed *end-members* having multispectral time resolved fluorescence decays denoted by $\mathbf{s}_k \in \mathbb{R}^T$, for $k = 1, 2, \ldots, K$, where T denotes the length of the spectro-temporal signals. In accordance with the hyperspectral imaging

terminology, we shall interchangeably refer to these end-member profiles as *end-member signatures*. If we denote the multispectral time resolved fluorescence signal recorded at a given pixel (say nth pixel) in a FLIM image by $\mathbf{x}_n$, then under the linear mixing assumption, $\mathbf{x}_n$ can be expressed as a linear combination of the K end-member signatures, i.e.

$$\mathbf{x}_n = a_{1,n}\ \mathbf{s}_1 + a_{2,n}\ \mathbf{s}_2 + \cdots + a_{K,n}\ \mathbf{s}_K \ \Leftrightarrow\ \mathbf{x}_n = \mathbf{S}\mathbf{a}_n, \tag{5.1}$$

where $\mathbf{S} \equiv [\mathbf{s}_1,\ \mathbf{s}_2, \cdots, \mathbf{s}_K] \in \mathbb{R}^{T\times K}$ and $\mathbf{a}_n \equiv [a_{1,n},\ a_{2,n},\ \cdots, a_{K,n}]^T \in \mathbb{R}^K$. Here, the weights: $a_{1,n}, a_{2,n}, \ldots, a_{K,n}$ represent the contributions or abundances of the K end-members at the nth pixel. We we can then express the *data matrix*: $\mathbf{X} \equiv [\mathbf{x}_1, \mathbf{x}_2, \cdots, \mathbf{x}_N] \in \mathbb{R}^{T\times N}$, containing the recorded spectro-temporal fluorescence decays from N pixels along its columns (henceforth referred to as *data vectors*) in matrix notation as $\mathbf{X} = \mathbf{S}\mathbf{A}$. We shall call $\mathbf{S} \equiv [\mathbf{s}_1,\ \mathbf{s}_2, \cdots, \mathbf{s}_K]$,the *mixing matrix*, which holds the K end-member signatures in its columns; and $\mathbf{A} \in \mathbb{R}^{K\times N}$ shall be referred to as the *abundance matrix*, which contains the contributions of K end-members (along rows) for each of the N pixels (along columns). Taking into account that matrices $\mathbf{X}, \mathbf{S}$ and $\mathbf{A}$ contain non-negative elements (denoted by: $\mathbf{X}, \mathbf{S}, \mathbf{A} \succcurlyeq 0$), the problem we attempt to address can be stated as follows: Given a non-negative data matrix $\mathbf{X}$ and the number of fluorophores K contributing to the bulk fluorescence signal, find the mixture and the abundance matrices $\mathbf{S}, \mathbf{A} \succcurlyeq 0$ such that the product $\mathbf{S}\mathbf{A}$ best approximates $\mathbf{X}$; i.e. $\mathbf{X} \approx \mathbf{S}\mathbf{A}$. This problem is more generally known as non-

negative matrix factorization and appears in several research areas under different names, most notably, spectral unmixing or blind source separation in hyperspectral image analysis and multivariate curve resolution in chemometrics [54, 55].

5.2.4 Geometrical Interpretation, Preprocessing and NMF Algorithms

5.2.4.1 Geometrical Interpretation

The solution to the NMF problem stated in the previous section can be better understood by resorting to a geometrical interpretation of NMF. For meaningful interpretation, the rows of $\mathbf{A}$ are interpreted to represent the relative abundance of different end-members, in which case, they are assumed to follow a full-additivity constraint, i.e. $\sum_{k=1}^{K} a_{k,n} = 1$ for $n = 1, 2, \ldots, N$ (in the following section, we discuss how a simple normalization procedure can be employed to ensure that the full-additivity constraint is satisfied). Under the linear mixing, non-negativity, and full-additivity constraints, it then follows that the set $\mathfrak{X} \equiv \left\{\mathbf{x}_n \in \mathbb{R}^T : \mathbf{x}_n = \mathbf{S}\mathbf{a}_n,\ \mathbf{1}^T\mathbf{a}_n = 1,\ n = 1, 2, \ldots, N\right\}$ represents a $K-1$ dimensional simplex and estimating $\mathbf{S}$ amounts to finding the vertices of this simplex. This is shown in Fig. 5.1 and Fig. 5.2 for cases when $K = 2$ and $K = 3$, respectively.

5.2.4.2 Data Preprocessing

The full-additivity constraint mentioned earlier, is not always satisfied in many practical situations. This may happen when either the imaged area is large or in situations where it is desired to use data acquired from different imaging sessions. In

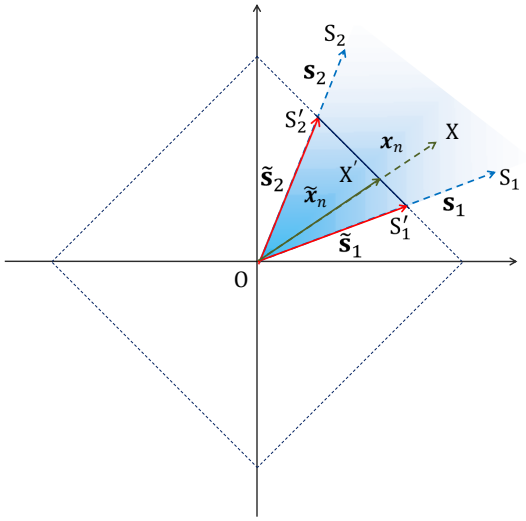

Figure 5.1: Data normalization to satisfy the full-additivity constraint. All possible non-negative linear combinations of $\mathbf{s}_1$ and $\mathbf{s}_2$ lie in the blue shaded unbounded area contained within $\mathbf{s}_1$ and $\mathbf{s}_2$. $\mathbf{x}_n$ represents one such data vector. Normalizing data vectors to unit L_1-norm length amounts to rescaling them such that the tip of the rescaled data vectors lie on the portion of the unit L_1 norm circle (shown in dotted lines) contained between the normalized end-member signatures $\widetilde{\mathbf{s}}_1$ and $\widetilde{\mathbf{s}}_2$, i.e. on the line $S'_1S'_2$, which represents a 1-D simplex.

the former case, it is mainly the variations in physical and chemical conditions, while in the the latter case, it is the differences in experimental conditions that results in the violation of the full-additivity constraint. This effect is commonly referred to as *signature variability* in hyperspectral imaging literature and is characterized by what is called spectral shape invariance, which means that although the shapes of the end-member signatures do not vary much across different pixels, their scaling or amplitude vary significantly over the imaged area [56]. In such a case, instead of being contained *on* a $K-1$ dimensional simplex, the data lies within a region of the positive orthant of a T dimensional space enclosed by a convex polygonal

cone spanned by the K columns of $\mathbf{S}$. This is shown in Fig. 5.1 and Fig. 5.2 for the case when $K = 2$ and $K = 3$, respectively, where the data vectors lie within the cone (shown as blue shaded region) spanned by the end-member signatures, as opposed to lying on a line ($K = 2$) and a triangular plane ($K = 3$), respectively. In cases like these, a normalization technique inspired from the dark point fixed transform (DPFT) can be performed to ensure that the normalized data satisfies the full-additivity constraint [57,58]. This normalization involves scaling the data vectors $\mathbf{x}_n$ to have unit length in the L_1-norm sense, i.e. if $\widetilde{\mathbf{x}}_n$ denotes the normalized data vector, then $\widetilde{\mathbf{x}}_n = \mathbf{x}_n / \|\mathbf{x}_n\|_1$, where $\|\mathbf{x}\|_1$ for a vector $\mathbf{x} = (x_1, x_2, \ldots, x_n)$ is defined as: $\|\mathbf{x}\|_1 := |x_1| + |x_2| + \cdots + |x_n|$. The linear mixing model stated in Eq. (5.1) can then be reformulated as:

$$\widetilde{\mathbf{x}}_n = \frac{\mathbf{x}_n}{\|\mathbf{x}_n\|_1} = \frac{\sum_{k=1}^{K} a_{k,n}\mathbf{s}_k}{\|\mathbf{x}_n\|_{\mathbf{1}}} = \sum_{k=1}^{K} \underbrace{\left(a_{k,n}\frac{\|\mathbf{s}_k\|_1}{\|\mathbf{x}_n\|_1}\right)}_{\widetilde{a}_{k,n}} \underbrace{\left(\frac{\mathbf{s}_k}{\|\mathbf{s}_k\|_1}\right)}_{\widetilde{\mathbf{s}}_k} = \sum_{k=1}^{K} \widetilde{a}_{k,n}\widetilde{\mathbf{s}}_k, \qquad (5.2)$$

where, $\widetilde{\mathbf{s}}_k = \mathbf{s}_k / \|\mathbf{s}_k\|_1$ denotes the rescaled end-member signatures and $\widetilde{a}_{k,n}$ denotes the corresponding rescaled contributions. Observing that $\|\mathbf{x}_n\|_1 = \sum_{k=1}^{K} a_{k,n}\|\mathbf{s}_k\|_1$, it follows immediately that $\sum_{k=1}^{K} \widetilde{a}_{k,n} = 1$. The meaning of the term "relative abundance" can now be better understood if we reconsider the NMF problem: $\mathbf{X} = \mathbf{SA}$, where it is assumed that the row entries of a given column of $\mathbf{S}$ sum to 1; an assumption that follows from the preceding discussion on normalization. In this case, the relative abundance of an end-member (say kth) at a given pixel (say nth) can

be interpreted as the relative contribution of the end-member's signature signal (kth column of $\mathbf{A}$) to the bulk signal measured at the nth pixel (nth column of $\mathbf{X}$).

The aforementioned normalization technique can also be understood intuitively by considering a simple case, where we have a mixture of 2 end-members ($K = 2$), for which the end-member signatures $\mathbf{s}_1$ and $\mathbf{s}_2$ are represented as vectors OS_1 and OS_2 in Fig. 5.1. In a 2-D space, the unit L_1-norm circle (set of vectors of norm 1) is a square, which is shown in dotted lines in Fig. 5.1. Now, under the non-negativity and linear mixing assumptions, a data vector $\mathbf{x}_n$, denoted by OX lies inside the blue shaded region spanned by OS_1 and OS_2. The effect of normalizing a vector to unit length in L_1-norm sense can be thought of as scaling the length of that vector so that the tip of the vector falls on the unit L_1-norm circle. Thus, the normalized vector $\widetilde{\mathbf{x}}_n$ is simply a scaled version of the original vector $\mathbf{x}_n$ and is denoted by OX'. By a similar reasoning, the normalized end-member signatures, $\widetilde{\mathbf{s}}_1$ and $\widetilde{\mathbf{s}}_2$ (denoted by vectors OS_1' and OS_2') also lie on the unit L_1-norm circle, whence it follows that any vector expressed as a non-negative linear combination of $\mathbf{s}_1$ and $\mathbf{s}_2$ (or lying in the blue shaded region) upon normalization will fall on the line joining S_1' and S_2', which represents a 1-D simplex.

5.2.4.3 NMF Algorithms

A class of algorithms to perform NMF is based on the above mentioned geometrical interpretation of linear mixing model. These algorithms can be broadly grouped into two categories. The first category includes algorithms that are based on the

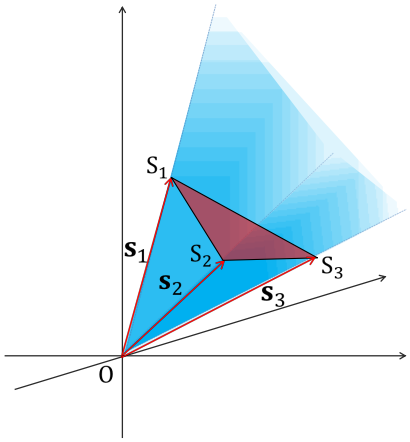

Figure 5.2: Simplex structure of data satisfying the non-negativity and full-additivity constraint. In the general case, all possible non-negative linear combinations of $\mathbf{s}_1$ $\mathbf{s}_2$ and $\mathbf{s}_3$ lie in the blue shaded unbounded volume enclosed by $\mathbf{s}_1$ $\mathbf{s}_2$ and $\mathbf{s}_3$. On imposing the full-additivity constraint all possible non-negative linear combinations of $\mathbf{s}_1$ $\mathbf{s}_2$ and $\mathbf{s}_3$ are constrained to lie on the triangle $S_1S_2S_3$, which represents a 2-D simplex.

assumption that the set containing the end-member signatures $\mathfrak{S} \equiv \{\mathbf{s}_k \in \mathbb{R}^T,\ k = 1, 2, \ldots, K\}$ is a subset of the set $\mathfrak{X} \equiv \{\mathbf{x}_n \in \mathbb{R}^T,\ n = 1, 2, \ldots, N\}$ containing the data vectors. This means that there are at least K pixels denoted by $n_1, n_2, \ldots, n_K$ such that $\mathbf{x}_{n_i} = \mathbf{s}_i$, for $i = 1, 2, \ldots, K$. This assumption is commonly referred to as the pure pixel assumption and it simply means that the vertices of the simplex described by the set of points in $\mathfrak{X}$ are contained in $\mathfrak{X}$. The problem of estimating end-member signatures is then reduced to finding the data vectors that form the vertices of the simplex. Some popular algorithms based on this assumption are Vertex Component Analysis (VCA), Pixel Purity Index (PPI) and N-FINDR [59–61]. The second category of NMF algorithms deal with a more realistic and difficult sit-

uation, where the end-members appear rarely as pure pixels or, in other words, the observed pixels are mostly a mixture of end-members. In such a case, the data does not span the entire simplex and not many observed pixels are found at the vertices of the simplex. The basic idea behind these algorithms is that even in the absence of pure pixels, it may be possible in many cases to deduce the simplex structure of the data. This idea was described in [62], where the author introduced a Minimum Volume Transform (MVT) to infer the simplex structure in the absence of pure pixels. Based on the idea of MVT, several unmixing algorithms have been proposed in the literature [58, 63, 64]. In this research, we present the application of Simplex Identification via Split Augmented Lagrangian (SISAL) [65] to find the vertices of a minimum volume simplex that encloses the multispectral FLIM data subject to the non-negativity and full-additivity constraints, as discussed next.

Let us assume that the T dimensional data vectors are represented in a K dimensional subspace. If we denote the lower dimensional analogues for matrices $\mathbf{X}$ and $\mathbf{S}$ by $\mathcal{X}$ and $\mathcal{S}$, then the volume of the $K-1$ dimensional simplex embedded in K dimensions is $|det(\mathcal{S})|$. Furthermore, if we define $\mathcal{Q} \equiv \mathcal{S}^{-1}$, then the optimization problem that SISAL attempts to address can be mathematically stated as:

$$\begin{aligned} \arg\max_{\mathcal{Q}} \quad & -log\,|det(\mathcal{Q})| \\ \text{subject to:} \quad & \mathcal{Q}\mathcal{X} \succcurlyeq \mathbf{0},\ \mathbf{1}_K^T \mathcal{Q}\mathcal{X} = \mathbf{1}_N^T. \end{aligned} \tag{5.3}$$

In order to account for outliers and noise in the data, the full-additivity hard con-

straint is replaced by a soft constraint, which results in the following modified optimization problem:

$$\begin{aligned} \arg\max_{\mathcal{Q}} \quad & -log\left|det\left(\mathcal{Q}\right)\right| + \lambda\|\mathcal{Q}\mathcal{X}\|_h \\ \text{subject to:} \quad & \mathbf{1}_K^T\mathcal{Q}\mathcal{X} = \mathbf{1}_N^T, \end{aligned} \tag{5.4}$$

where $\|\mathbf{Y}\|_h \equiv \sum_{ij} \max\{-[Y]\}_{ij},\ 0\}$ and $\lambda > 0$ is the regularization parameter. The optimization problem stated in Eq. (5.4) can be solved using a set of sequential quadratic programming problems as discussed in [65]. An efficient MATLAB implementation of SISAL algorithm is made publicly available by the authors of [65] on their website.

5.2.5 Feature Extraction and Classification

5.2.5.1 Feature Extraction

A total of 58 arterial tissue samples were imaged over a 2 mm $\times$ 2 mm FOV by the multispectral FLIM system described earlier, generating a database of 58 multispectral FLIM data cubes of size 60 $\times$ 60 $\times$ 768 ($x \times y \times t; \lambda_1, \lambda_2, \lambda_3$). The 3-D multispectral FLIM image cubes were then processed to obtain two sets of 2-D feature maps, namely, the standard FLIM features and the NMF FLIM features. The process of obtaining the standard FLIM feature has been described in Section 2.3 (also see Fig. 2.4). The process of obtaining NMF FLIM features is outlined in Fig. 5.3. To perform NMF on multispectral FLIM data, the first step was "unfolding" the multispectral FLIM data cube, which involved reshaping the 3-D data cube

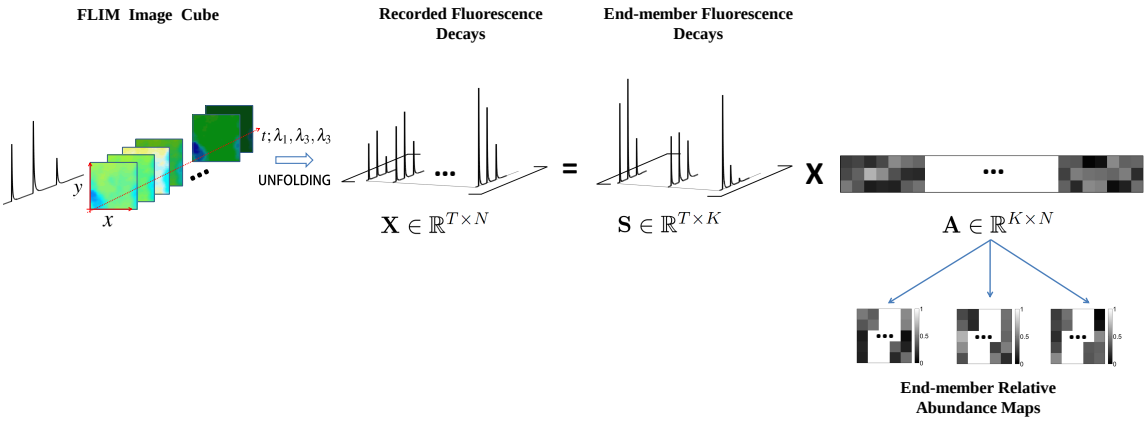

Figure 5.3: Schematic showing the process of performing NMF on a multispectral FLIM data cube. The 3-D spectro-temporal cube is unfolded and normalized to obtain a 2-D data matrix $\mathbf{X}$. The data matrix is then factorized to yield the mixing matrix $\mathbf{S}$ and the relative abundance matrix $\mathbf{A}$, columns of which are reshaped to obtain end-member relative abundance maps. These abundance maps comprise the NMF FLIM features.

$(x \times y \times t; \lambda_1, \lambda_2, \lambda_3)$ to form a 2-D data matrix $(t; \lambda_1, \lambda_2, \lambda_3 \times xy)$. The data matrix thus obtained was then normalized by using the DPFT and subsequently factorized using the SISAL algorithm to yield a mixing matrix that contains the end-member signatures and an abundance matrix. As shown in Fig. 5.3, rows of the abundance matrix were reshaped to yield relative abundance maps for the end-members. These maps constitute the NMF FLIM features. The performance of the two sets of features was evaluated in terms of their ability to characterize multispectral FLIM images by training and testing a multinomial logistic regression classification model (described in the next section) on a subset of 21 out of 58 multispectral FLIM datasets (homogeneous datasets). Furthermore, to obtain pixel level classification, each pixel of a FLIM image was considered to be a data-point, yielding a labeled data set of

$21 \times 60 \times 60$ data-points. The classification performance for the logistic regression model obtained from each set of features was compared by estimating the 10 fold cross-validation (CV) misclassification error.

5.2.5.2 Multinomial Logistic Regression

Supervised classification is the problem of deriving a set of rules from a set of pre-classified data and using that rule to classify a new data-point. The set of pre-classified data-points along with the class for each data-point is called the training set $\mathcal{T} = \{(\mathbf{z}_1, \mathbf{y}_1), (\mathbf{z}_2, \mathbf{y}_2), \ldots, (\mathbf{z}_N, \mathbf{y}_N)\}$, where $\mathbf{z}_n$ is referred to as the feature vector for the nth data point and $\mathbf{y}_n = [\, y_{n,1}, y_{n,2}, \ldots, y_{n,C}]$ is a $1 \times C$ vector such that $y_{n,c} = 1$ if the nth data point belongs to cth class, and 0 otherwise. Multinomial logistic regression is a supervised classification method that models the posterior probability of a data point belonging to one of the C possible classes as a linear function of $\mathbf{z}$ [66, 67]. By fixing one of the classes as the baseline class, the conditional log-odds of other classes with respect to the baseline class have the form:

$$\log \frac{\Pr(\text{Class} = c|\mathbf{Z} = \mathbf{z})}{\Pr(\text{Class} = C|\mathbf{Z} = \mathbf{z})} = \beta_{c,0} + \boldsymbol{\beta}_c^T \mathbf{z}, \qquad c = 1, 2, \ldots, C-1, \tag{5.5}$$

where the Cth class is assumed to be the baseline class. The special form of logistic regression model ensures that the posterior probabilities sum to 1, i.e.

$$\sum_c \Pr\left(\text{Class} = c|\mathbf{Z} = \mathbf{z}\right) = 1$$

. The problem of fitting a logistic regression model amounts to solving the maximum likelihood problem defined as:

$$\ell(\boldsymbol{\beta}) = \sum_{n=1}^{N} \sum_{c=1}^{C-1} y_{n,c} \log \frac{\exp(\beta_{c,0} + \boldsymbol{\beta}_c^T \mathbf{z}_n)}{1 + \sum_c \exp(\beta_{c,0} + \boldsymbol{\beta}_c^T \mathbf{z}_n)}, \tag{5.6}$$

where, the maximum likelihood estimate for the model parameter

$$\boldsymbol{\beta} \equiv (\beta_{1,0}, \boldsymbol{\beta}_1, \beta_{2,0}, \boldsymbol{\beta}_2, \ldots, \beta_{C-1,0}, \boldsymbol{\beta}_{C-1})$$

is obtained through an iterative optimization procedure like Newton-Raphson method [67, 68]. The model thus obtained is then used to predict the posterior probability of a given data- point belonging to one of the C classes and consequently assigning it to the class with the maximum probability.

5.3 Results

5.3.1 Validation on Simulated Data

The proposed method was first validated on simulated multispectral FLIM data, to which effect 10,000 data vectors ($N = 10,000$) representing artificial mixtures of collagen, lipids and elastin ($K = 3$) were generated. Collagen, lipids and elastin are the dominant endogenous fluorophores in arteries and are thus relevant to the present study. The end-member profiles for collagen, lipids and elastin ($T = 510$) were simulated based on the expected intensity and lifetime values for these fluorophores

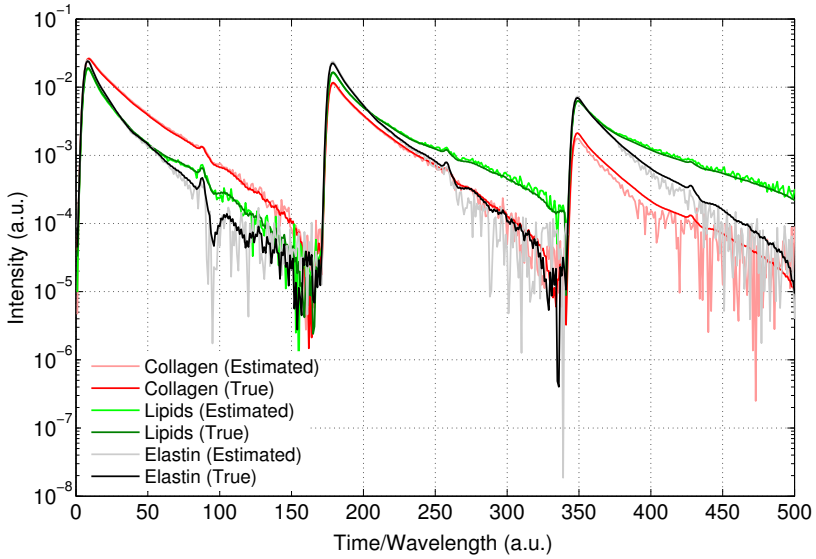

Figure 5.4: True end-member profiles (dark shade) plotted over estimated profiles (light shade) for the simulation study. The profiles are plotted on a semilog (y) axis to highlight the differences between the two profiles that were indistinguishable on a linear scale.

obtained from a time resolved fluorescence study [28]. These profiles constituted the **S** matrix and are referred to as the "true end-member profiles". To form the relative abundance matrix **A**, values for relative abundances were obtained by sampling from a uniform distribution and subsequent normalization to enforce full-additivity. To ensure that the data does not contain any pure pixel, data vectors having relative abundance greater than 0.7 for any end-member were discarded. Finally, an additive white Gaussian noise was added to simulate a SNR of 15 dB. To quantify the performance of the algorithm on simulated data, 5 realizations of the noisy data were

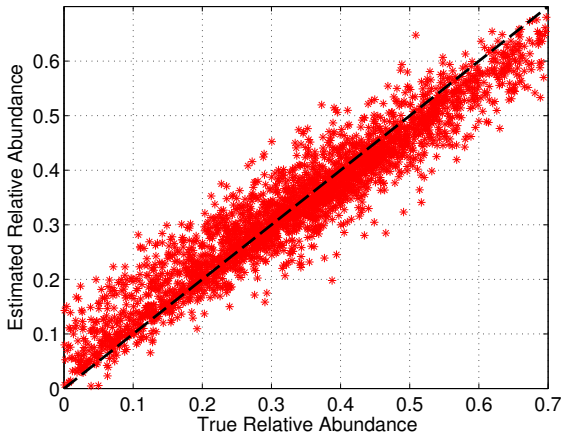

Figure 5.5: Scatter plot showing good agreement between the estimated and true relative abundances. Black dashed line represents the line of perfect fit ($y = x$).

generated and the weighted mean absolute percent error (WMAPE), defined as:

$$\text{WMAPE} = \frac{\sum_{n=1}^{N} \left| \frac{x_n - \tilde{x}_n}{x_n} \right| \cdot x_n}{\sum_{n=1}^{N} x_n} \times 100\% \tag{5.7}$$

was calculated for $\mathbf{S}$ and $\mathbf{A}$ for each realization. The WMAPE in estimating $\mathbf{A}$ and $\mathbf{S}$ was found to be 15.81 ± 0.42 and 9.67 ± 0.81 (mean $\pm$ standard error), respectively, indicating good agreement between the actual and estimated values. Figure 5.4 shows the true end-member profiles plotted along with the estimated profiles for a representative realization of the noisy data. The profiles are plotted on a semilog graph to highlight the differences between the two profiles that were not evident on a linear scale. The plot indicates good agreement between the two profiles. Likewise, a scatter plot shown in Fig. 5.5 also indicates good match between the estimated and

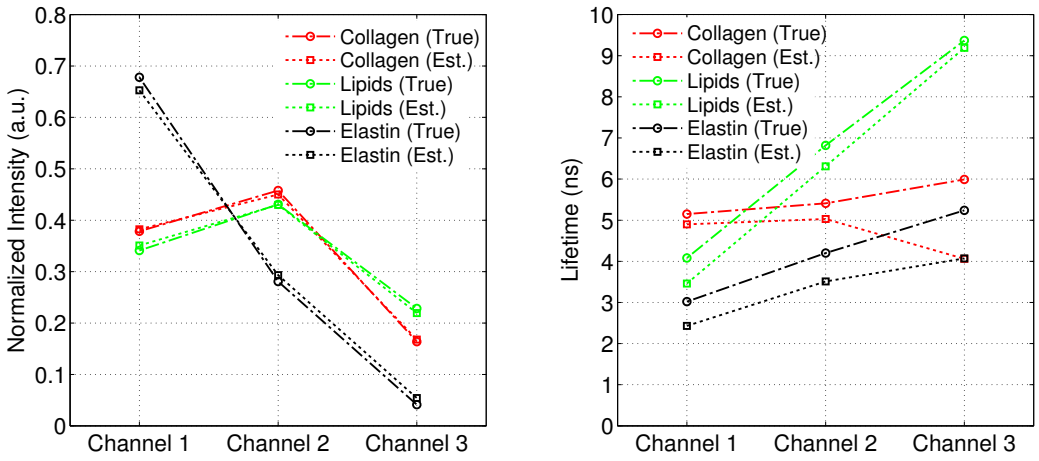

(a) (b)

Figure 5.6: Comparison of the true and estimated normalized intensities and lifetimes for collagen, elastin, and lipids in the three emission channels. (a) Normalized intensity and (b) lifetimes in the three channels for the true and estimated end-member profiles. Results indicate good agreement between the spectro-temporal characteristics of the two profiles.

true relative abundances. To further compare the estimated profiles with the true profiles, the normalized intensity and lifetimes in the three channels estimated from the profiles are plotted in Fig. 5.6 (a) and (b) respectively. These plots suggest a good match between the spectro-temporal characteristics of the true and estimated end-members. The large mismatch between collagen's lifetime in the third channel is possibly a consequence of low signal level in collagen's spectro-temporal profile in the third channel.

5.3.2 Validation on Experimental Data: Feature Extraction

The method was also validated on experimental multispectral FLIM data obtained from fresh human postmortem atherosclerotic coronary plaques. Standard

and NMF FLIM features were extracted from the multispectral FLIM database through the procedure outlined in the methods section. The end-member profiles obtained *via* NMF are shown in Fig. 5.8. The profile in red (solid line) has maximum emission intensity in the first channel followed by a relatively lower intensity in the second channel and least intensity in the last channel. This intensity trend is characteristic of collagen. Likewise, the green (dotted line) and black (dashed line) profiles have relatively same intensity in the first two channels but a lower intensity in the third channel, which is characteristic of both lipids and elastin as shown in the steady state spectra in Fig. 5.10 (a) (also [28]). To identify the end-members, we deconvolved the decay profile corresponding to the dominant emission band for each end-member and estimated the average lifetime from the deconvolved decays. This is shown in Fig. 5.10 (b), where the log-transformed deconvolved profiles, $\log_e(I(t))$ are plotted against time, t. In the case of a mono-exponential decay, the log-transformed plots would be expected to be straight lines. Deviation from a straight line indicates complex nature of decay kinetics. To estimate average lifetime from these plots, a straight line fit based on least squares estimation was obtained and the average lifetime was estimated by calculating -1/slope of the best fit line. Based on the intensity trends and lifetime values, the three end-member profiles were identified as collagen (red, $\tau_{avg} = 7.1\,\text{ns}$), lipids (green, $\tau_{avg} = 10.8\,\text{ns}$) and elastin (black, $\tau_{avg} = 2.6\,\text{ns}$).

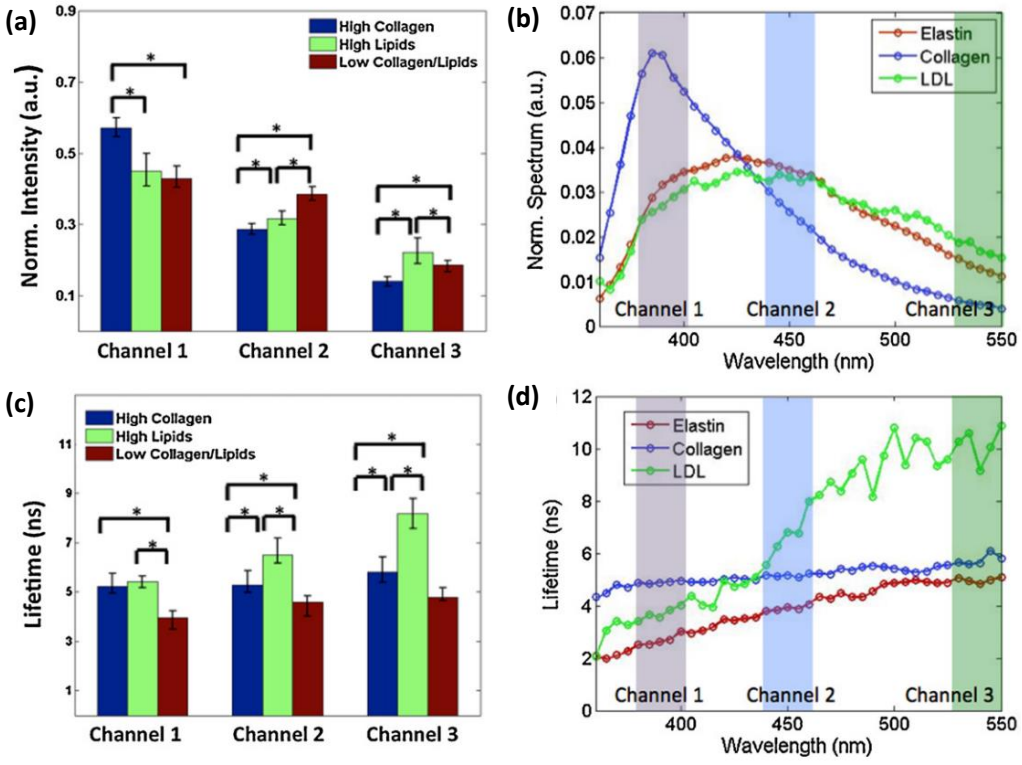

Figure 5.7: Results of the statistical analysis on the standard FLIM features. The values of the normalized fluorescence intensity in the three spectral channels from the HC, HL and LCL groups (a) resemble the fluorescence emission spectra from collagen, LDL and elastin, respectively (b). Similarly, the values of the fluorescence lifetime from the HC, HL and LCL groups (c) resemble the fluorescence lifetime from collagen, LDL and elastin, respectively (d).

5.3.3 Standard FLIM Features

The ability of the six standard FLIM features (normalized intensity and lifetime in the three channels) to distinguish between the three histopathological classes was assessed *via* the following statistical analysis. A 15×15 pixel block in each FLIM image was counted as a single data point to reduce the effect of non-normality. The nonparametric MannWhitney U-test was performed between every pair of classes,

wherein $P < 0.01$ was considered significant. Results of the statistical analysis are summarized in Fig. 5.7 (a)&(c). The bar plots denote the median value and the error bars denote the first and third quartiles. For comparison, the plots of wavelength dependent normalized emission spectrum and average lifetimes from purified collagen, elastin and (low density lipoproteins) LDL measured with a time-resolved spectroscopy system are also shown in Figure 5.7 (b)&(d). The median values for the normalized intensity and lifetime for the HC and HL samples resemble those of collagen and LDL respectively (characteristic strong emission in Channel 1 for collagen and long lifetime in Channel 3 for LDL). The horizontal brackets above the bars indicate significant difference among pairs (P<0.01).

5.3.4 Comparison of Standard FLIM and NMF Features

The two sets of features corresponding to a representative HC, HL and LCL plaque from the homogeneous datasets are shown in Fig. 5.9. In each sub-figure, the top row (A)-(C) shows the normalized fluorescence intensity maps for the three spectral channels. Likewise, the second row (D)-(F) shows the lifetime maps for the three channels. The relative abundance maps of the three end-members, namely, collagen, lipids and elastin, constitute the NMF FLIM features that are shown in the third row (G)-(I). Representative histopathological sections for each plaque type are also shown in the last row (J) of each sub-figure. For the HC plaque (Fig. 5.9 (a)), the fluorescence intensity was stronger in channel 1 than in channels 2 and 3, and the average lifetime varied between 5–6 ns, which resembles the fluorescence emission

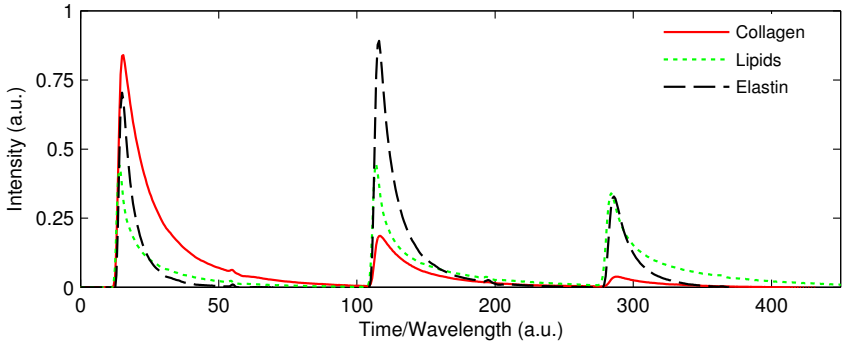

Figure 5.8: End-member signatures obtained from the artery multispectral FLIM data. Based on the spectro-temporal characteristics, the end-members were identified as collagen (red, solid line), lipids (green, dotted line) and elastin (black, dashed line).

characteristics of collagen. In the histopathological section, the light blue stain color indicates the presence of collagen. The relative abundance maps in this case, showed higher abundance of collagen (0.61 ± 0.04) as compared to that of lipids (0.25 ± 0.04) and elastin (0.17 ± 0.02). For the HL plaque (Fig. 5.9 (b)), the fluorescence intensity, compared to the HC plaque, was lower in channel 1, similar in channel 2 and higher in channel 3. The averaged lifetime gradually increased from $\sim$5 ns in channel 1 to $\sim$8 ns in channel 3. In the histopathological section, the empty areas indicate the presence of lipids. The relative abundance maps in this case, showed the highest abundance of lipids (0.57 ± 0.09) along with some collagen (0.33 ± 0.09), but significantly lower amount of elastin (0.10 ± 0.05). Lastly, for the LCL plaque (Fig. 5.9 (c)), the fluorescence intensity had similar values in channels 1 and 2 as the HL plaque (due to the similar emission intensity profiles for elastin and lipids, see Fig. 5.10 (a)). However, unlike HL, the lifetime maps in the case of LCL plaque were similar in

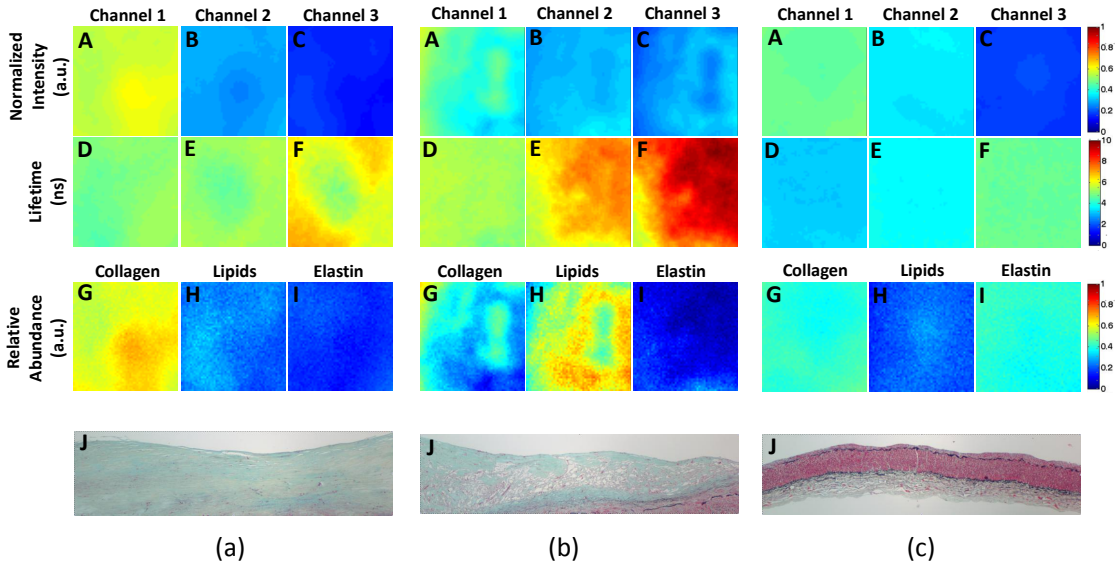

Figure 5.9: Standard FLIM features: normalized intensity and lifetime maps (A-C & D-F resp.) and NMF FLIM features: relative abundance maps (G-I) for three homogeneous samples, one from each (a) High Collagen, (b) High Lipids and (c) Low Collagen/Lipids class. Also shown are the representative histology sections for each class (J).

the three channels (between ∼3–4 ns). The relative abundance maps for LCL type of plaque suggested presence of collagen (0.41 ± 0.02) and elastin (0.40 ± 0.02) but a significantly lower amount of lipids (0.21 ± 0.03).

5.3.5 Classification Performance on Homogeneous Datasets

To compare the performance of the two sets of features (standard FLIM *vs.* NMF features) in terms of their ability to discriminate between the three plaque types (HC, HL, LCL), two multinomial logistic regression models, one from each feature set, were trained and tested on the homogeneous datasets. In the case of standard FLIM features, the decision boundaries are hypersurfaces in a five-dimensional fea-

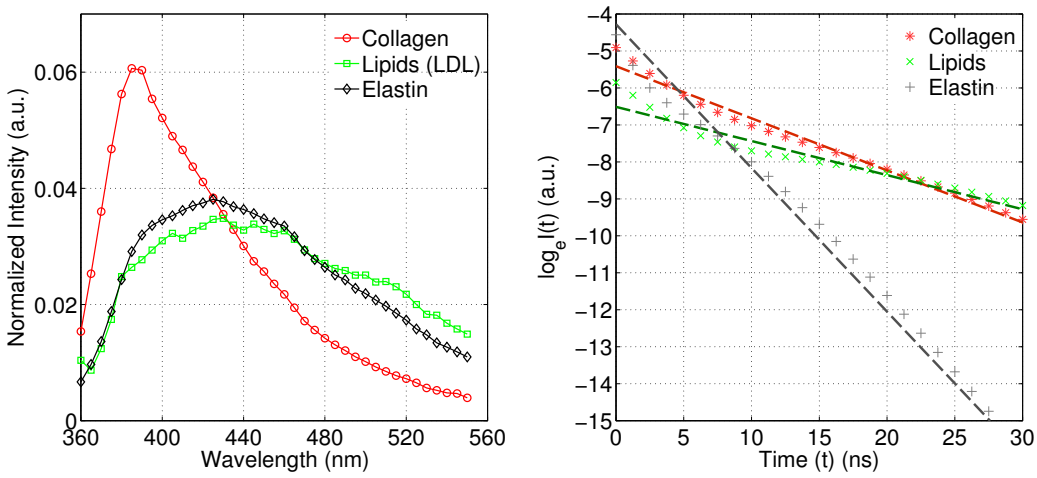

(a) (b)

Figure 5.10: (a) Steady state spectra for collagen, lipids (LDL) and elastin obtained from time-resolved measurements (b) log-transformed fluorescence decays for collagen, lipids and elastin fitted to straight lines. The negative inverse slope is equal to a fluorophore's average lifetime. Deviation from a straight line indicates the non-mono-exponential nature of the decay.

ture space and cannot be visualized. However, in the case of NMF features, the decision boundaries are lines in a 2-D feature space as shown in Fig. 5.11. As can be seen in Fig. 5.11, the classifier partitions the feature space into 3 regions corresponding to the three classes. In order to quantify the classification performance of the classifiers, we computed the confusion matrices *via* 10 fold stratified CV, which are shown in Fig. 5.12. The overall classification accuracy for the standard FLIM features and the NMF features was estimated to be 98.3% and 96.1%, respectively.

5.3.6 Validation on Heterogeneous Plaques

We also compared the performance of the two classifiers trained on the homogeneous datasets by testing them on datasets of plaques showing heterogeneous

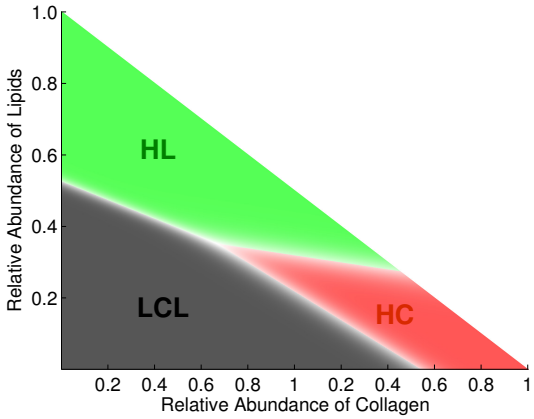

Figure 5.11: Feature space partition obtained by the multinomial logistic regression classifier. The multinomial logistic regression classifier for the NMF features partitions the feature space into three regions corresponding to the three classes: High Collagen (HC), High Lipids (HL) and Low Collagen/Lipids (LCL) seperated by linear decision boundaries (white region).

histopathology. Three examples of such validation are shown in Fig. 5.13 (a)-(c). The first two rows: (A)-(C) & (D)-(F) in each sub-figure show the normalized intensity and lifetime maps, respectively. The abundance maps for collagen, lipids and elastin are shown in the third row: (G)-(I). The classification maps for classifier trained on standard FLIM and NMF features are shown in panel (J) and (L), respectively. For both classification maps, the probability of each FLIM image pixel belonging to HC or HL class is color coded in red and green, respectively. We also display a matching histology section for each plaque in panel (K) of each sub-figure.

Fig. 5.13 (a) shows the feature and classification maps for a plaque with regions of LCL (top) and HC (bottom). The matching histology section for this sample confirmed that the LCL region was IT and the HC region was fibrotic PIT. A plaque showing regions of HC, HL and LCL is shown in Fig. 5.13 (b); a histology section

True Class \ Predicted Class	HC	HL	LCL
HC	13622	434	344
HL	507	13887	6
LCL	57	0	50343

True Class \ Predicted Class	HC	HL	LCL
HC	12963	510	927
HL	636	13600	164
LCL	763	54	49583

Figure 5.12: Confusion matrix for the standard FLIM features (left) and the NMF FLIM features (right). The diagonal entries indicate the number of pixels that were correctly classified, while the off-diagonal entries indicate the misclassified pixels.

corresponding to the middle of the plaque confirmed that the HC region was fibrotic PIT, the HL region showed foam cell infiltration, and the LCL region was IT. Finally, a plaque showing regions of HL (top-left) and LCL (bottom-right) is shown in Fig. 5.13 (c); a histology section corresponding to the middle of the plaque confirmed that the HL region was PIT highly infiltrated by foam cells, and the LCL region was IT.

5.4 Discussion

In this study, we presented an application of NMF to interpret multispectral FLIM data. We also demonstrated the potential application of the proposed method for multispectral FLIM based tissue characterization using the coronary atherosclerotic plaques as a test model. In the following, we discuss the main advantages and limitations of the proposed method over the standard methods of interpreting multispectral FLIM images.

The conventional method of interpreting multispectral FLIM images is based on

comparing the average spectral intensity and lifetime values of a sample with a set of possible known fluorophores. This method is very subjective in most cases, especially when there are more than one fluorescing species contributing to the bulk fluorescence signal. In contrast, the NMF features provide a more direct and intuitive way of interpreting FLIM images, because fluorophore abundance maps can be directly related to tissue biochemistry. The application of NMF to the multispectral FLIM data from human coronary plaques clearly demonstrated this aspect of the proposed method, where it was shown how the NMF approach was not just able to identify the main endogenous tissue fluorophores (i.e. elastin, collagen and lipids), but was also able to quantify their relative abundance maps, allowing for direct biochemical characterization of the atherosclerotic plaques.

To provide quantitative interpretation of FLIM images based on the intensity and lifetime values, the most commonly used method assumes that all the constituent fluorophores in a sample have mono-exponential decay kinetics. The sample fluorescence decay is then expressed as a multi-exponential model, in which each exponential component is associated to each constituent fluorophore. The sample fluorescence decay at each pixel is thus fitted to the multi-exponential model, and the estimated normalized pre-exponential weights are interpreted as the relative contribution of each constituent fluorophore to the bulk fluorescence signal [17, 49]. While such an interpretation of FLIM images can be more informative than the analysis based on single average lifetime value, it is restricted in a way, because many fluorophores are

known to exhibit non-monoexponential decays thereby violating the assumption of a mono-exponential decay associated to each constituent fluorophore. This is even more pertinent when analyzing endogenous multispectral FLIM data, because many endogenous fluorophores show non-monoexponential decay dynamics [22]. This however, is not a problem with the NMF approach, because it does not make any assumption about the functional form of the end-member profiles (i.e. decay dynamics of the constituent fluorophores). This is evident from the log-transformed fluorescence decay profiles for collagen, lipids and elastin retrieved *via* NMF and shown in Fig. 5.10 (b), where the deviation of these plots from straight lines (dashed lines) indicate the complex nature of the decay dynamics.

Kremers *et al.* recently proposed a method capable of handling fluorophores showing non-monoexponential decays; however, its application was limited to two species [49], like many other earlier studies [48, 51]. This is mainly because the SNR requirement for fitting a multiexponential model with more than two lifetimes is very demanding. Thus, these methods can handle experimental FLIM data where only two molecules can be simultaneously monitored. Moreover, in most of these studies only the fluorescence lifetime but not the spectral information is used in the unmixing process [49, 52]; e.g. in the method proposed by Kremers *et al.*, only one emission band was considered. Schlachter *et al.* recently proposed a method capable of handling multispectral FLIM data; however, its application was limited to mono-exponential fluorescence decays and to two species [52]. The NMF approach, on the

other hand, can handle multispectral FLIM data originating from more than two constituent fluorophores that is measured across an arbitrary number of emission spectral bands. This can facilitate the identification of the underlying constituent fluorophores, since the end-member profiles obtained *via* NMF contain both spectral and temporal information which makes it possible to identify them with adequate confidence. This was clearly demonstrated in our analysis of the multispectral FLIM data from the human atherosclerotic plaques, where the three fluorophores were correctly identified as elastin, collagen and lipids, as expected based on the well characterized histopathology of atherosclerosis [69]. In this case, the identification of the constituent fluorophores was performed based on both the spectral and lifetime values of the estimated end-member profiles at three different emission bands. This is in contrast to the standard FLIM analysis method, where only one lifetime value is available for making such an identification. In such a case, unless guided by strong evidence derived from tissue biochemistry, the identification of the latent fluorophores can at best be only hypothesized.

Another advantage of the NMF approach over the standard FLIM data analysis methods is that the NMF features (abundance maps) can be obtained directly from the spectro-temporal FLIM intensity data in a computationally efficient manner without the need for time deconvolution. The time complexity of SISAL algorithm is estimated to be of the order $O(NK)$ in [65], wherein the authors have also compared the time performance of SISAL against other NMF algorithms. Furthermore,

once the end-member profiles have been derived from a pre-recorded dataset, the abundance maps for a new sample can be obtained quickly by performing a simple inversion. This is unlike in the case of standard FLIM features, where unless extremely short excitation light pulses are used, time-deconvolution of the instrument response from the fluorescence decay data is required to obtain lifetime maps [22]. The deconvolution coupled with multi-exponential model fitting involve iterative optimization, which is both computationally expensive and time consuming. This advantage of the proposed method, however, necessitates that the data is recorded by the same system, i.e. the instrument response for all the data is the same.

The above stated advantages of the NMF method however, come with the need of having enough diversity in data such that the simplex formed by the data vectors is filled adequately to enable the inference of the underlying simplex structure. It is only in such a case, that NMF algorithms are able to estimate the end-member profiles and the corresponding relative abundances with confidence.

An important aspect of the proposed technique is the estimation of the number of components (end-members) present in the linear mixing model. Several methods for determining the number of end-member are reported in the literature, ranging from relatively simple techniques like principal component and independent component analysis to more complicated techniques like virtual dimensionality [70], maximum noise fraction [71] and noise adjusted principal components [72] and many more. While these techniques have been applied with varying degrees of success in different

applications, there is no single approach generally accepted to work in all cases. In our case, the choice of three end-members ($K = 3$) was primarily based on the biochemical understanding of the underlying tissue. However, in cases where there is no prior knowledge about the possible number of end-members, any or more than one of the above techniques can be used in conjugation with the interpretation of the end-member signatures obtained by NMF to decide on an appropriate number of end-members.

Finally, we also validated the performance of the new set of FLIM features in terms of their ability to discriminate between three types of atherosclerotic plaques. The classification maps and the confusion matrices presented in the results section, suggested that the NMF features are comparable to the standard FLIM features in terms of their discriminatory power to differentiate between the three plaque types. With the added advantage of ease of interpretation, we believe that the NMF features can facilitate the translation of multispectral FLIM from predominantly a lab imaging modality to clinical setting.

5.5 Conclusions

To summarize, we presented the application of NMF to multispectral FLIM data to derive a set of NMF features that provides an intuitive and an objective way of characterizing latent tissue fluorophores and their abundances. The method presented in this study made no assumption about the functional form of decay kinetics of the fluorophores under study and can be obtained directly from the recorded mul-

tispectral FLIM intensity data thereby obviating the need for deconvolution. As discussed earlier, several studies on the application of FLIM to tissue diagnosis use the difference in lifetime values to distinguish normal tissue from a pathological tissue; however, the scope of such studies has been severely restricted to those two ends of the disease-progression spectrum. We believe that this is mainly due to the absence of techniques that can objectively characterize the latent tissue fluorophores and quantify the changes in their abundance during the pathogenesis of a disease. The method proposed in this study is an attempt in this direction, which would expand the scope of FLIM in clinical graded diagnosis by providing an easy and objective way of interpreting multispectral FLIM data. More generally, the method detailed in this study can also be helpful in advancing the field of molecular imaging and may find broad applicability in basic, pre-clinical and clinical research.

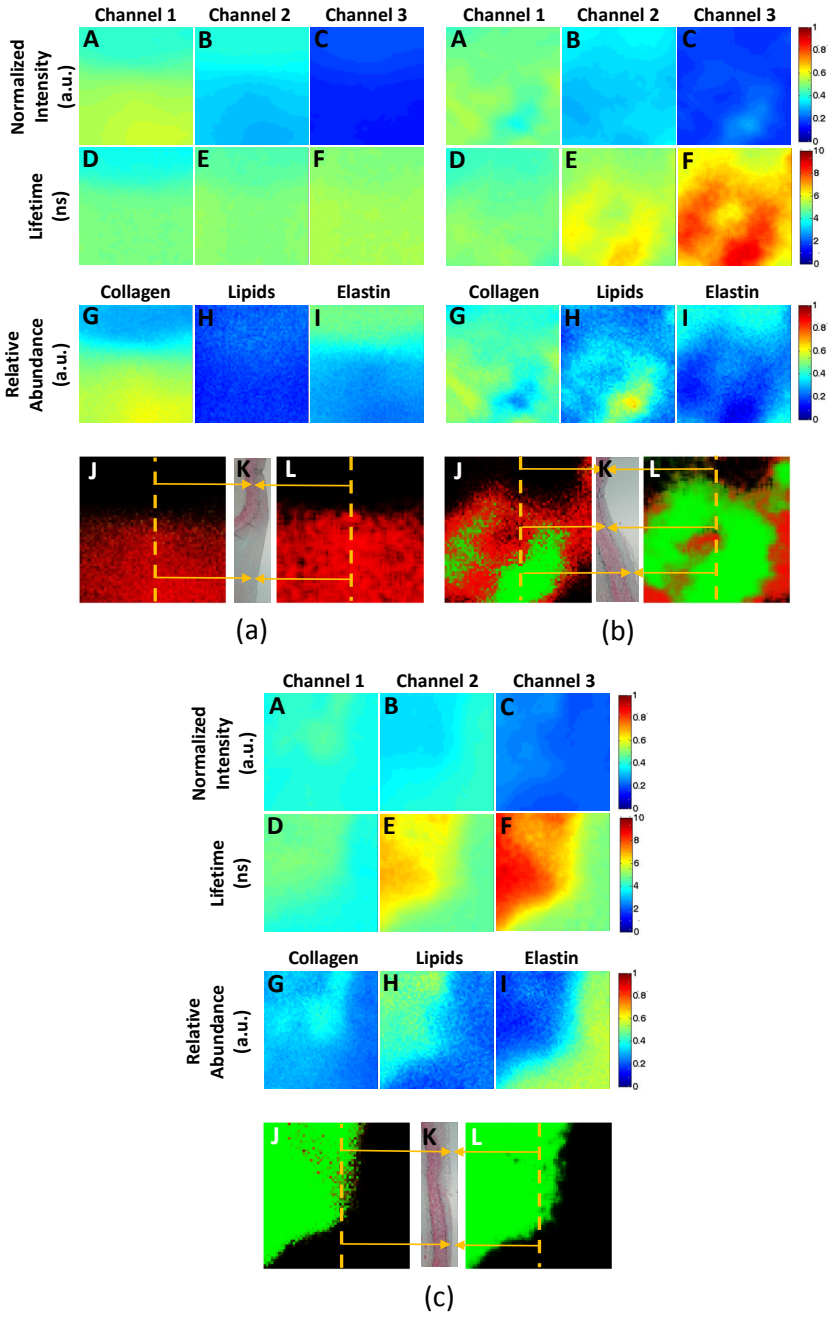

Figure 5.13: Results of the classification performance on the heterogeneous datasets. Standard FLIM features: normalized intensity and lifetime maps (A-C & D-F resp.) and NMF FLIM features: relative abundance maps (G-I) for three heterogeneous samples with regions of: (a) HC and LCL (b) HC, HL and LCL, and (c) HL and LCL. Also shown are the histology sections from the center of the sample (K) with matching regions in the classification maps obtained from the NMF features (J) and the standard FLIM features (L) shown in orange arrows. Pixels in the classification maps are color coded as red for HC, green for HL and black for LCL

6. COMBINED MORPHOLOGICAL AND BIOCHEMICAL IMAGING OF ATHEROSCLEROSIS

6.1 Introduction

Invasive imaging of coronary atherosclerotic plaque is limited to the evaluation of its morphological features, while not evaluating metabolic processes like inflammation, oxidative stress, and dyslipidemia, that lead to its development [73–77]. Early and intermediate-stage atherosclerotic plaques have thin fibrous caps, lipid-laden cores, and localized inflammation that are inadequately visualized by using OCT or intravascular ultrasound (IVUS) [78]. Convincing evidence exists to indicate that the underlying mechanisms in coronary plaque development, leading to acute thrombosis are multifactorial, involve complex interactions between structural, compositional, biomechanical, cellular, and molecular processes in the vessel wall [79, 80]. Unfortunately, there is no current imaging modality (noninvasive or intravascular) that can provide such a level of plaque characterization.

Of the commercially available intravascular imaging tools, OCT provides the highest resolution images and can be used to define the superficial morphological features of atherosclerotic plaques; however, it does not offer any information about the biochemical make-up of plaques [81–83]. Conversely, endogenous fluorescence imaging techniques like FLIM enables the quantification of plaques' biochemical content and the identification of lipid-rich and collagen-rich plaques [69], but does not

provide any information about their morphology. In this study, we report how quantitative biochemical classification based on standard multispectral FLIM features (two-dimensional normalized intensity and lifetime maps for each spectral channel described in Chapter 2.3) can be combined with qualitative morphological OCT image analysis for a more comprehensive evaluation of atherosclerotic plaques.

The coronary artery tissue database described in Section 3.2.1 was used in this study. The data was acquired using the multimodal FLIM-OCT imaging system described in Section 3.1.

6.2 Methods

6.2.1 Histology

On the basis of the histopathologic evaluation, each section was classified as either intimal thickening (IT), pathologic intimal thickening (PIT), collagen-rich PIT having >50% of collagen content (CLG-PIT), PIT with superficial lipid accumulation (LIP-PIT), fibroatheroma (FA) with a cap having >50% of collagen content (CLG-FA), FA with a lipid-rich cap (LIP-FA), thin-cap fibroatheroma (TCFA), calcified FA (CA), or CA with a collagen-rich cap (CLG-CA). In addition, the collagen-rich plaques (CLG-PIT, CLG-FA, CLG-CA) were grouped in a highcollagen (HC) category, the lipid-rich plaques (LIP-PIT, LIP-FA, TCFA) were grouped in a high-lipid (HL) category, and the other plaques (IT, PIT, CA) were grouped in a lowcollagen/lipid (LCL) category.

6.2.2 FLIM Plaque Evaluation

Similar to the analysis presented in Section 5, the endogenous FLIM signal was analyzed to classify the tissue based on its biochemical composition as (High Collagen) HC, (High Lipids) HL or (Low Collagen/Lipids) LCL plaques. The plaque autofluorescence was quantified in terms of the relative fluorescence intensity and the average lifetime at each pixel of the multispectral FLIM image. For statistical classification, Fisher's linear discriminant analysis [67] was applied with the six multispectral FLIM parameters as the feature vector for each pixel. A biochemical map was then generated after classifying each pixel of an image to 1 of the 3 groups (HC, HL, or LCL). Finally, each complete plaque segment was classified based on its estimated biochemical map as follows: if 10% or more of the pixels were classified as HL, the segment was classified as HL; if less than 10% of the pixels were classified as HL but at least 20% of the pixels were classified as HC, the segment was classified as HC; if less than 10% of the pixels were classified as HL and less than 20% of the pixels were classified as HC, the segment was classified as LCL.

6.2.3 OCT Plaque Evaluation

The OCT B-scans (cross-sectional images) were reviewed by an interventional cardiologist with clinical experience in the use of intravascular imaging. Following standard criteria for intravascular OCT reading [83], each plaque was classified as IT (showing two or three well-defined layers), PIT (showing a homogeneous signal-

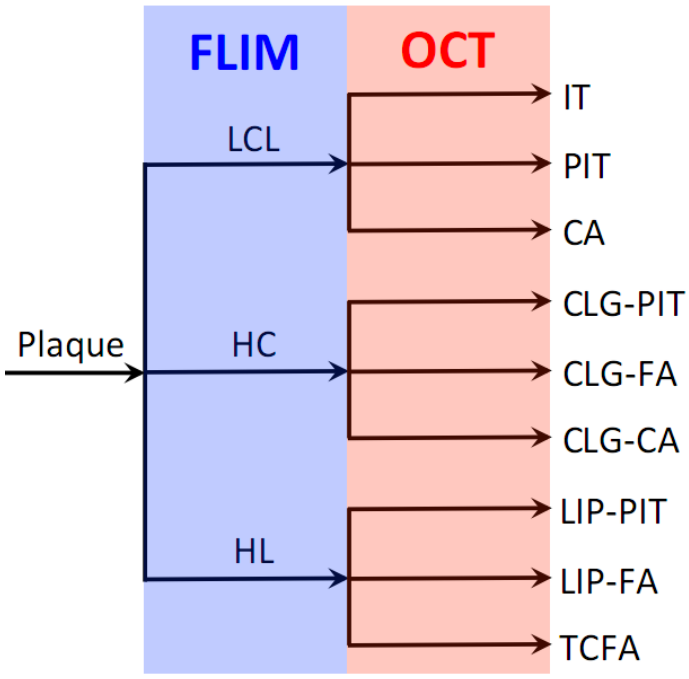

Figure 6.1: Histopathologic classification criteria of the multimodal OCT-FLIM cross sections. Based on standard OCT cross-section evaluation, each plaque was classified as: intimal thickening (IT), pathologic IT (PIT), fibroatheroma (FA), thin-cap FA (TCFA) or calcified FA (CA-FA). Based on the FLIM biochemical plaque characterization as high lipid (HL), high collagen (HC), or low collagen/lipid (LCL): each plaque was further classified as IT, PIT, fibrotic PIT (FIB-PIT), foam-cell infiltrated PIT (FC-PIT), fibrotic FA (FIB-FA), foam-cell infiltrated FA (FC-FA), TCFA or CA-FA.

rich region), FA (showing a signal-poor region with diffuse borders corresponding to a necrotic-core or a lipid-pool), or CA (showing a signal-poor region with sharp borders). An FA was considered TCFA if the cap thickness was $<100\,\mu$m.

6.2.4 Plaque Classification Based on FLIM and OCT Evaluation

To perform plaque evaluation based on FLIM and OCT, the FLIM-derived biochemical map were superimposed on the surface of the OCT volumetric image as

shown in Fig. 6.2 for a representative sample. The resulting multimodal plaque representations were evaluated, and each plaque was placed into 1 of the 9 classes following the criteria as defined in Fig. 6.1. Plaques classified as LCL by FLIM were further classified as IT, PIT or CA based on their OCT evaluation. Plaques classified as HC by FLIM were further classified as CLG-PIT, CLG-FA or CLG-CA based on their OCT evaluation. Plaques classified as HL by FLIM were further classified as LIP-PIT, LIP-FA or TCFA based on their OCT evaluation. The classification results were compared with the histopathology evaluation and the overall classification accuracy was computed.

6.3 Results

6.3.1 Histology

The histopathology evaluation of the 46 imaged coronary sections resulted in the following plaque distribution: IT (n=11), PIT (n=2) and CA (n=4) also grouped as LCL plaques (n=17); CLG-PIT (n=7), CLG-FA (n=3) and CLG-CA (n=4) also grouped as HC plaques (n=14); LIP-PIT (n=11), LIP-FA (n=2) and TCFA (n=2) also grouped as HL plaques (n=15). Representative histology sections for each plaque type are shown in Fig. 6.3.

6.3.2 FLIM Based Plaque Evaluation

The FLIM derived biochemical maps of all the IT, PIT and CA segments showed less than 5% of HC or HL pixels; thus, they all (17 out of 17) were correctly classified

as LCL plaques. The FLIM derived biochemical maps of all the CLG-PIT, CLG-FA and CLG-CA segments showed less than 5% of HL pixels but more than 20% of HC pixels; thus, they all (14 out of 14) were correctly classified as HC plaques. Finally, the FLIM derived biochemical maps of all the LIP-PIT, LIP-FA and TCFA segments showed more than 20% of HL pixels; thus, they all (15 out of 15) were correctly classified as HL plaques.

6.3.3 Plaque Classification Based on FLIM and OCT

It should be noted that while OCT can image up to $\sim$1 mm deep into the tissue, the biochemical assessment offered by FLIM is limited to the most superficial $\sim$200 μm. The biochemical map was color-coded as LCL (light blue), HC (yellow), or HL (red). Rendering the data as 2-D cross-sectional images (Fig.6.3, first, third and fifth rows) is convenient for direct comparison with the histopathology slides (Fig.6.3, second, fourth and sixth rows). This set of paired multimodal and histopathologic images accurately illustrates the evaluation criteria used for classification. Sample multimodal and histopathologic images of IT, PIT and CA are shown in the top six panels (Fig. 6.3, light blue box). They all showed a FLIM biochemical map corresponding to LCL content, reflecting the lack of superficial lipids and collagen as confirmed by histopathology. In addition, the OCT scans showed well-defined layers for the IT, a bright homogeneous single layer for the PIT, and a low-intensity region with well-defined borders corresponding to a calcified necrotic-core (NC) for the CA. All these morphological features were confirmed by histopathology.

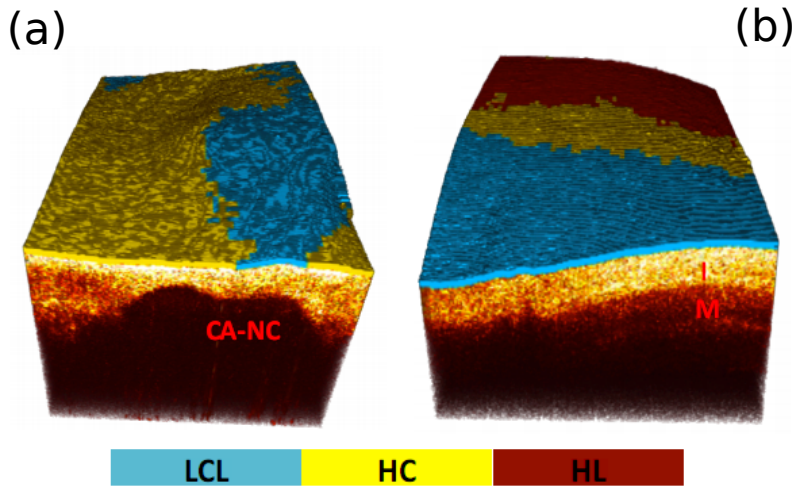

Figure 6.2: Multimodal OCT-FLIM volumes of representative coronary plaques. Sample volumetric OCT images with the FLIM derived biochemical maps projected on the lumen surface. (a) CA: the calcified necrotic core (CA-NC) is seen clearly on the OCT cross sections; the biochemical FLIM map shows that the left shoulder and part of the fibrous cap are high-collagen (HC), while the left shoulder is mostly low collagen/lipid (LCL). (b) IT to PIT transition: the initial OCT cross sections clearly indicate the intimal (I) and medial (M) layers on the IT region, with the FLIM map showing LCL content; as the plaque transitions from IT to PIT, the OCT shows a thickening of the intima, while the FLIM map indicates a transition from HC to high-lipid (HL).

Sample multimodal and histopathologic images of CLG-FA, CLG-PIT and CLG-CA are shown in the middle six panels (Fig. 6.3, yellow box). They all showed a FLIM biochemical map corresponding to HC content, reflecting dominant superficial collagen content as confirmed by histopathology. The OCT scan of the CLG-FA showed a low-intensity region with diffuse borders covered by a thick bright layer ($>100\,\mu$m), corresponding to a NC covered by a thick cap. The other OCT scans showed a bright homogeneous single layer for the CLG-PIT, and a low-intensity region with well-defined borders for the CLG-CA. All these morphological features

were also confirmed by histopathology.

Sample multimodal and histopathologic images of LIP-FA, LIP-PIT and TCFA are shown in the bottom six panels (Fig. 6.3, red box). They all showed a FLIM biochemical map corresponding to HL content, reflecting dominant superficial lipid content as confirmed by histopathology. The OCT scan of the LIP-FA showed a low-intensity region with diffuse borders covered by a thick bright layer ($>100\,\mu$m), corresponding to a NC covered by a thick cap. The OCT scan of the TCFA also showed a low-intensity region with diffuse borders but in this case covered by a thin bright layer ($\sim 100\,\mu$m), corresponding to a NC covered by a thin cap. The OCT scan of the CLG-PIT showed a bright homogeneous single layer. All these morphological features were also confirmed by histopathology.

Multimodal images from each of the 46 imaged coronary segments were evaluated using the classification criteria described above (Fig.6.1). These results are summarized in Table 6.1. All the LCL plaques correctly classified by FLIM were further correctly identified as IT, PIT or CA based on their OCT evaluation. From all the 14 HC plaques correctly identified by FLIM, 12 were further correctly identified as CLG-PIT, CLG-FA or CLG-CA based on their OCT evaluation; however, one CLG-PIT was misclassified as CLG-FA, and one CLG-FA was misclassified as CLG-PIT. From all the 15 HL plaques correctly identified by FLIM, 14 were further correctly identified as LIP-PIT, LIP-FA or TCFA based on their OCT evaluation; however, one LIP-PIT was misclassified as LIP-FA. Overall, 93.5% of the plaques (43/46) were

Table 6.1: FLIM-OCT classification results

FLIM Classification			OCT Classification		
			IT	PIT	CA
LCL 17/17	IT	(n = 11)	11		
	PIT	(n = 2)		2	
	CA	(n = 4)			4
			CLG-PIT	CLG-FA	CLG-CA
HC 14/14	CLG-PIT	(n = 7)	6	1	
	CLG-FA	(n = 3)	1	2	
	CLG-CA	(n = 4)			4
			LIP-PIT	LIP-FA	TCFA
HL 15/15	LIP-PIT	(n = 11)	10	1	
	LIP-FA	(n = 2)		2	
	TCFA	(n = 2)			2

correctly identified using the combined OCT-FLIM evaluation.

6.4 Discussion

The results of this study suggest that simultaneous coregistered OCT and FLIM imaging of coronary plaques enables the detailed characterization of the plaques morphologic and lipid/collagen content, which can be used to assign each plaque to its histopathologic class. Specifically, OCT is well suited to identifying layers, fibrous cap thickness, necrotic cores, and calcification, while endogenous FLIM allows identifying collagen- and lipid-rich plaques. Together, they enable the generation of detailed maps of plaque morphology and biochemistry, which can then be used to place the plaques in their respective histopathologic classes and to quantify the heterogeneity within the classes.

Recently, a consensus has been reached on standard criteria to identify fibrous plaques, calcification, and necrotic/lipid pools in intravascular OCT cross-sectional images (B-scans) [84]. In the present study, we have successfully applied these criteria to correctly identify all of the IT, CA, and TCFA plaques. However, the discrimination between pathological intimal thickening and fibroatheroma was less effective, highlighting the difficulty in identifying necrotic-cores or lipid-pools by OCT evaluation, particularly when they are not superficial. This limitation has also been noted by others [85]. In the present study, this is further confounded by the fact that our OCT system is based at a center wavelength of 830 nm rather than the more typical center wavelength of 1300 nm; hence, we expect poorer depth penetration for our system.

The characterization of the lipid and collagen content of plaque is important for histopathologic classification and for estimating a plaques propensity for developing into high-risk vulnerable plaque. In the present study, endogenous FLIM alone was able to identify low-collagen/low-lipid plaques (including IT, PIT, and CA), high-collagen plaques (including CLG-PIT, CLG-FA and CLG-CA), and high-lipid plaques (including LIP-PIT, LIP-FA, and TCFA) with 100% sensitivity and 100% specificity.

Although FLIM enables biochemical characterization of coronary plaques, little information about plaque morphology can be inferred from the autofluorescence signal. For instance, LIP-PIT, LIP-FA and TCFA were all classified as HL based on

FLIM regardless of their very different morphological characteristics. In contrast, OCT enables morphologic characterization of coronary plaques but does not provide specific information about plaque biochemistry. For instance, PIT, GLG-PIT and LIP-PIT all appeared as bright and homogeneous single layers in their OCT scans regardless of their different biochemical composition. Only when the FLIM plaque classification was merged with the OCT B-scans (Fig.6.2 and 6.3) it was possible to characterize plaque composition and morphology simultaneously. In particular, the fibrous plaques correctly identified by OCT were further characterized as having significant collagen or lipid content based on the FLIM classification (Fig. 6.3; PIT, CLG-PIT, and LIP-PIT panels). Likewise, the fibroatheromas correctly identified by OCT were further identified as having a fibrous cap and shoulders rich in collagen or lipids (Fig. 6.3; CLG-FA and LIP-FA panels). Our results demonstrate that simultaneous OCT and endogenous FLIM imaging of coronary plaque enables the identification of all histopathologic types with high accuracy (>90%).

6.5 Conclusion

In conclusion, we have demonstrated the feasibility of simultaneous FLIM-based biochemical and OCT-based morphologic characterization of coronary plaque at practical spatial resolution and acquisition speeds, and the identification of all histopathologic types of coronary atherosclerotic plaque using the proposed multimodal optical imaging technology.

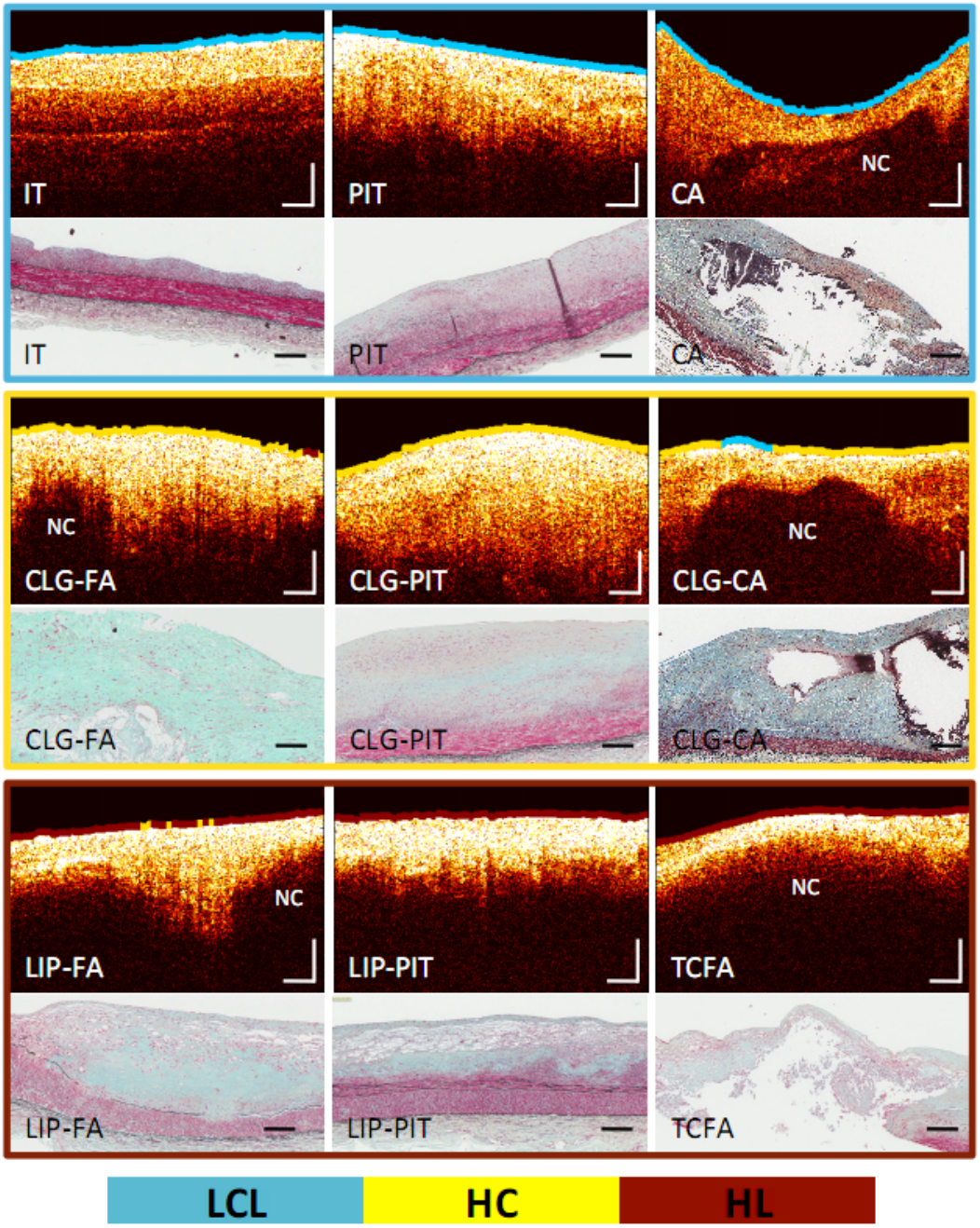

Figure 6.3: Multimodal OCT-FLIM Cross Sections of Representative Coronary Plaques. Rows 1 and 3: 2D multimodal images (cross sections) of representative plaques from each histopathologic class. Rows 2 and 4: Corresponding histology slides. Collagen appears blue, elastin is the black/dark lines, smooth muscle cells appear as elongated red cells, lipids appear as empty space, and foam cells appear with large white cytoplasm. All scale bars are 200 μm.

7. COMBINED MORPHOLOGICAL AND BIOCHEMICAL IMAGING OF ORAL CANCER

7.1 Introduction

Despite the ease of accessibility of the oral cavity and identifiable risk factors, the overall five year survival rate for oral cancer has not improved significantly over the past several decades [14], mostly due to diagnosis at later stages. Late diagnosis of oral cancer can be mainly attributed to the current method of detection and diagnosis of oral malignancies, which relies on visual inspection followed by biopsy of suspicious lesions. Biopsy being an invasive procedure is reserved for highly suspicious lesions, which often leads to missing potentially malignant lesions. This is because many malignant lesions on visual examination resemble benign lesions found in commonly occurring less serious conditions of the oral cavity. Even in cases where suspicious lesions are well identified, due to the complex nature of oral lesions, the choice of the optimal site for biopsy remains an important concern. Additionally, high rates of inter and intra-observer variability in histopathological evaluation of oral biopsies further confound the diagnosis of oral cancer. To enable early detection of oral cancer, there is, therefore, a need for a diagnostic tool that is noninvasive, reliable and capable of being used in an out-patient setting. Such a tool should enable screening for possible malignancy of large number of oral lesions, which are routinely encountered by dentists and other physicians during visual examination of the oral

cavity.

Progression of oral cancer is accompanied by alterations in the intrinsic fluorescence properties of the oral tissue as a consequence of changes in the relative abundance of tissue autofluorophores like collagen, NADH and FAD [17, 39, 86]. These changes result from processes like increased cellular invasion and NADH-FAD activity in the epithelial layer and degradation of stromal collagen, which are linked to oral dysplasia. The ability of fluorescence imaging modalities to probe these biochemical changes makes these them suitable for the diagnosis of oral cancer. As discussed in Section 2.2, depending on the source of contrast, fluorescence imaging can be classified into two categories, namely, steady-state and time-resolved. There are two main advantages of time-resolved measurements over steady-state measurements. First, using fluorescence lifetime information from time-resolved measurements, it is possible to distinguish between multiple fluorophores that have overlapping emission spectra and are thus indistinguishable using only intensity information available from steady-state measurements. Second, unlike steady-state measurements, lifetime measurements are more robust to variations in the intensity of excitation light and fluorophores' concentrations. Despite the aforementioned advantages of using lifetime information, most studies on the applications of fluorescence imaging for oral cancer diagnosis are based on steady-state measurements. Lack of studies on the diagnostic potential of lifetime based imaging methods can be partly explained by the fact that unlike steady-state fluorescence measurements, which require simple

instrumentation and minimal computation, instrumentation and signal processing for lifetime based systems are more complex. Motivated by these observations, the first part of the present study seeks to: (a) assess whether using lifetime information, in addition to the fluorescence intensity information, offers any improvement in the diagnostic potential of fluorescence based imaging for oral cancer, and (b) examine the necessity of performing deconvolution (computational bottleneck in FLIM signal processing) for obtaining lifetime by evaluating the performance of an approximate method of lifetime estimation that does not require deconvolution.

In addition to changes in the relative abundances of tissue autofluorophores, progression of oral cancer is also associated with several structural modifications of the oral epithelium, like epithelial thickening, loss of the layered structure, and irregular epithelial stratification [18, 20, 21]. OCT is an interferometry based structural imaging modality that is capable of providing images of sub-surface tissue structures in a non-invasive way. The high-resolution imaging capability of OCT makes it an attractive imaging modality for the diagnosis of oral cancer. Several studies on the application of OCT for the diagnosis of oral cancer are discussed in the literature [20, 21]. However, most of these studies are based on visual inspection of OCT B-scans to identify structural features associated with the malignant transformation of the oral tissue. Visual assessment of tissue morphology, as reported in these studies, has a limited scope for two main reasons. First, it is extremely time-consuming and practically impossible to visually evaluate the large amount of data obtained

from a high-speed OCT system. Second, certain properties of tissue texture, like graininess and homogeneity are difficult to quantify by direct visualization. Therefore, it is highly desirable to develop automated image processing methods that can quantitatively characterize tissue morphology and texture in OCT images. Motivated by these observations, the second part of the present study investigates the feasibility of using automated algorithms for quantifying structural features in OCT images that are associated with the malignant transformation of the oral epithelium.

Finally, the overarching objective of this study was to examine the premise that using both biochemical and morphological information obtained from FLIM and OCT, respectively, will increase the diagnostic accuracy for oral cancer, compared to using only one type of information. The analysis presented in this study was performed on FLIM and OCT images from the Hamster Cheek Pouch Tissue Database described in Section 3.2.2. To evaluate the diagnostic accuracy, a quantitative approach was taken in which several metrics (or *features*) describing various attributes of FLIM and OCT images were first obtained by using signal and image processing techniques. These features were subsequently used to design a statistical learning model to perform automated classification. The performance of the different sets of features was compared based on several measures of classification performance like accuracy, sensitivity and specificity.

7.2 Methods

7.2.1 Histopathological Evaluation

As stated earlier, the hamster cheek pouch database described in Section 3.2.2 was used in this study. Biopsy samples from the imaged areas were processed following standard procedures for histopathology analysis. On an average, 10 sections per tissue sample were obtained and each section was assessed by a board certified pathologist to be one of the following five grades: (i) normal (G0), (ii) hyperplasia and hyperkeratosis (G1), (iii) hyperplasia with dysplasia (G2), (iv) carcinoma *in situ* (G3), and (v) squamous cell carcinoma (G4). For classification analysis, the following criteria was used to group the tissue samples into three classes: (i) class 1 (*benign*; 27 samples): samples from the control group (15 samples) and samples for which all histology sections were graded as G1 (12 samples), (ii) class 2 (*pre-cancerous*; 11 samples): samples for which at least 50% sections were graded as G2 or G3 and none of the sections were graded as G4, and (iii) class 3 (*cancerous*; 15 samples): samples for which all sections were graded as G4. Samples that could not be assigned to any of the above mentioned classes were excluded from the analysis.

7.2.2 FLIM Features

For a systematic analysis of FLIM features, we grouped the FLIM features into two groups, namely, the *exact* FLIM features and the *approximate* FLIM features, each containing nine features. The normalized intensities and average lifetimes maps

for the three emission bands, which are obtained by following the standard multispectral FLIM data processing outlined in Section 2.3 constituted six of the nine exact FLIM features. As described in Section 2.3, the average lifetimes (denoted by τ_{avg}), were computed based on the mathematical definition of lifetime stated in Eq. (2.4). Another way of quantifying the rate of fluorescence decay is to assume that the fluorophore follows a first order decay dynamics, in which case, lifetime can be estimated as the time at which the fluorescence intensity is reduced to $1/e$ of its maximum value. The lifetime estimated in this way shall be referred to as the $1/e$ *lifetime* (denoted by $\tau_{1/e}$). The average lifetime is different from $1/e$ lifetime in that it takes into account the entire fluorescence decay to estimate the lifetime, unlike $1/e$ lifetime, which is based on only the initial part of the fluorescence decay. Also, for a fluorophore that follows a first order decay kinetics, the two lifetimes, τ_{avg} and $\tau_{1/e}$, are equal. The addition of three $1/e$ lifetimes (one for each emission channel) to the set of six multispectral FLIM features resulted in a total of nine exact FLIM features.

The second group of features, called the approximate FLIM features also comprised normalized intensities, average and $1/e$ lifetimes. However, unlike the exact lifetime features, which are obtained from the deconvolved decay profiles, the approximate lifetime features were estimated directly from the undeconvolved recorded decay profiles by using the falling part of the recorded decay as a surrogate for the deconvolved decay profile, and subsequently estimating the lifetimes (both average

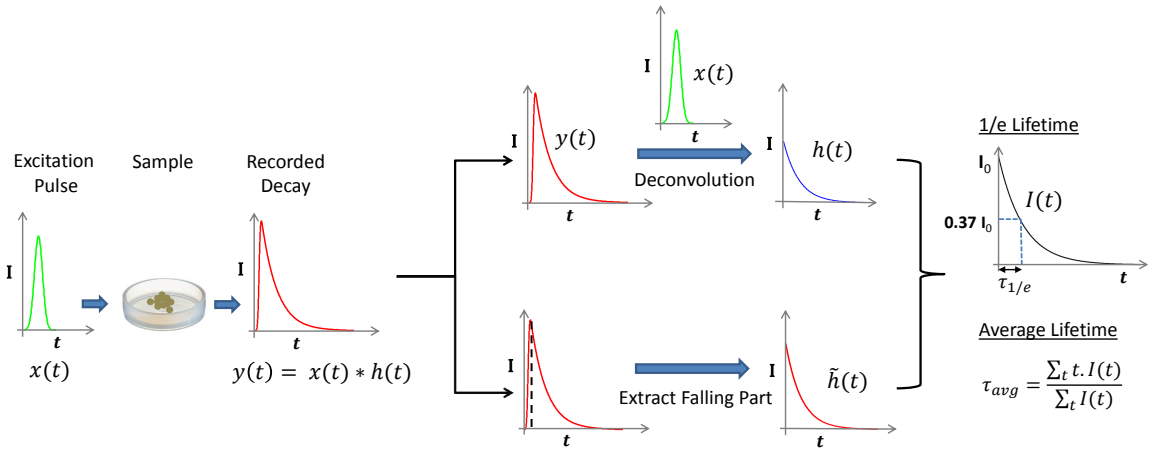

Figure 7.1: Schematic illustrating the process of obtaining exact and approximate lifetime features. The exact lifetimes are obtained from the deconvolved intrinsic decay $h(t)$ shown in blue, whereas the approximate lifetimes ate obtained from the falling part of the recorded decay $y(t)$, denoted by $\tilde{h}(t)$, which is used as a substitute for the the intrinsic decay.

and $1/e$) in a manner similar to the exact lifetimes. The process of obtaining the exact and approximate lifetimes is illustrated in Fig. 7.1.

As noted in Section 3.1.3, the 2-D FLIM feature maps contain 60×60 pixels over a FOV of $2{\times}2\,\text{mm}^2$. For the analyses presented here, these feature maps were spatially averaged (window size: $3{\times}3$ pixels) to produce FLIM feature maps of size $20{\times}20$ pixels. In the following discussion, unless stated otherwise, "FLIM features" shall be assumed to refer to the "exact FLIM features".

7.2.3 OCT Features

Different layers of normal oral tissue appear as bright and dark bands in an OCT B-scan. Stratum corneum, the topmost kertainized layer of the oral tissue can be seen as a bright layer at the air-tissue interface in the B-scan of a normal tissue shown

in Fig. 7.3 (a). Just below this layer, a dark band corresponding to the stratified squamous epithelium (EP) can be seen. The epithelium layer is followed by lamina propria (LP), top portion of which appears as a bright band. In contrast, B-scan of a malignant oral tissue shows the absence of the layered structure, as can be seen in Fig. 7.3 (b), where the B-scan has brightest intensity at the surface that gradually fades off with depth. This layered versus non-layered structure is also evident by examining the A-lines in a B-scan. In the case of a layered tissue, an A-line has multiple prominent peaks corresponding to the different layers, whereas for a non-layered tissue, there is only one prominent peak corresponding to the tissue surface as shown in Fig. 7.2. To quantify these characteristics of A-lines, we defined two types of A-line features, which shall be referred to as the "peaks and valleys" and "crossings" features.

To calculate these features, the tissue surface was first identified by performing a simple foreground/background segmentation using k-means algorithm ($k = 2$). The B-scans were then aligned with respect to the tissue surface and were subsequently filtered by a three-step process. First, to reinforce the layered structure in B-scans, the aligned B-scans were filtered in the lateral direction by using a moving average kernel of size 60 A-lines. Next, the A-lines were smoothened, in the axial direction, by performing morphological *closing* (to flatten valleys) followed by *opening* (to eliminate narrow peaks) by flat structuring elements of size 10 and 5 pixels, respectively. Finally, any spurious peaks having a normalized magnitude lower than

0.1 were suppressed by performing h-maxima transformation of the A-lines. Details about opening and closing operations, and h-maxima transform can be found in any standard textbook on morphological image processing, e.g. [87]. To calculate the peaks and valleys features, local maxima (peaks) and minima (valleys) of the filtered A-lines were detected and the following four peaks and valleys features were computed: (i) Σp_i, (ii) $\Sigma p_i - \Sigma v_i$, (iii) $\Sigma p_i + \Sigma v_i$, and (iv) $\Sigma(p_i - (v_i + v_{i+1})/2)$, where p_i and v_i denote the normalized intensity values of the $ith.$ peak and valley, respectively. To calculate the crossings features, a crossings vector of size 15×1 was defined for each A-line, such that the jth element of the crossings vector is equal to the number of times the filtered A-line would intersect an imaginary line drawn parallel to the x-axis (depth) and having a y coordinate (normalized intensity value) of $(20 - j)/20$ (shown as red broken lines in Fig. 7.2). Intuitively, if an A-line has just one prominent peak, then all the elements of the crossings vector would be two, whereas, for an A-line that has multiple prominent peaks, several elements of the crossings vector would be greater than two, as illustrated in Fig. 7.2. Four crossings features defined as the (a) mean, (b) median, (c) mode, and (d) standard deviation of the elements of the crossings vector were computed. Overall, eight (four peaks and valleys, and four crossings features) A-line derived features were obtained for each A-line, resulting in eight 2-D feature maps of size 600×600 pixels for each sample. Speckle pattern in an OCT image of a tissue sample is known to contain information about the size and distribution of the sub-resolution tissue scatterers [88, 89]. Oral

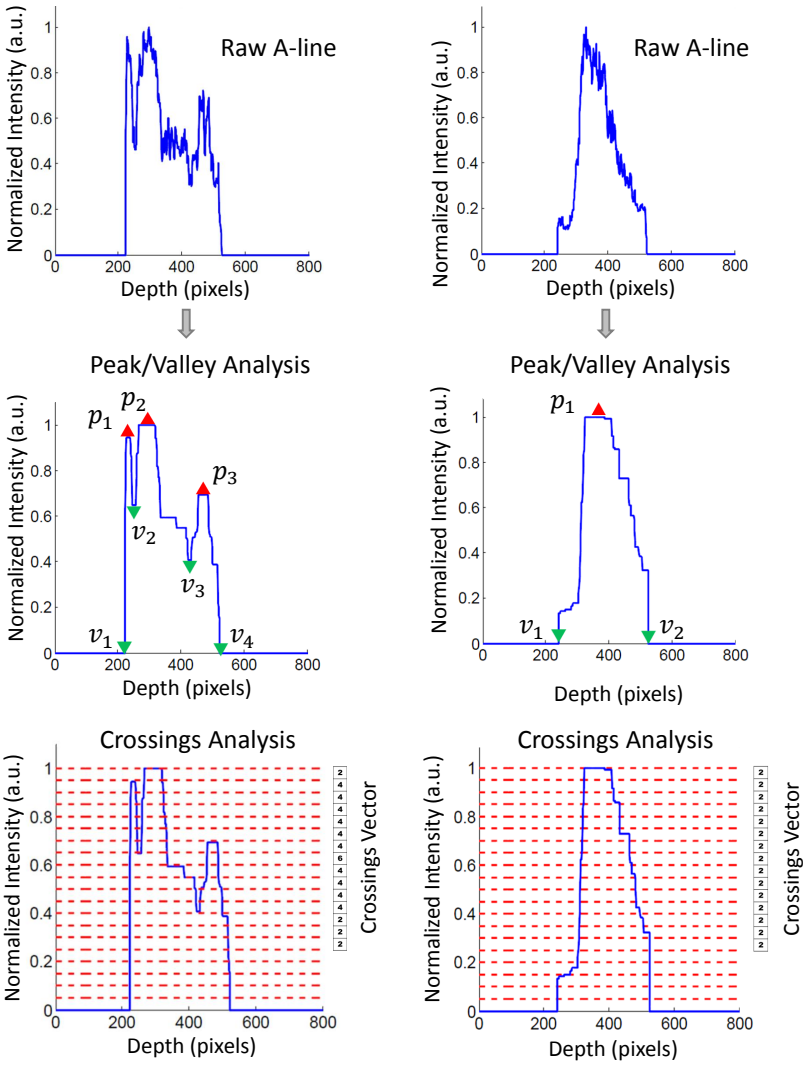

Figure 7.2: Schematic illustrating the process of obtaining peaks & valleys and crossings features from representative A-lines of a normal tissue (left column) and a malignant tissue (right column). Raw A-lines were first filtered to remove noise. Four peaks & valleys features were computed as: (i) Σp_i, (ii) $\Sigma p_i - \Sigma v_i$, (iii) $\Sigma p_i + \Sigma v_i$, and (iv) $\Sigma(p_i - (v_i + v_{i+1})/2)$, where p_i and v_i denote the normalized intensity values of the peaks and valleys respectively. To compute the crossings features for an A-line, the intensity axis was partitioned into 20 equal intervals (shown as red broken partition lines). A 15×1 crossings vector was defined such that the $jth.$ element is equal to the number of times the filtered A-line intersects the $jth.$ partition line. The mean, median, mode, and standard deviation of the elements of the crossings vector comprised the crossings features.

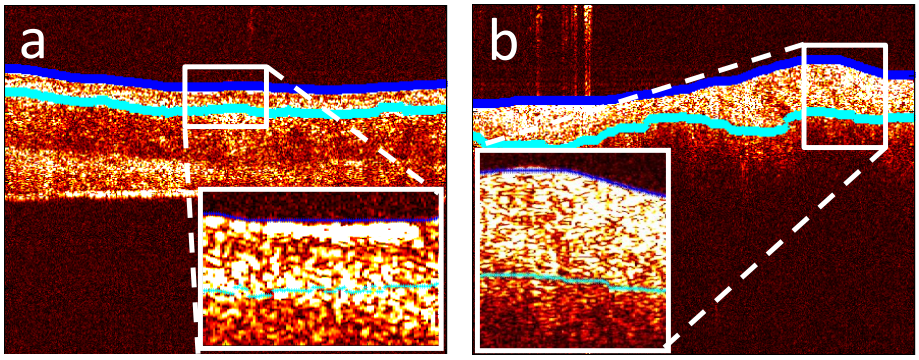

Figure 7.3: Textural differences between B-scans of a normal and a malignant tissue ((a) & (b) respectively). The top surface and the epithelium boundary are shown in blue and cyan respectively. Magnified views of portions of the delineated epithelial regions (insets) show continuous dark and bright bands in the case of a normal tissue and an interspersed speckled region for the malignant tissue.

dysplasia is often characterized by basal cell hyperplasia and epithelial proliferation. The presence of dysplastic cells in the epithelium results in an interspersed speckle pattern in an OCT B-scan, which is unlike the speckle pattern seen in B-scans of normal oral tissue, where different layers appear as more homogeneous bright and dark regions (see insets in Fig. 7.3 (b)). To quantify this difference in speckle patterns, several B-scan derived texture features were computed. The first step in computing these features was to locate the boundary between the EP and LP. In the case of a layered tissue, this was achieved by identifying the second prominent peak along A-lines in an OCT B-scan, as shown in cyan in Fig. 7.3 (a). For cases where the layered structure was absent, the B-scan was segmented into three regions using k-means clustering algorithm, and the lower boundary of the topmost tissue region was used as a proxy for the EP/LP boundary as shown in cyan in Fig. 7.3 (b). After

delineating the EP/LP boundary, the region between the tissue surface (shown in blue in Fig. 7.3) and the EP/LP boundary was selected for texture analysis based on gray level run length (GLRL) analysis. A "gray level run" is a sequence of consecutive pixels, along some direction, having the same gray level value. The length of a gray level run is the number of pixels in that run. To quantify texture based on GLRL, a 2-D GLRL matrix for a given direction is computed. The element (i, j) of the GLRL matrix denotes the number of times a run of length j and pixel value i is found in the image. The process of obtaining a GLRL matrix for a 4×4 image is illustrated in Fig. 7.4. To obtain texture features from a GLRL matrix, 11 different measures characterizing different textural properties, like coarseness, non-uniformity, etc. were computed (Fig. 7.4; also see [90]). To take care of the possible slanted tissue orientation, the B-scans were aligned with respect to the air/tissue interface before computing the texture features. The GLRL features were computed for both vertical and horizontal directions, and for two quantization levels, namely, binary and 32 bits, yielding 44 B-scan derived texture features. The GLRL texture features for each B-scan were computed over a sliding window region of size 60 A-lines within the delineated epithelial region, resulting in B-scan derived texture feature maps of size 600×600 pixels. Both the A-line and B-scan derived OCT features were spatially averaged (window size: 30×30 pixels) to yield a total of 52 2-D OCT feature maps of size 20×20 pixels.

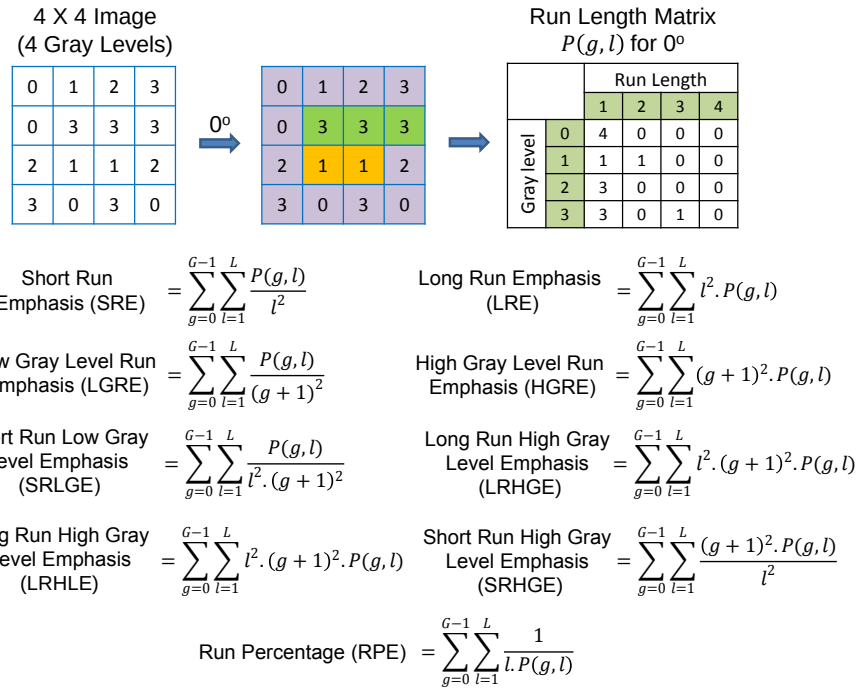

Figure 7.4: Schematic illustrating the process of building a gray level run length (GLRL) matrix. For a given direction (here 0°), the element (i, j) of the GLRL matrix denotes the number of times a run of length j and pixel value i is found in the image. Runs of length one, two, and three in the example image are color coded in purple, orange, and green respectively. Formulae to compute the eleven GLRL derived texture features are also listed.

7.2.4 Classifier Design and Evaluation

The objective of a classification algorithm is to assign a category or *class* to a new data-point belongs to based on the information obtained from an available set of pre-classified data-points called the *training set*. A data-point is characterized by certain attributes or *features*, and the problem of classifier design is that of estimating the parameters of a model describing the functional relationship between the features and class labels. The process of estimating these parameters constitutes the *training*

phase of a classifier design. To evaluate the classification accuracy of a classifier, the trained classifier is *tested* to predict the class of data-points in a *test set*, which have preferably not been used for training (i.e. not included in the training set). The predicted class labels produced by the classifier are compared with the true class labels of the test data (assumed to be known) to evaluate the classification accuracy of the classifier.

To evaluate the discriminatory potential of a set of features, a popular ensemble classification algorithm called random forest was used in this study. Ensemble based classification methods offer an attractive alternative to the traditional classification algorithms to deal with complex classification problems. An ensemble based method, in simple terms, combines several "weak classifiers" to produce a "strong classifier". This often results in an improved classification accuracy, which comes at the expense of a higher computational overhead. The advantages of an ensemble based method over a single classifier has been discussed in [91]. In this study, we used random forest, which is an ensemble of simple decision trees classifiers [92].

In the context of classification algorithms, a data-point characterized by n features is represented as a vector in a n-dimensional feature space. The process of classification for a m-class problem can then be thought of as partitioning the feature space into m different regions. A decision tree classifier partitions the feature space into disjoint rectangular regions based on a set of recursive binary rules. This is illustrated in Fig. 7.5 (b) for the case of a three-class problem in a 2-D feature space.

The rules in the case of the example shown in Fig. 7.5 (b) are: (i) Region 1 (green): Feature 1 > 25, (ii) Region 2 (red): (Feature 1 < 25), and (Feature 2 < 20), and (iii) Region 3 (blue): (Feature 1 < 25) and (Feature 2 > 20). These rules are graphically represented as a tree shown in Fig. 7.5 (a), where each split point or an *internal node* represents a binary question based on one of the features and the terminal nodes of the tree represent a class label. The process of training a decision tree involves determining the set of rules or the binary test conditions for each internal node of the decision tree. Classifying a test data-point is straightforward once the decision tree has been built. Starting from the top-most node, the data-point is propagated down the tree based on the decision taken at each internal node, until it reaches a terminal node. The class label associated with the terminal node is then assigned to the test data-point. While decision trees have several advantages like the ability to handle multiclass problems, robustness to outliers and computational efficiency, they suffer from disadvantages like low prediction accuracy for complex classification problems and high variance. Random forest overcomes the disadvantages of decision trees by forming an ensemble of several decision trees (denoted by n_{tree}, here) during its training phase [93]. Assuming that the training set consists of N data-points characterized by M features, each decision tree in a random forest is trained over a set of M data-points obtained by sampling by replacement from the pool of training data-points and f features chosen randomly from the M original features. In this study, we used $n_{tree} = 200$ and $f = \sqrt{M}$ for training the random forest. To classify

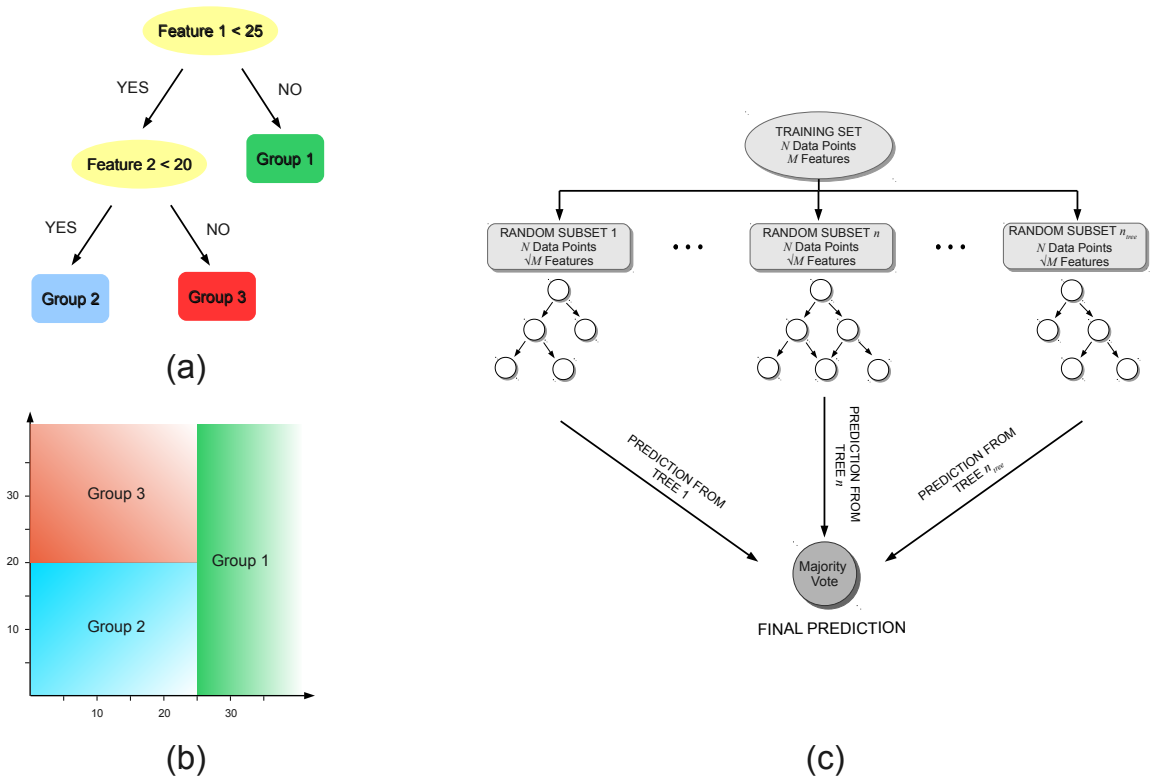

Figure 7.5: Random forest based classification. (a) Graphical representation of the decision process in form of a binary tree (b) Partitioning of the feature space based on the rules of the decision tree in (a) (c) The process of training and testing of a random forest.

a new data sample, the class of the data sample is first predicted by each decision tree and the final class predicted by the random forest is obtained by simply taking a majority vote of the classes predicted by individual trees. This process is illustrated in Fig. 7.5 (c).

To obtain an unbiased estimate of the classification accuracy, it is necessary to test the performance of the classifier on an independent test data that has not been used for training. Cross-validation is a commonly used, powerful resampling statistical technique for estimating the generalization performance (i.e. the performance

on data that has not been used for training) of an algorithm. In the context of classification, cross-validation provides a means of obtaining an unbiased estimate for the classification accuracy. In this study, a variant of the leave-one-out cross-validation (LOO CV) method was used to estimate the classification accuracy. In the standard LOO CV procedure, all but one data-points are used for training the classifier and the left out data-point is used for testing. The process of training and testing is repeated in an iterative round-robin fashion (each iteration called a *fold* of CV), until all the data-points are used as test data-points. Since the data-points in our study correspond to pixels in 2-D feature maps, to avoid optimistically biased accuracy estimates resulting from spatial correlation between pixels, we performed leave-one-sample-out cross-validation (LOSO CV), wherein CV folds were performed over the datasets and not pixels. In addition to the mean classification accuracy (obtained by averaging the accuracies obtained on individual CV folds), the classifier performance was also evaluated by computing the sensitivity and specificity for each class by pooling the results of the different CV folds.

7.2.5 Feature Selection for OCT Features

Feature selection is a process of selecting a subset of features from a large pool of features. The objective of feature selection is to remove redundant (correlated) and irrelevant features while retaining the most relevant features for building a predictive model. Getting rid of redundant and irrelevant features not just results in reduced computational cost, both in terms of training and testing the model, but

also provides a better understanding of the importance of different features in the classification model. Due to the large number of correlated OCT features, we used the Minimum Redundancy Maximum Relevance (mRMR) algorithm [94] to identify the most important OCT features. mRMR is a mutual information based powerful feature selection method that aims at selecting features that are mutually different but highly relevant for classification. The predictive power of the smaller set of OCT features obtained by mRMR algorithm was also evaluated by using a training and testing procedure similar to what was used for the complete set of OCT features.

7.2.6 Statistical Comparison of Different Feature Sets

Two types of non-parametric statistical tests were used to compare the performance of different feature sets. To compare the performance of two sets of features, Wilcoxon signed rank test was used. The Wilcoxon test is a nonparametric procedure for comparing two sets of paired observations. The classification accuracies for different CV folds for classifiers based on the two feature sets were treated as the different observations. The null hypothesis for the test was that there there was no difference in the accuracies achieved by classifiers based on the two sets of features and the two-sided alternative hypothesis stated that it was otherwise. The second type of statistical test, namely, the Friedman test, was used to compare the performance of more than two feature sets. The Friedman test is the non-parametric equivalent of the ANOVA test. The null hypothesis for the Friedman test was that there was no difference in the accuracies achieved by classifiers based on the dif-

ferent sets of features being compared, and the alternative hypothesis stated that there was at least one pair of feature sets that had different classification accuracies. Briefly, the Friedman test ranks the different features sets being compared for each cross-validation fold based on the classification accuracies. The average ranks for the different feature sets are then used to compute a test statistic (χ_F^2 statistic) which is compared against a critical value determined based on a pre-determined significance level to check whether the measured average ranks are significantly different from the mean rank. If the critical value is less than or equal to the test statistic, the null hypothesis is rejected in favor of the alternative hypothesis. In such a case, a post-hoc test is conducted to identify which features sets are different. In this study, Holm procedure was used as a post-hoc test to compare the performance of the best feature set (as judged by the mean ranks obtained during Friedman test) against the remaining feature sets. Holm procedure compares a set of logically interrelated hypothesis of comparisons between the control and other feature sets. For each pairwise comparison, the p value is computed based on the mean rank difference between the two groups and the null hypothesis that there is no difference between the two groups is rejected if the p value is found to be less than an adjusted α value (called Holm α in this study).The choice of the Holm procedure was motivated by the simplicity and power of the test for performing multiple comparisons as described in [95].

Table 7.1: Results of Wilcoxon signed rank test for comparing the classification accuracies of the exact and approximate FLIM features ($n = 48, \alpha = 0.05$)

Feature Sets Compared	R^+	R^-	T statistic	z statistic	p value
Exact FLIM - Approx. FLIM	156.5	371.5	156.5	-2.010	0.044

7.3 Results and Discussions

7.3.1 Comparison of the Exact and Approximate FLIM Features

The mean classification accuracy for the exact and approximate FLIM features was found to be 83.7% and 80.7%, respectively. To test whether, in general, the exact FLIM features performed better than the approximate features, Wilcoxon signed rank test was performed. Out of the 48 pair-wise comparisons (corresponding to 48 LOSO cross-validation folds), the overall accuracy for the exact FLIM features was found to be the same as that for the approximate FLIM features in 16 comparisons, higher in 23 comparisons, and lower in the remaining 9 comparisons (refer Table A.1). The results of the Wilcoxon signed rank test ($n = 48, \alpha = 0.05$) summarized in Table 7.1 indicated that the classification accuracies for the exact FLIM features were statistically different (borderline p value = 0.044, $\alpha = 0.05$) than those for the approximate features. Although the mean accuracy for the exact FLIM features was found to be statistically higher than the approximate FLIM features, the borderline p-value for the Wilcoxon test indicates that the difference between the overall accuracies for the two sets of FLIM features was not substantive. This suggests that

Table 7.2: Results of Friedman test for comparing the classification accuracies of different FLIM feature sets ($n = 48, df = 3, \alpha = 0.05$)

	Feature Sets				χ^2_F statistic	p value
	All	Int.	Int. & $\tau_{1/e}$	Int. & τ_{avg}		
Mean Rank	3.4	1.6	2.2	2.8	58.02	<0.001
Mean Accuracy	0.836	0.638	0.690	0.784		

an accuracy as high as that obtained by using the exact FLIM features can, in fact, be obtained by using the approximate FLIM features. The advantage of using approximate features over the exact features being that estimating the approximate FLIM features obviates the need for deconvolution and thus requires significantly less computational effort.

7.3.2 Comparison of Intensity and Lifetime Features

To assess the improvement in the diagnostic accuracy achieved by using both intensity and lifetime information, as opposed to only intensity, the classification accuracies for the following four sets of exact FLIM features were compared: (i) All FLIM features (3 normalized intensities, 6 lifetimes), (ii) Intensities only (3 features), (iii) Intensities and $1/e$ lifetimes (6 features), and (iv) Intensities and average lifetimes (6 features). As described earlier, for each cross-validation fold, all but one datasets were used for training the classifier and the left-out dataset was used to evaluate the classification accuracy. The classification accuracies for the different sets of FLIM features evaluated over different cross-validation folds are listed in Ta-

Table 7.3: Post-hoc comparison table for Friedman test for comparing different exact FLIM features ($n = 48, \alpha = 0.05$)

Hypothesis Index	Feature Sets Compared	Mean Rank Difference	z statistic	p value	Holm α
1	All - Intensity	1.81	6.88	<0.01	0.017
2	All - Intensity & $\tau_{1/e}$	1.22	4.62	<0.01	0.025
3	All - Intensity & τ_{avg}	0.64	2.41	0.016	0.05

ble A.2. To test for statistical differences between the four sets of FLIM features, Friedman test ($n = 48, \alpha = 0.05$) was performed. The results of the Friedman test ($\chi^2_F = 58.02, df = 3, p < 0.001$), summarized in Table 7.2, led to the rejection of the null hypothesis, suggesting that significant difference exists between the classification accuarcies of one or more feature sets. Based on the mean accuracies and ranks of the different feature sets summarized in Table 7.2, it was hypothesized that classification performance based on All FLIM features was better than the other feature sets. To test this hypothesis, Holm post-hoc procedure was conducted in which the classification accuracy of all FLIM features was compared with the other three feature sets. The results of the Holm procedure are presented in Table 7.3. Based on the results of the Holm procedure, all three hypotheses corresponding to the pairwise comparisons between All FLIM features and the other three feature sets were rejected suggesting that the performance of All FLIM features was statistically better that the other three feature sets. These results are in agreement with the findings of an earlier study investigating the potential of time-resolved fluorescence measurements for oral

cancer in a hamster cheek pouch model [96], where the authors found that using both intensity and lifetime features as opposed to only intensity features resulted in a significant improvement in the overall classification accuracy. The poor performance of intensity based imaging systems in oral cancer screening has also been reported in several other studies [97,98], where it has been noted that there is lack of substantive evidence to suggest that the use of autofluorescence intensity based imaging system improves the sensitivity and specificity of oral cancer beyond the conventional oral examination.

Also, the fact that using both lifetimes $\tau_{1/e}$ and τ_{avg} along with intensity results in a statistically higher overall accuracy compared to using either of them with intensity, suggests that using both lifetimes provide a more complete description of the fluorescence decay dynamics. A similar result was reported in [96], where the authors report highest overall classification accuracy for a combination of intensity, average lifetime and zeroth order Laguerre coefficient features. Using both average lifetime and zeroth order Laguerre coefficient in this case provides a better characterization of the fluorescence decay, much like the combination of $\tau_{1/e}$ and τ_{avg} in our study.

7.3.3 Comparison of FLIM and OCT Features

The mean accuracies and the ranks for the FLIM (9 features), OCT (52 features), and FLIM & OCT (61 features) features are listed in Table 7.4 and a detailed list of the classification accuracies for different cross-validation folds is presented in Table A.4. To test for statistical differences between the three sets of features,

Table 7.4: Results of Friedman test for comparing the classification accuracies of FLIM and OCT features ($n = 48, \alpha = 0.05$)

	Feature Sets			χ^2_F statistic	p value
	FLIM & OCT	FLIM	OCT		
Mean Rank	2.5	2.0	1.5	26.97	<0.001
Mean Accuracy	0.871	0.837	0.809		

Friedman test ($n = 48, \alpha = 0.05$) was performed. The results of the Friedman test ($\chi^2_F = 58.02, df = 3, p < 0.001$), summarized in Table 7.4, led to the rejection of the null hypothesis, suggesting that significant difference exists between the classification accuarcies of two or more feature sets. Based on the mean accuracies and ranks of the different feature sets, it was hypothesized that combining FLIM and OCT features leads to better classification accuracy than using either FLIM or OCT features. To test this hypothesis, Holm test was performed to compare the classification accuracy of the combined FLIM & OCT features with the individual OCT and FLIM features. Based on the results of the Holm procedure presented in Table 7.5, the two hypotheses corresponding to the pairwise comparisons between the combined FLIM & OCT features and the individual OCT and FLIM features were rejected suggesting that the classification accuracies for the combined FLIM & OCT features were in general, better that the other the individual OCT or FLIM features.

In addition to the mean classification accuracies, the sensitivity and specificity for each class (benign, pre-cancerous and cancerous) for the FLIM and OCT features

Table 7.5: Post-hoc comparison table for Friedman test for FLIM and OCT features ($n = 48, \alpha = 0.05$)

Hypothesis Index	Feature Sets Compared	Mean Rank Difference	z statistic	p value	Holm α
1	FLIM & OCT - OCT	0.948	4.64	<0.01	0.025
2	FLIM & OCT - FLIM	0.427	2.09	0.036	0.05

Table 7.6: Sensitivity and specificity for FLIM and OCT features

	Sensitivity			Specificity		
	Feature Sets			Feature Sets		
CLASS	FLIM & OCT	FLIM	OCT	FLIM & OCT	FLIM	OCT
Benign	0.883	0.876	0.784	0.909	0.918	0.878
Pre-cancerous	0.802	0.760	0.768	0.956	0.925	0.861
Cancerous	0.902	0.833	0.879	0.916	0.888	0.943

were also computed. Based on the sensitivity and specificity values listed in Table 7.6, it can be said that the FLIM features had higher sensitivity and specificity than the OCT features for the benign class. On the other hand, OCT features had better sensitivity and specificity than the FLIM features for the cancerous class. For the pre-cancerous class, the two sets of features performed comparably. By combining both FLIM and OCT features, best sensitivity and specificity was achieved for all the classes. The stacked bar graphs shown in Figure 7.6, provide further insights into the classification performance. The graph shows the proportion of samples belonging to a given class: benign, pre-cancerous, or cancerous that were classified correctly or

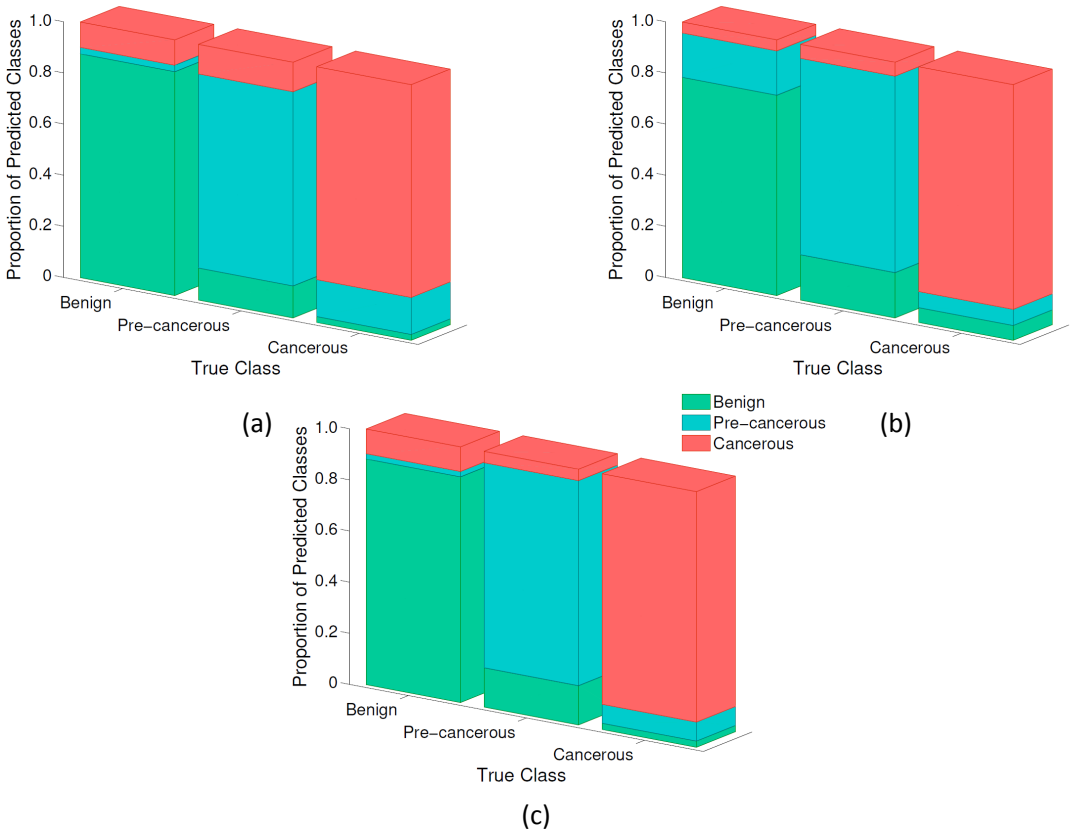

Figure 7.6: Stacked bar graph showing the proportion of samples belonging to a given class: benign, pre-cancerous, or cancerous (x axis, true class) that were classified correctly (predicted as belonging to the same class) or incorrectly (predicted as belonging to one of the other two classes) for (a) FLIM features (b) OCT features (c) FLIM & OCT features.

incorrectly. The bar graph in Figure 7.6 (a) suggests that the classification based on the FLIM features provides relatively poor discrimination between the pre-cancerous and cancerous samples (cyan and red) compared to the classification based on the OCT features. A possible reason for this could be that the information contained in the fluorescence signal obtained from the samples in the pre-cancerous and cancerous classes was not discriminatory enough to achieve an accurate class separation, a fact

noted by several other researchers investigating the potential of fluorescence based imaging methods for the diagnosis of oral cancer [96, 99, 100]. In contrast, significant difference in tissue morphology between the pre-cancerous and cancerous classes enables superior performance of the OCT features.

Likewise, the bar graph in Figure 7.6 (b) suggests that the OCT features perform poorly compared to the FLIM features in discriminating benign samples from pre-cancerous samples (green and cyan). Following similar reasoning as before, this confusion between the two classes could have possibly resulted from the lack of sensitivity of the OCT features used in this study, to characterize differences in tissue morphology between samples in the benign and pre-cancerous classes. To overcome this limitation, more OCT features that are capable of characterizing morphological indicators of early dysplasia like changes in keratinization, epithelial thickening, irregular epithelial stratification and broadening of rete ridges could be evaluated and combined with the existing set of OCT features. Although a standard criteria of interpreting OCT B-scans for grading oral dysplasia has not been developed yet, previous studies on OCT-based diagnosis of oral cancer, both in hamster cheek pouches [18–20] and humans [21], have been successful in identifying the aforementioned histologically relevant morphological features in OCT B-scans, for diagnosing oral pre-malignancies and malignancies.

The classification based on both FLIM and OCT features takes advantage of the complimentary nature of the two feature sets to yield an improved performance

compared to the classification based on either of those feature sets. This is indicated by the highest sensitivity and specificity values for the combined FLIM and OCT features, for all three classes.

It is of relevance to note that the performance of OCT-based classification is mainly limited by the nature of OCT features in terms of their ability to provide a sufficiently detailed description of tissue morphology. In this sense, one could expect to achieve a superior classification performance by using a set of more descriptive and richer OCT features. In the case of FLIM, however, a bigger limitation arises from two other factors: (i) the difficulty to identify the specific sources contributing to the bulk fluorescence measurements, and (ii) the complex and sometimes similar nature of alterations in metabolic cofactors and structural proteins that occur in both benign and malignant oral conditions. For example, loss of stromal fluorescence is observed both in benign tissue with chronic inflammation caused by the breakdown of collagen crosslinks and in dysplastic tissue due to epithelial thickening and degradation of stromal collagen [18,101,102]. Similarly, an increase in keratin fluorescence can be observed in both benign and malignant oral conditions, due to the presence of keratotic lesions in both conditions [103, 104]. This was also noticed in the current study, where histological evaluation of several samples in both the benign and pre-cancerous classes revealed the presence of hyperkeratosis. Although an increase in NADH fluorescence originating from the epithelial layer has been reported to be strongly correlated with neoplastic progression [2, 16, 102], in the presence of kera-

tinized epithelium, most of the excitation light is back-scattered, which significantly reduces the fluorescence signal obtained from NADH. Morepver, the similarity in the spectral and temporal fluorescence characteristics of collagen and keratin [105, 106] further confounds the FLIM-based diagnosis of oral dysplasia.

Another possible reason for the relatively inferior performance of the different feature sets for the pre-cancerous class could be the presence of mislabeled pixels (data-points) in the training data that belong to the pre-cancerous class. As mentioned earlier, a sample was labeled pre-cancerous if the histological evaluation of at least 50% of sections in that sample indicated some grade of dysplasia. This was done due to the lack of samples belonging to the pre-cancerous class that had sufficiently homogeneous evaluation across all the histology sections. As a result of this, not all the pixels in a pre-cancerous sample (although all labeled as pre-cancerous) were truly representative of pre-cancerous conditions. We speculate that the "label noise" arising in this way could also be responsible for the confusion between the pre-cancerous and other classes.

7.3.4 Selected OCT Features

To obtain a smaller set of most discriminatory OCT features from the original set of OCT features, 52 sequential feature sets $S_1, S_2, \ldots, S_{52}$ ($S_1 \subset S_2 \subset \ldots S_{52}$) were obtained using the mRMR incremental feature selection method. The sequential feature sets are ordered such that the mth. feature set, S_m contains the m most discriminatory features. The mean classification accuracies for the sequential feature

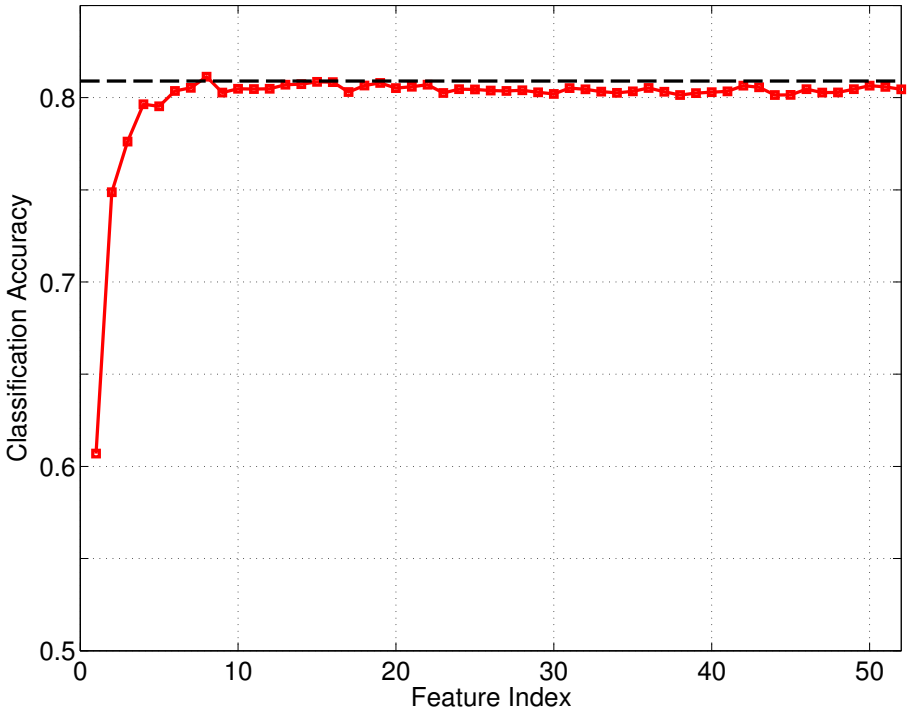

Figure 7.7: Mean classification accuracies for the sequential OCT feature sets using mRMR incremental feature selection procedure. The dashed black line line denotes the mean accuracy obtained by using all 52 OCT features.

sets were subsequently computed by using a random forest based training and testing procedure similar to what was used for the complete set of OCT features. Figure 7.7 shows the mean classification accuracies for the 52 sequential feature sets. The plot suggests that using more than six features does not offer a significant improvement in the mean classification accuracy; accuracy for the best six features being 0.804 compared to 0.809 for all OCT features. Specifically, the set of six most important OCT features obtained by the mRMR algorithm included both A-line and B-scan derived features, viz. : (i) *std*(crossings), (ii) LRLGE (90°, 32 bits), (iii) RP (0°, 2 bits), (iv) $\Sigma p_i + \Sigma v_i$, (v) RP (90°, 32 bits), and (vi) SRHGE (0°, 2 bits).

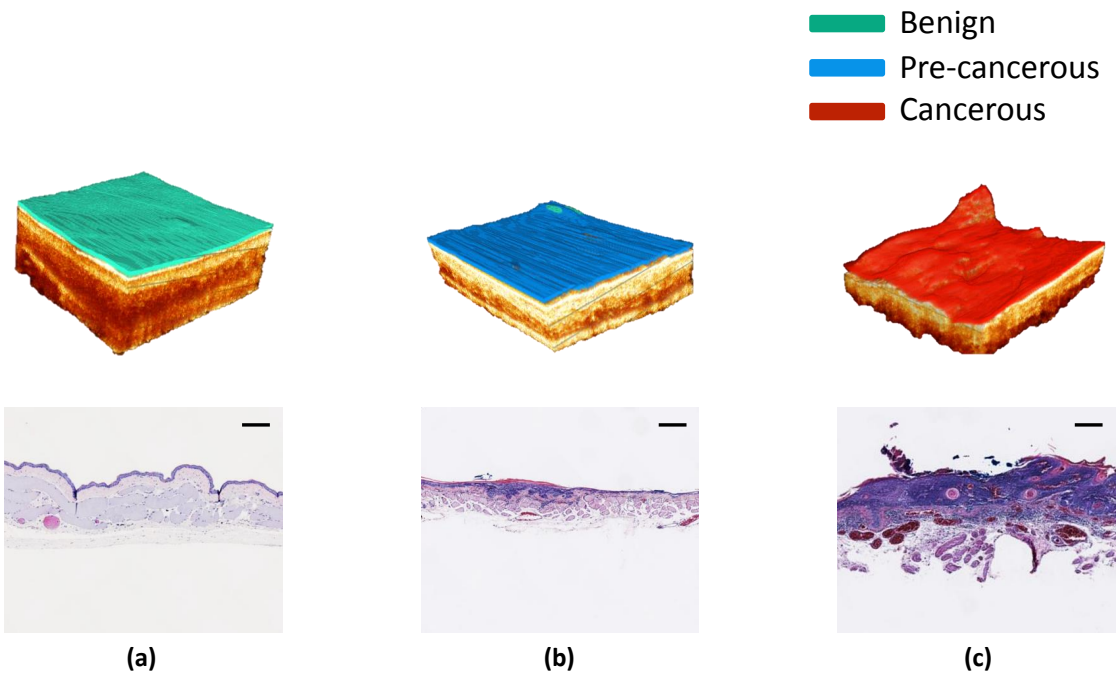

Figure 7.8: Results of the classification presented as diagnostic maps overlaid on the OCT volumes for (a) benign (b) pre-cancerous and (c) cancerous samples. Also shown are the representative histology sections taken from the samples. Scale bars represent 200 μm

7.4 Conclusion

Very few studies have investigated the diagnostic potential of FLIM and OCT for oral cancer. Even fewer studies have focused on algorithms for objective characterization of the biochemical and morphological changes associated with the progression of oral cancer. In this study, we demonstrated, perhaps for the first time, the feasibility of using automated quantitative image analysis algorithms for extracting relevant biochemical and morphological features from 3-D FLIM and OCT datasets, and using those features to perform automated diagnosis of oral cancer. The results of the

classification algorithm could be presented in form of a diagnostic map overlaid on the corresponding OCT volume for a better diagnostic interpretation as shown in Fig. 7.8.

The main finding to emerge from the present study is that the synergy of biochemical and morphological information obtained from FLIM and OCT, respectively, increases the sensitivity and specificity for detecting malignant and pre-malignant lesions, compared to using features from only one type of modality. The second major finding of our study is that using both intensity and lifetime FLIM features, as opposed to only intensity features, provides significant improvement in the diagnostic accuracy. To circumvent the computational effort of deconvolution to obtain the lifetimes, the performance of a new set of FLIM features, called the "approximate" FLIM features was also analyzed. The results of this analysis indicated that a diagnostic power as high as that of the exact FLIM features can in fact be obtained by using the approximate FLIM features. The advantage of using approximate features over the exact features being that estimating the approximate features does not require deconvolution and thus significantly reduces the computational effort.

The findings of this study are significant because they demonstrate the feasibility of using automated algorithms for performing the diagnosis of pre-malignant and malignant lesions based on FLIM and OCT data. We recognize that the sample size used in this study was rather small, and were not truly representative of the vast gamut of histological alterations that accompany the progression of oral can-

cer. A further study using a larger pool of samples with more diverse histological presentations is therefore warranted to fully substantiate the findings of the current study.

8. SUMMARY

With significant progress made in the design and instrumentation of optical imaging systems, factors like acquisition speed and data transfer rate, which presented early challenges in the development of various optical imaging techniques are no longer a major concern. The high-speed imaging capability of these systems, however, poses a new challenge of processing, interpreting and visualizing the vast amount of information contained in the data collected in near real-time. The prohibitively large amount of data obtained from these systems makes manual analysis by an expert virtually impossible. In the absence of automated methods for data analysis, then, the full potential of these optical imaging technologies remains largely underutilized. This is an even bigger issue in the case of functional imaging modalities like FLIM, where the indirect nature of the imaging signals makes the interpretation of images (fluorescence intensity and lifetime maps in the case of FLIM) complex and less intuitive. The lack of tools for automated analysis for diagnostic applications, a problem which remains largely unaddressed, formed the central theme of this dissertation. An automated image analysis approach involves three major steps, namely, feature extraction, classification, and visualization. In this dissertation, several computational methods for performing these different steps were described in the context of two imaging modalities: OCT and FLIM. The results of this study demonstrated the feasibility of using automated methods for extracting biochemical information from

FLIM data and morphological information from OCT data and combining them for a more comprehensive diagnosis of atherosclerosis and oral cancer.

Use of automated algorithms for clinical diagnosis, which form the basis of computer aided diagnosis (CAD) [107, 108], has already started to make an impact in conventional radiology. One of the most successful applications of CAD has been in mammography based screening for breast cancer, where CAD based large prospective studies like [109] have reported a gain of approximately 20% in the early detection of malignant breast tumors in mammograms. The success of CAD in breast cancer screening and diagnosis has led to commercialized CAD systems like ImageChecker® (Hologic, Inc.) and M-Vu CAD® (VuCOMP, Plano, Texas) have been successful in gaining approval from the U.S food and drug administration (FDA). It is reported that more than 1500 CAD systems are currently in use in assisting radiologists in the early detection of breast cancer at many hospitals, clinics and screening centers around the world [110]. Other areas in radiology where CAD systems are used include detection of lung nodules in X-ray images (Philips xLNA Enterprise), and diagnosis of advanced prostrate cancer based on bone scintigraphy (EXINI Diagnostics, Sweden), to name a few. The initial success of CAD in radiological imaging has encouraging implications for the use of automated methods in optical imaging.

Most optical imaging modalities, although showcased as promising diagnostic tools in the academic world, remain far from being applicable in a clinical setting. At this time, it is difficult to speculate the success of optical imaging in clinical

diagnosis. However, there can be little doubt that automated data analysis will play a pivotal role in the successful commercialization of any optical imaging modality by enabling large scale quantitative cross-sectional studies in the validation phase and eventually by enhancing the diagnostic power in the deployment phase. In this sense, automated data analysis is one of the essential pillars on which the future of optical imaging rests.

REFERENCES

[1] J. G. Fujimoto, C. Pitris, S. A. Boppart, and M. E. Brezinski, "Optical coherence tomography: an emerging technology for biomedical imaging and optical biopsy," *Neoplasia (New York, NY)*, vol. 2, no. 1-2, pp. 9–25, 2000.

[2] I. Pavlova, K. Sokolov, R. Drezek, A. Malpica, M. Follen, and R. Richards-Kortum, "Microanatomical and biochemical origins of normal and precancerous cervical autofluorescence using laser-scanning fluorescence confocal microscopy," *Photochemistry and Photobiology*, vol. 77, no. 5, pp. 550–555, 2003.

[3] M. Xu and L. V. Wang, "Photoacoustic imaging in biomedicine," *Review of Scientific Instruments*, vol. 77, no. 4, pp. 1–22, 2006.

[4] K. König, A. Ehlers, I. Riemann, S. Schenkl, R. Bückle, and M. Kaatz, "Clinical two-photon microendoscopy," *Microscopy Research and Technique*, vol. 70, no. 5, pp. 398–402, 2007.

[5] C. W. Freudiger, W. Min, B. G. Saar, S. Lu, G. R. Holtom, C. He, J. C. Tsai, J. X. Kang, and X. S. Xie, "Label-free biomedical imaging with high sensitivity by stimulated raman scattering microscopy," *Science*, vol. 322, no. 5909, pp. 1857–1861, 2008.

[6] R. Rosen, A. G. Podoleanu, L. A. Yannuzzi, R. Weitz, J. A. Rogers, Y. Fisher, G. M. Dobre, P. Garcia, J. Nieto, R. G. Cucu *et al.*, "Combined multiplanar

optical coherence tomography and confocal scanning ophthalmoscopy," *Journal of Biomedical Optics*, vol. 9, no. 1, pp. 86–93, 2004.

[7] C. Xu, C. Vinegoni, T. S. Ralston, W. Luo, W. Tan, and S. A. Boppart, "Spectroscopic spectral-domain optical coherence microscopy," *Optics Letters*, vol. 31, no. 8, pp. 1079–1081, 2006.

[8] P. Kim, M. Puorishaag, D. Côté, C. P. Lin, and S. H. Yun, "In vivo confocal and multiphoton microendoscopy," *Journal of Biomedical Optics*, vol. 13, no. 1, pp. 010 501–010 501, 2008.

[9] C. P. Fleming, V. V. Fedorov, A. M. Rollins, I. R. Efimov, W. J. Hucker, and C. M. Ripplinger, "Bimodal biophotonic imaging of the structure-function relationship in cardiac tissue," *Journal of Biomedical Optics*, vol. 13, no. 5, pp. 054 012–054 012, 2008.

[10] B. W. Graf and S. A. Boppart, "Multimodal in vivo skin imaging with integrated optical coherence and multiphoton microscopy," *IEEE Journal of Selected Topics in Quantum Electronics*, vol. 18, no. 4, pp. 1280–1286, 2012.

[11] H. Fatakdawala, S. Poti, F. Zhou, Y. Sun, J. Bec, J. Liu, D. R. Yankelevich, S. P. Tinling, R. F. Gandour-Edwards, D. G. Farwell *et al.*, "Multimodal in vivo imaging of oral cancer using fluorescence lifetime, photoacoustic and ultrasound techniques," *Biomedical Optics Express*, vol. 4, no. 9, pp. 1724–1741, 2013.

[12] R. Virmani, A. P. Burke, A. Farb, and F. D. Kolodgie, "Pathology of the

vulnerable plaque," *Journal of the American College of Cardiology*, vol. 47, no. 8, pp. C13–C18, 2006.

[13] R. Virmani, F. D. Kolodgie, A. P. Burke, A. Farb, and S. M. Schwartz, "Lessons from sudden coronary death a comprehensive morphological classification scheme for atherosclerotic lesions," *Arteriosclerosis, Thrombosis, and Vascular Biology*, vol. 20, no. 5, pp. 1262–1275, 2000.

[14] N. Howlader, A. Noone, M. Krapcho, N. Neyman, R. Aminou, S. Altekruse, C. Kosary, J. Ruhl, Z. Tatalovich, H. Cho *et al.*, "Seer cancer statistics review, 1975–2009 (vintage 2009 populations)," *Bethesda, MD: National Cancer Institute*, 2012.

[15] V. K. Ramanujan, J.-H. Zhang, E. Biener, and B. Herman, "Multiphoton fluorescence lifetime contrast in deep tissue imaging: prospects in redox imaging and disease diagnosis," *Journal of Biomedical Optics*, vol. 10, no. 5, pp. 051 407–051 407, 2005.

[16] M. C. Skala, J. M. Squirrell, K. M. Vrotsos, J. C. Eickhoff, A. Gendron-Fitzpatrick, K. W. Eliceiri, and N. Ramanujam, "Multiphoton microscopy of endogenous fluorescence differentiates normal, precancerous, and cancerous squamous epithelial tissues," *Cancer Research*, vol. 65, no. 4, pp. 1180–1186, 2005.

[17] M. C. Skala, K. M. Riching, D. K. Bird, A. Gendron-Fitzpatrick, J. Eickhoff, K. W. Eliceiri, P. J. Keely, and N. Ramanujam, "In vivo multiphoton fluores-

cence lifetime imaging of protein-bound and free nicotinamide adenine dinucleotide in normal and precancerous epithelia," *Journal of Biomedical Optics*, vol. 12, no. 2, pp. 024 014–024 014, 2007.

[18] P. Wilder-Smith, K. Osann, N. Hanna, N. E. Abbadi, M. Brenner, D. Messadi, and T. Krasieva, "In vivo multiphoton fluorescence imaging: a novel approach to oral malignancy," *Lasers in Surgery and Medicine*, vol. 35, no. 2, pp. 96–103, 2004.

[19] E. S. Matheny, R. Mina-Araghi, M. Brenner, N. M. Hanna, W. Jung, Z. Chen, and P. Wilder-Smith, "Optical coherence tomography of malignancy in hamster cheek pouches," *Journal of Biomedical Optics*, vol. 9, no. 5, pp. 978–981, 2004.

[20] P. Wilder-Smith, T. Krasieva, W.-G. Jung, J. Zhang, Z. Chen, K. Osann, and B. Tromberg, "Noninvasive imaging of oral premalignancy and malignancy," *Journal of Biomedical Optics*, vol. 10, no. 5, pp. 051 601–051 601, 2005.

[21] P. Wilder-Smith, K. Lee, S. Guo, J. Zhang, K. Osann, Z. Chen, and D. Messadi, "In vivo diagnosis of oral dysplasia and malignancy using optical coherence tomography: preliminary studies in 50 patients," *Lasers in Surgery and Medicine*, vol. 41, no. 5, pp. 353–357, 2009.

[22] J. R. Lakowicz, *Principles of fluorescence spectroscopy.* (Springer, New York, USA, 2009).

[23] B. Q. Spring and R. M. Clegg, "Frequency-domain FLIM," in *FLIM Microscopy*

in Biology and Medicine. (Chapman & Hall/CRC, Boca Raton, FL, USA, 2010).

[24] M. Choma, M. Sarunic, C. Yang, and J. Izatt, "Sensitivity advantage of swept source and fourier domain optical coherence tomography," *Optics Express*, vol. 11, no. 18, pp. 2183–2189, 2003.

[25] M. E. Brezinski, *Optical coherence tomography: principles and applications*. (Academic press, Burlington, MA, USA, 2006).

[26] W. Drexler and J. G. Fujimoto, *Optical coherence tomography: technology and applications*. (Springer, Berlin, Germany, 2008).

[27] J. Izatt and M. Choma, "Theory of optical coherence tomography," in *Optical coherence tomography*. (Springer, Berlin, Germany, 2008).

[28] J. Park, J. A. Jo, S. Shrestha, P. Pande, Q. Wan, and B. E. Applegate, "A dual-modality optical coherence tomography and fluorescence lifetime imaging microscopy system for simultaneous morphological and biochemical tissue characterization," *Biomedical Optics Express*, vol. 1, no. 1, pp. 186–200, 2010.

[29] S. Shrestha, B. E. Applegate, J. Park, X. Xiao, P. Pande, and J. A. Jo, "High-speed multispectral fluorescence lifetime imaging implementation for in vivo applications," *Optics Letters*, vol. 35, no. 15, pp. 2558–2560, 2010.

[30] I. H. van Stokkum, D. S. Larsen, and R. van Grondelle, "Global and target analysis of time-resolved spectra," *Biochimica et Biophysica Acta (BBA)-*

Bioenergetics, vol. 1657, no. 2, pp. 82–104, 2004.

[31] W. R. Ware, L. J. Doemeny, and T. L. Nemzek, "Deconvolution of fluorescence and phosphorescence decay curves. least-squares method," *The Journal of Physical Chemistry*, vol. 77, no. 17, pp. 2038–2048, 1973.

[32] K. Lee, J. Siegel, S. Webb, S. Leveque-Fort, M. Cole, R. Jones, K. Dowling, M. Lever, and P. French, "Application of the stretched exponential function to fluorescence lifetime imaging," *Biophysical Journal*, vol. 81, no. 3, pp. 1265–1274, 2001.

[33] V. Ramanujan, J. Jo, G. Cantu, and B. Herman, "Spatially resolved fluorescence lifetime mapping of enzyme kinetics in living cells," *Journal of Microscopy*, vol. 230, no. 3, pp. 329–338, 2008.

[34] J. A. Jo, Q. Fang, and L. Marcu, "Ultrafast method for the analysis of fluorescence lifetime imaging microscopy data based on the laguerre expansion technique," *IEEE Journal of Selected Topics in Quantum Electronics*, vol. 11, no. 4, pp. 835–845, 2005.

[35] V. Z. Marmarelis, "Identification of nonlinear biological systems using laguerre expansions of kernels." *Annals of Biomedical Engineering*, vol. 21, no. 6, pp. 573–589, 1993.

[36] A. S. Dabir, C. A. Trivedi, Y. Ryu, P. Pande, and J. A. Jo, "Fully automated deconvolution method for on-line analysis of time-resolved fluorescence spec-

troscopy data based on an iterative laguerre expansion technique," *Journal of Biomedical Optics*, vol. 14, no. 2, pp. 024 030–024 030, 2009.

[37] D. Elson, J. Jo, and L. Marcu, "Miniaturized side-viewing imaging probe for fluorescence lifetime imaging (FLIM): validation with fluorescence dyes, tissue structural proteins and tissue specimens," *New Journal of Physics*, vol. 9, no. 5, p. 127, 2007.

[38] N. Ramanujam, "Fluorescence spectroscopy of neoplastic and non-neoplastic tissues." *Neoplasia*, vol. 2, no. 1-2, pp. 89–117, 2000.

[39] R. Richards-Kortum and E. Sevick-Muraca, "Quantitative optical spectroscopy for tissue diagnosis," *Annual Review of Physical Chemistry*, vol. 47, no. 1, pp. 555–606, 1996.

[40] Q. Fang, T. Papaioannou, J. A. Jo, R. Vaitha, K. Shastry, and L. Marcu, "Time-domain laser-induced fluorescence spectroscopy apparatus for clinical diagnostics," *Review of Scientific Instruments*, vol. 75, no. 1, pp. 151–162, 2004.

[41] P. Olivier, "Online system identification using laguerre series," *IEEE Proceedings-Control Theory and Applications*, vol. 141, no. 4, pp. 249–254, 1994.

[42] B. Wahlberg, "System identification using laguerre models," *IEEE Transactions on Automatic Control*, vol. 36, no. 5, pp. 551–562, 1991.

[43] C. Zervos, P. Belanger, and G. A. Dumont, "On pid controller tuning using orthonormal series identification," *Automatica*, vol. 24, no. 2, pp. 165–175, 1988.

[44] N. Galletly, J. McGinty, C. Dunsby, F. Teixeira, J. Requejo-Isidro, I. Munro, D. Elson, M. Neil, A. Chu, P. French *et al.*, "Fluorescence lifetime imaging distinguishes basal cell carcinoma from surrounding uninvolved skin," *British Journal of Dermatology*, vol. 159, no. 1, pp. 152–161, 2008.

[45] M.-A. Mycek, K. T. Schomacker, and N. S. Nishioka, "Colonic polyp differentiation using time-resolved autofluorescence spectroscopy," *Gastrointestinal Endoscopy*, vol. 48, no. 4, pp. 390–394, 1998.

[46] L. Marcu, "Fluorescence lifetime in cardiovascular diagnostics," *Journal of Biomedical Optics*, vol. 15, no. 1, pp. 011 106–011 106, 2010.

[47] J. A. Jo, B. E. Applegate, J. Park, S. Shrestha, P. Pande, I. B. Gimenez-Conti, and J. L. Brandon, "In vivo simultaneous morphological and biochemical optical imaging of oral epithelial cancer," *IEEE Transactions on Biomedical Engineering*, vol. 57, no. 10, pp. 2596–2599, 2010.

[48] P. J. Verveer, A. Squire, and P. I. Bastiaens, "Global analysis of fluorescence lifetime imaging microscopy data," *Biophysical Journal*, vol. 78, no. 4, pp. 2127–2137, 2000.

[49] G. Kremers, E. B. Van Munster, J. Goedhart, and T. W. Gadella Jr, "Quan-

titative lifetime unmixing of multiexponentially decaying fluorophores using single-frequency fluorescence lifetime imaging microscopy," *Biophysical Journal*, vol. 95, no. 1, pp. 378–389, 2008.

[50] K. Lee, J. Siegel, S. Webb, S. Leveque-Fort, M. Cole, R. Jones, K. Dowling, M. Lever, and P. French, "Application of the stretched exponential function to fluorescence lifetime imaging," *Biophysical Journal*, vol. 81, no. 3, pp. 1265–1274, 2001.

[51] A. Clayton, Q. Hanley, and P. Verveer, "Graphical representation and multicomponent analysis of single-frequency fluorescence lifetime imaging microscopy data," *Journal of Microscopy*, vol. 213, no. 1, pp. 1–5, 2004.

[52] S. Schlachter, S. Schwedler, A. Esposito, G. K. Schierle, G. Moggridge, and C. Kaminski, "A method to unmix multiple fluorophores in microscopy images with minimal a priori information," *Optics Express*, vol. 17, no. 25, pp. 22 747–22 760, 2009.

[53] A. Cichocki, R. Zdunek, A. H. Phan, and S. Amari, *Nonnegative matrix and tensor factorizations: applications to exploratory multi-way data analysis and blind source separation*. (Wiley, West Sussex, UK, 2009).

[54] N. Keshava and J. F. Mustard, "Spectral unmixing," *IEEE Signal Processing Magazine*, vol. 19, no. 1, pp. 44–57, 2002.

[55] H. Grahn and P. Geladi, *Techniques and applications of hyperspectral image*

analysis. (Wiley, West Sussex, UK, 2007).

[56] J. M. Nascimento and J. M. Dias, "Does independent component analysis play a role in unmixing hyperspectral data?" *IEEE Transactions on Geoscience and Remote Sensing*, vol. 43, no. 1, pp. 175–187, 2005.

[57] J. M. Bioucas-Dias, A. Plaza, N. Dobigeon, M. Parente, Q. Du, P. Gader, and J. Chanussot, "Hyperspectral unmixing overview: Geometrical, statistical, and sparse regression-based approaches," *IEEE Journal of Selected Topics in Applied Earth Observations and Remote Sensing,*, vol. 5, no. 2, pp. 354–379, 2012.

[58] T.-H. Chan, W.-K. Ma, C. Chi, and Y. Wang, "A convex analysis framework for blind separation of non-negative sources," *IEEE Transactions on Signal Processing*, vol. 56, no. 10, pp. 5120–5134, 2008.

[59] J. M. Nascimento and J. M. Dias, "Vertex component analysis: A fast algorithm to unmix hyperspectral data," *IEEE Transactions on Geoscience and Remote Sensing*, vol. 43, no. 4, pp. 898–910, 2005.

[60] J. W. Boardman, "Automating spectral unmixing of AVIRIS data using convex geometry concepts," in *Summaries 4th Annual JPL Airborne Geoscience Workshop*. JPL Publication 93–26, 1993, pp. 11–14.

[61] M. E. Winter, "N-FINDR: an algorithm for fast autonomous spectral endmember determination in hyperspectral data," in *SPIE's international sym-*

posium on optical science, engineering, and instrumentation. International Society for Optics and Photonics, 1999, pp. 266–275.

[62] M. D. Craig, "Minimum-volume transforms for remotely sensed data," *IEEE Transactions on Geoscience and Remote Sensing*, vol. 32, no. 3, pp. 542–552, 1994.

[63] R. Schachtner, G. Pöppel, A. M. Tomé, and E. W. Lang, "Minimum determinant constraint for non-negative matrix factorization," in *Independent component analysis and signal separation.* (Springer, Heidelberg, Germany, 2009).

[64] J. Li and J. M. Bioucas-Dias, "Minimum volume simplex analysis: a fast algorithm to unmix hyperspectral data," in *IEEE iternational geoscience and remote sensing symposium*, vol. 3. IEEE, 2008, pp. III–250.

[65] J. M. Bioucas-Dias, "A variable splitting augmented lagrangian approach to linear spectral unmixing," in *First workshop on Hyperspectral Image and Signal Processing: Evolution in Remote Sensing.* IEEE, 2009, pp. 1–4.

[66] D. W. Hosmer Jr, S. Lemeshow, and R. X. Sturdivant, *Applied logistic regression.* (Wiley, Hoboken, New Jersey, USA, 2013).

[67] T. Hastie, R. Tibshirani, and J. J. H. Friedman, *The elements of statistical learning.* (Springer, New York, USA, 2001).

[68] E. K. Chong and S. H. Zak, *An introduction to optimization.* (John Wiley & Sons, Hoboken, New Jersey, USA, 2013).

[69] J. Park, P. Pande, S. Shrestha, F. Clubb, B. E. Applegate, and J. A. Jo, "Biochemical characterization of atherosclerotic plaques by endogenous multispectral fluorescence lifetime imaging microscopy," *Atherosclerosis*, vol. 220, no. 2, pp. 394–401, 2012.

[70] C.-I. Chang and Q. Du, "Estimation of number of spectrally distinct signal sources in hyperspectral imagery," *IEEE Transactions on Geoscience and Remote Sensing*, vol. 42, no. 3, pp. 608–619, 2004.

[71] A. A. Green, M. Berman, P. Switzer, and M. D. Craig, "A transformation for ordering multispectral data in terms of image quality with implications for noise removal," *IEEE Transactions on Geoscience and Remote Sensing*, vol. 26, no. 1, pp. 65–74, 1988.

[72] J. B. Lee, A. S. Woodyatt, and M. Berman, "Enhancement of high spectral resolution remote-sensing data by a noise-adjusted principal components transform," *IEEE Transactions on Geoscience and Remote Sensing*, vol. 28, no. 3, pp. 295–304, 1990.

[73] J. F. Granada, G. L. Kaluza, A. E. Raizner, and P. R. Moreno, "Vulnerable plaque paradigm: prediction of future clinical events based on a morphological definition," *Catheterization and Cardiovascular Interventions*, vol. 62, no. 3, pp. 364–374, 2004.

[74] B. K. Jefferson and E. J. Topol, "Molecular mechanisms of myocardial infarction," *Current Problems in Cardiology*, vol. 30, no. 7, pp. 333–374, 2005.

[75] F. Montecucco and F. Mach, "Atherosclerosis is an inflammatory disease," in *Seminars in immunopathology*. Springer, 2009, pp. 1–3.

[76] M. T. Quinn, S. Parthasarathy, L. G. Fong, and D. Steinberg, "Oxidatively modified low density lipoproteins: a potential role in recruitment and retention of monocyte/macrophages during atherogenesis," *Proceedings of the National Academy of Sciences*, vol. 84, no. 9, pp. 2995–2998, 1987.

[77] R. Stocker and J. F. Keaney, "Role of oxidative modifications in atherosclerosis," *Physiological Reviews*, vol. 84, no. 4, pp. 1381–1478, 2004.

[78] P. Libby, P. M. Ridker, and A. Maseri, "Inflammation and atherosclerosis," *Circulation*, vol. 105, no. 9, pp. 1135–1143, 2002.

[79] A. V. Finn, M. Nakano, J. Narula, F. D. Kolodgie, and R. Virmani, "Concept of vulnerable/unstable plaque," *Arteriosclerosis, Thrombosis, and Vascular Biology*, vol. 30, no. 7, pp. 1282–1292, 2010.

[80] R. Virmani, A. P. Burke, A. Farb, and F. D. Kolodgie, "Pathology of the vulnerable plaque," *Journal of the American College of Cardiology*, vol. 47, no. 8, pp. C13–C18, 2006.

[81] I. Jang, G. J. Tearney, B. MacNeill, M. Takano, F. Moselewski, N. Iftima, M. Shishkov, S. Houser, H. T. Aretz, E. F. Halpern *et al.*, "In vivo characterization of coronary atherosclerotic plaque by use of optical coherence tomography," *Circulation*, vol. 111, no. 12, pp. 1551–1555, 2005.

[82] B. D. MacNeill, B. E. Bouma, H. Yabushita, I.-K. Jang, and G. J. Tearney, "Intravascular optical coherence tomography: cellular imaging," *Journal of Nuclear Cardiology*, vol. 12, no. 4, pp. 460–465, 2005.

[83] H. Yabushita, B. E. Bouma, S. L. Houser, H. T. Aretz, I. Jang, K. H. Schlendorf, C. R. Kauffman, M. Shishkov, D.-H. Kang, E. F. Halpern *et al.*, "Characterization of human atherosclerosis by optical coherence tomography," *Circulation*, vol. 106, no. 13, pp. 1640–1645, 2002.

[84] F. Prati, E. Regar, G. S. Mintz, E. Arbustini, C. Di Mario, I.-K. Jang, T. Akasaka, M. Costa, G. Guagliumi, E. Grube *et al.*, "Expert review document on methodology, terminology, and clinical applications of optical coherence tomography: physical principles, methodology of image acquisition, and clinical application for assessment of coronary arteries and atherosclerosis," *European Heart Journal*, vol. 31, no. 4, pp. 401–415, 2010.

[85] O. Manfrini, E. Mont, O. Leone, E. Arbustini, V. Eusebi, R. Virmani, and R. Bugiardini, "Sources of error and interpretation of plaque morphology by optical coherence tomography," *The American Journal of Cardiology*, vol. 98, no. 2, pp. 156–159, 2006.

[86] M. G. Müller, T. A. Valdez, I. Georgakoudi, V. Backman, C. Fuentes, S. Kabani, N. Laver, Z. Wang, C. W. Boone, R. R. Dasari *et al.*, "Spectroscopic detection and evaluation of morphologic and biochemical changes in early human oral carcinoma," *Cancer*, vol. 97, no. 7, pp. 1681–1692, 2003.

[87] P. Soille, *Morphological image analysis: principles and applications.* (Springer-Verlag, New York, USA, 2003).

[88] K. W. Gossage, T. S. Tkaczyk, J. J. Rodriguez, and J. K. Barton, "Texture analysis of optical coherence tomography images: feasibility for tissue classification," *Journal of Biomedical Optics*, vol. 8, no. 3, pp. 570–575, 2003.

[89] A. A. Lindenmaier, L. Conroy, G. Farhat, R. S. DaCosta, C. Flueraru, and I. A. Vitkin, "Texture analysis of optical coherence tomography speckle for characterizing biological tissues in vivo," *Optics Letters*, vol. 38, no. 8, pp. 1280–1282, 2013.

[90] X. Tang, "Texture information in run-length matrices," *IEEE Transactions on Image Processing*, vol. 7, no. 11, pp. 1602–1609, 1998.

[91] T. G. Dietterich, "Ensemble methods in machine learning," in *Multiple classifier systems.* (Springer-Verlag, New York, USA, 2000).

[92] L. Breiman, "Random forests," *Machine Learning*, vol. 45, no. 1, pp. 5–32, 2001.

[93] A. Criminisi, "Decision forests: A unified framework for classification, regression, density estimation, manifold learning and semi-supervised learning," *Foundations and Trends in Computer Graphics and Vision*, vol. 7, no. 2-3, pp. 81–227, 2011.

[94] H. Peng, F. Long, and C. Ding, "Feature selection based on mutual information criteria of max-dependency, max-relevance, and min-redundancy," *IEEE Transactions on Pattern Analysis and Machine Intelligence*, vol. 27, no. 8, pp. 1226–1238, 2005.

[95] J. Demšar, "Statistical comparisons of classifiers over multiple data sets," *The Journal of Machine Learning Research*, vol. 7, pp. 1–30, 2006.

[96] D. G. Farwell, J. D. Meier, J. Park, Y. Sun, H. Coffman, B. Poirier, J. Phipps, S. Tinling, D. J. Enepekides, and L. Marcu, "Time-resolved fluorescence spectroscopy as a diagnostic technique of oral carcinoma: validation in the hamster buccal pouch model," *Archives of Otolaryngology–Head & Neck Surgery*, vol. 136, no. 2, pp. 126–133, 2010.

[97] M. W. Lingen, J. R. Kalmar, T. Karrison, and P. M. Speight, "Critical evaluation of diagnostic aids for the detection of oral cancer," *Oral Oncology*, vol. 44, no. 1, pp. 10–22, 2008.

[98] R. Mehrotra and D. K. Gupta, "Exciting new advances in oral cancer diagnosis: avenues to early detection," *Head & Neck Oncology*, vol. 3, no. 1, pp. 1–9, 2011.

[99] A. Gillenwater, R. Jacob, R. Ganeshappa, B. Kemp, A. K. El-Naggar, J. L. Palmer, G. Clayman, M. F. Mitchell, and R. Richards-Kortum, "Noninvasive diagnosis of oral neoplasia based on fluorescence spectroscopy and native tissue autofluorescence," *Archives of Otolaryngology–Head & Neck Surgery*, vol. 124, no. 11, pp. 1251–1258, 1998.

[100] D. De Veld, M. Witjes, H. Sterenborg, and J. Roodenburg, "The status of in vivo autofluorescence spectroscopy and imaging for oral oncology," *Oral Oncology*, vol. 41, no. 2, pp. 117–131, 2005.

[101] I. Pavlova, M. Williams, A. El-Naggar, R. Richards-Kortum, and A. Gillenwater, "Understanding the biological basis of autofluorescence imaging for oral cancer detection: high-resolution fluorescence microscopy in viable tissue," *Clinical Cancer Research*, vol. 14, no. 8, pp. 2396–2404, 2008.

[102] R. Drezek, C. Brookner, I. Pavlova, I. Boiko, A. Malpica, R. Lotan, M. Follen, and R. Richards-Kortum, "Autofluorescence microscopy of fresh cervical-tissue sections reveals alterations in tissue biochemistry with dysplasia," *Photochemistry and Photobiology*, vol. 73, no. 6, pp. 636–641, 2001.

[103] J. E. Bouquot and R. J. Gorlin, "Leukoplakia, lichen planus, and other oral keratoses in 23,616 white americans over the age of 35 years," *Oral Surgery, Oral Medicine, Oral Pathology*, vol. 61, no. 4, pp. 373–381, 1986.

[104] B. W. Neville and T. A. Day, "Oral cancer and precancerous lesions," *CA: A Cancer Journal for Clinicians*, vol. 52, no. 4, pp. 195–215, 2002.

[105] Y. Wu, P. Xi, J. Qu, T.-H. Cheung, and M.-Y. Yu, "Depth-resolved fluorescence spectroscopy reveals layered structure of tissue," *Optics Express*, vol. 12, no. 14, pp. 3218–3223, 2004.

[106] Y. Wu and J. Y. Qu, "Combined depth-and time-resolved autofluorescence

spectroscopy of epithelial tissue," *Optics Letters*, vol. 31, no. 12, pp. 1833–1835, 2006.

[107] K. Doi, H. MacMahon, S. Katsuragawa, R. M. Nishikawa, and Y. Jiang, "Computer-aided diagnosis in radiology: potential and pitfalls," *European Journal of Radiology*, vol. 31, no. 2, pp. 97–109, 1999.

[108] R. A. Castellino, "Computer aided detection (CAD): an overview," *Cancer Imaging*, vol. 5, no. 1, p. 17, 2005.

[109] T. W. Freer and M. J. Ulissey, "Screening mammography with computer-aided detection: Prospective study of 12,860 patients in a community breast center 1," *Radiology*, vol. 220, no. 3, pp. 781–786, 2001.

[110] K. Doi, "Computer-aided diagnosis in medical imaging: historical review, current status and future potential," *Computerized Medical Imaging and Graphics*, vol. 31, no. 4-5, pp. 198–211, 2007.

APPENDIX A

TABLES FOR THE STATISTICAL TESTS DESCRIBED IN SECTIONS 7.3.1–7.3.3

Table A.1: Comparison of classification accuracies for classifiers based on the exact and approximate FLIM features. For each CV fold, all but one dataset were used for training the classifier and the classification accuracy was estimated by testing the classifier on the left-out dataset listed under the dataset column. The differences, ranks and signs were used to perform a Wilcoxon signed rank test summarized in Table 7.1 to compare the classification accuracies for the two sets of FLIM features

		Accuracy				
CV Fold	Dataset	Exact FLIM	Approx. FLIM	Difference	Rank	Sign
1	JJN03-03	1.00	1.00	0.00	1	+
2	JJN03-04	0.78	1.00	0.22	23	-
3	JJN04-02	1.00	1.00	0.00	N/A	
4	JJN05-01	1.00	1.00	0.00	N/A	
5	JJN05-04	1.00	1.00	0.00	N/A	
6	JJN05-05	1.00	1.00	0.00	N/A	
7	JJN08-03	1.00	1.00	0.00	N/A	
8	JJN12-04	1.00	1.00	0.00	N/A	
9	JJN15-03	1.00	1.00	0.00	N/A	
10	JJN16-03	1.00	1.00	0.00	N/A	
11	JJN16-09	1.00	1.00	0.00	N/A	
12	JJN17-05	1.00	1.00	0.00	N/A	
13	JJN18-03	1.00	1.00	0.00	N/A	
14	JJN19-03	1.00	1.00	0.00	N/A	
15	JJN20-01	1.00	1.00	0.01	4	+
16	JJT02-01	1.00	0.84	0.16	21	+
17	JJT02-04	1.00	0.71	0.29	27	+
18	JJT03-02	0.02	0.64	0.62	30	-

Continued on next page

Table A.1 – *Continued from previous page*

CV Fold	Dataset	Accuracy: Exact FLIM	Accuracy: Approx. FLIM	Difference	Rank	Sign
19	JJT07-03	0.96	0.40	0.56	29	+
20	JJT07-04	0.00	0.07	0.07	11	-
21	JJT09-01	0.83	0.21	0.62	31	+
22	JJT09-03	0.70	0.61	0.09	13	+
23	JJT10-02	0.99	0.96	0.03	10	+
24	JJT13-01	0.93	0.84	0.08	12	+
25	JJT12-02	0.98	0.99	0.00	1	-
26	JJT12-04	0.75	0.76	0.01	6	-
27	JJT17-05	0.11	0.00	0.11	16	+
28	JJT21-06	0.90	0.77	0.13	18	+
29	JJT24-04	0.96	0.95	0.01	7	+
30	JJT24-07	0.93	0.69	0.24	25	+
31	JJT24-09	0.98	0.87	0.12	17	+
32	JJT25-06	0.00	0.91	0.91	32	-
33	JJT27-04	0.99	0.75	0.25	26	+
34	JJT27-10	0.62	0.72	0.09	14	-
35	JJT28-11	0.51	0.74	0.23	24	-
36	JJT16-05	0.99	0.99	0.01	5	+
37	JJT16-10	0.97	0.94	0.03	9	+
38	JJT18-05	0.77	0.26	0.51	28	+
39	JJT18-06	1.00	1.00	0.00	N/A	
40	JJT18-07	0.47	0.34	0.13	19	+
41	JJT23-04	0.74	0.59	0.15	20	+
42	JJT25-07	1.00	1.00	0.00	3	+
43	JJT26-06	1.00	1.00	0.00	N/A	
44	JJT27-03	1.00	1.00	0.00	N/A	
45	JJT28-06	0.73	0.83	0.10	15	-
46	JJT28-08	1.00	1.00	0.00	N/A	
47	JJT28-12	0.61	0.45	0.16	22	+
48	JJT32-08	1.00	0.98	0.02	8	+
Mean Accuarcy		0.837	0.807			

Table A.2: Comparison of classification accuracies for classifiers based on different FLIM features. For each CV fold, all but one dataset were used for training the classifier and the classification accuracy was estimated by testing the classifier on the left-out dataset listed under the dataset column

CV		Accuracies for FLIM Features			
Fold	Dataset	All	Int.	Int. & $\tau_{1/e}$	Int. & τ_{avg}
1	JJN03-03	1.000	0.883	0.950	1.000
2	JJN03-04	0.780	0.603	0.483	0.995
3	JJN04-02	1.000	0.540	0.760	1.000
4	JJN05-01	1.000	0.853	0.965	1.000
5	JJN05-04	1.000	0.843	0.998	1.000
6	JJN05-05	1.000	0.510	0.635	1.000
7	JJN08-03	1.000	0.738	0.998	1.000
8	JJN12-04	1.000	0.839	0.814	1.000
9	JJN15-03	1.000	0.768	0.738	1.000
10	JJN16-03	1.000	0.998	0.998	1.000
11	JJN16-09	1.000	0.992	1.000	1.000
12	JJN17-05	1.000	0.705	0.693	1.000
13	JJN18-03	1.000	0.983	0.998	1.000
14	JJN19-03	1.000	0.873	1.000	1.000
15	JJN20-01	1.000	0.790	0.818	1.000
16	JJT02-01	1.000	0.816	0.572	1.000
17	JJT02-04	1.000	0.865	0.589	1.000
18	JJT03-02	0.018	0.388	0.003	0.015
19	JJT07-03	0.958	0.770	0.113	0.658
20	JJT07-04	0.000	0.285	0.583	0.000
21	JJT09-01	0.830	0.388	0.373	0.514
22	JJT09-03	0.698	0.360	0.193	0.848
23	JJT10-02	0.990	0.583	0.815	0.990
24	JJT13-01	0.925	0.358	0.863	0.845
25	JJT12-02	0.983	0.478	0.945	0.973
26	JJT12-04	0.746	0.075	0.061	0.587
27	JJT17-05	0.110	0.000	0.048	0.008
28	JJT21-06	0.898	0.430	0.705	0.768
29	JJT24-04	0.963	0.443	0.550	0.578
30	JJT24-07	0.930	0.304	0.368	0.635
31	JJT24-09	0.980	0.545	0.770	0.900
32	JJT25-06	0.000	0.213	0.528	0.000

Continued on next page

Table A.2 – *Continued from previous page*

CV Fold	Dataset	Accuracies for FLIM Features			
		All	Int.	Int. & $\tau_{1/e}$	Int. & τ_{avg}
33	JJT27-04	0.993	0.473	0.843	0.833
34	JJT27-10	0.623	0.000	0.058	0.468
35	JJT28-11	0.509	0.576	0.501	0.574
36	JJT16-05	0.995	0.960	0.995	0.987
37	JJT16-10	0.968	0.949	0.978	0.863
38	JJT18-05	0.768	0.168	0.580	0.310
39	JJT18-06	1.000	0.991	1.000	1.000
40	JJT18-07	0.470	0.083	0.360	0.383
41	JJT23-04	0.735	0.588	0.675	0.648
42	JJT25-07	1.000	0.997	0.997	0.997
43	JJT26-06	0.998	1.000	1.000	0.995
44	JJT27-03	0.997	0.994	0.997	0.994
45	JJT28-06	0.734	0.688	0.741	0.703
46	JJT28-08	1.000	1.000	1.000	1.000
47	JJT28-12	0.609	0.497	0.525	0.639
48	JJT32-08	0.997	0.959	0.967	0.949
Mean Accuarcy		0.836	0.638	0.690	0.784

Table A.3: Ranks for the data presented in Table A.2 for performing the Friedman test to compare the classification accuracies for the different sets of FLIM features.

CV		Ranks for FLIM Features			
Fold	Dataset	All	Int.	Int. & $\tau_{1/e}$	Int. & τ_{avg}
1	JJN03-03	3.5	1.0	2.0	3.5
2	JJN03-04	3.0	2.0	1.0	4.0
3	JJN04-02	3.5	1.0	2.0	3.5
4	JJN05-01	3.5	1.0	2.0	3.5
5	JJN05-04	3.5	1.0	2.0	3.5
6	JJN05-05	3.5	1.0	2.0	3.5
7	JJN08-03	3.5	1.0	2.0	3.5
8	JJN12-04	3.5	2.0	1.0	3.5
9	JJN15-03	3.5	2.0	1.0	3.5
10	JJN16-03	3.5	1.5	1.5	3.5
11	JJN16-09	3.0	1.0	3.0	3.0
12	JJN17-05	3.5	2.0	1.0	3.5
13	JJN18-03	3.5	1.0	2.0	3.5
14	JJN19-03	3.0	1.0	3.0	3.0
15	JJN20-01	3.5	1.0	2.0	3.5
16	JJT02-01	3.5	2.0	1.0	3.5
17	JJT02-04	3.5	2.0	1.0	3.5
18	JJT03-02	3.0	4.0	1.0	2.0
19	JJT07-03	4.0	3.0	1.0	2.0
20	JJT07-04	1.5	3.0	4.0	1.5
21	JJT09-01	4.0	2.0	1.0	3.0
22	JJT09-03	3.0	2.0	1.0	4.0
23	JJT10-02	3.5	1.0	2.0	3.5
24	JJT13-01	4.0	1.0	3.0	2.0
25	JJT12-02	4.0	1.0	2.0	3.0
26	JJT12-04	4.0	2.0	1.0	3.0
27	JJT17-05	4.0	1.0	3.0	2.0
28	JJT21-06	4.0	1.0	2.0	3.0
29	JJT24-04	4.0	1.0	2.0	3.0
30	JJT24-07	4.0	1.0	2.0	3.0
31	JJT24-09	4.0	1.0	2.0	3.0
32	JJT25-06	1.5	3.0	4.0	1.5
33	JJT27-04	4.0	1.0	3.0	2.0
34	JJT27-10	4.0	1.0	2.0	3.0

Continued on next page

Table A.3 – *Continued from previous page*

CV Fold	Dataset	Ranks for FLIM Features			
		All	Int.	Int. & $\tau_{1/e}$	Int. & τ_{avg}
35	JJT28-11	2.0	4.0	1.0	3.0
36	JJT16-05	3.5	1.0	3.5	2.0
37	JJT16-10	3.0	2.0	4.0	1.0
38	JJT18-05	4.0	1.0	3.0	2.0
39	JJT18-06	3.0	1.0	3.0	3.0
40	JJT18-07	4.0	1.0	2.0	3.0
41	JJT23-04	4.0	1.0	3.0	2.0
42	JJT25-07	4.0	2.0	2.0	2.0
43	JJT26-06	2.0	3.5	3.5	1.0
44	JJT27-03	3.5	1.5	3.5	1.5
45	JJT28-06	3.0	1.0	4.0	2.0
46	JJT28-08	2.5	2.5	2.5	2.5
47	JJT28-12	3.0	1.0	2.0	4.0
48	JJT32-08	4.0	2.0	3.0	1.0
Mean Rank		3.4	1.6	2.2	2.8

Table A.4: Comparison of classification accuracies for classifiers based on different features. For each CV fold, all but one dataset were used for training the classifier and the classification accuracy was estimated by testing the classifier on the left-out dataset listed under the dataset column

CV		Accuracies for Different Features		
Fold	Dataset	FLIM & OCT	FLIM	OCT
1	JJN03-03	1.000	1.000	0.995
2	JJN03-04	1.000	0.780	0.998
3	JJN04-02	1.000	1.000	1.000
4	JJN05-01	1.000	1.000	1.000
5	JJN05-04	1.000	1.000	0.998
6	JJN05-05	1.000	1.000	0.935
7	JJN08-03	1.000	1.000	1.000
8	JJN12-04	1.000	1.000	0.907
9	JJN15-03	1.000	1.000	0.398
10	JJN16-03	1.000	1.000	0.158
11	JJN16-09	1.000	1.000	0.510
12	JJN17-05	0.995	1.000	0.013
13	JJN18-03	1.000	1.000	1.000
14	JJN19-03	1.000	1.000	1.000
15	JJN20-01	1.000	1.000	0.858
16	JJT02-01	0.997	1.000	0.874
17	JJT02-04	1.000	1.000	0.964
18	JJT03-02	0.050	0.018	0.878
19	JJT07-03	1.000	0.958	1.000
20	JJT07-04	0.000	0.000	0.935
21	JJT09-01	0.481	0.830	0.135
22	JJT09-03	0.915	0.698	0.665
23	JJT10-02	0.998	0.990	0.900
24	JJT13-01	0.995	0.925	0.735
25	JJT12-02	0.980	0.983	0.535
26	JJT12-04	0.966	0.746	0.626
27	JJT17-05	0.390	0.110	0.958
28	JJT21-06	0.880	0.898	0.653
29	JJT24-04	0.563	0.963	0.388
30	JJT24-07	0.962	0.930	0.933
31	JJT24-09	0.958	0.980	0.920
32	JJT25-06	0.023	0.000	0.998

Continued on next page

Table A.4 – *Continued from previous page*

CV Fold	Dataset	Accuracies for Different Features		
		FLIM & OCT	FLIM	OCT
33	JJT27-04	1.000	0.993	0.960
34	JJT27-10	0.953	0.623	0.625
35	JJT28-11	0.818	0.509	0.799
36	JJT16-05	0.997	0.995	0.989
37	JJT16-10	0.997	0.968	0.990
38	JJT18-05	0.825	0.768	0.868
39	JJT18-06	1.000	1.000	1.000
40	JJT18-07	0.705	0.470	0.695
41	JJT23-04	0.758	0.735	0.728
42	JJT25-07	1.000	1.000	0.990
43	JJT26-06	1.000	0.998	0.953
44	JJT27-03	0.997	0.997	0.980
45	JJT28-06	1.000	0.734	0.980
46	JJT28-08	1.000	1.000	0.968
47	JJT28-12	0.614	0.609	0.581
48	JJT32-08	0.995	0.997	0.882
Mean Accuarcy		0.871	0.837	0.809

Table A.5: Ranks for the data presented in Table A.3 for performing the Friedman test to compare the classification accuracies for the different sets of features.

CV		Ranks for Different Features		
Fold	Dataset	FLIM & OCT	FLIM	OCT
1	JJN03-03	2.5	2.5	1.0
2	JJN03-04	3.0	1.0	2.0
3	JJN04-02	2.0	2.0	2.0
4	JJN05-01	2.0	2.0	2.0
5	JJN05-04	2.5	2.5	1.0
6	JJN05-05	2.5	2.5	1.0
7	JJN08-03	2.0	2.0	2.0
8	JJN12-04	2.5	2.5	1.0
9	JJN15-03	2.5	2.5	1.0
10	JJN16-03	2.5	2.5	1.0
11	JJN16-09	2.5	2.5	1.0
12	JJN17-05	2.0	3.0	1.0
13	JJN18-03	2.0	2.0	2.0
14	JJN19-03	2.0	2.0	2.0
15	JJN20-01	2.5	2.5	1.0
16	JJT02-01	2.0	3.0	1.0
17	JJT02-04	2.5	2.5	1.0
18	JJT03-02	2.0	1.0	3.0
19	JJT07-03	2.5	1.0	2.5
20	JJT07-04	1.5	1.5	3.0
21	JJT09-01	2.0	3.0	1.0
22	JJT09-03	3.0	2.0	1.0
23	JJT10-02	3.0	2.0	1.0
24	JJT13-01	3.0	2.0	1.0
25	JJT12-02	2.0	3.0	1.0
26	JJT12-04	3.0	2.0	1.0
27	JJT17-05	2.0	1.0	3.0
28	JJT21-06	2.0	3.0	1.0
29	JJT24-04	2.0	3.0	1.0
30	JJT24-07	3.0	1.0	2.0
31	JJT24-09	2.0	3.0	1.0
32	JJT25-06	2.0	1.0	3.0
33	JJT27-04	3.0	2.0	1.0
34	JJT27-10	3.0	1.0	2.0

Continued on next page

Table A.5 – *Continued from previous page*

CV Fold	Dataset	Ranks for Different Features		
		FLIM & OCT	FLIM	OCT
35	JJT28-11	3.0	1.0	2.0
36	JJT16-05	3.0	2.0	1.0
37	JJT16-10	3.0	1.0	2.0
38	JJT18-05	2.0	1.0	3.0
39	JJT18-06	2.0	2.0	2.0
40	JJT18-07	3.0	1.0	2.0
41	JJT23-04	3.0	2.0	1.0
42	JJT25-07	2.5	2.5	1.0
43	JJT26-06	3.0	2.0	1.0
44	JJT27-03	2.5	2.5	1.0
45	JJT28-06	3.0	1.0	2.0
46	JJT28-08	2.5	2.5	1.0
47	JJT28-12	3.0	2.0	1.0
48	JJT32-08	2.0	3.0	1.0
Mean Rank		2.5	2.0	1.5